**INSTITUTE OF FUNDAMENTAL AND APPLIED RESEARCH**

**UDC: 530.12:531.51**

**Uktamov Uktamjon Xayrulla o'g'li**

# Dynamics of gravitational objects in SMBH environment with dark matter halo and magnetic field

**01.04.02- THEORETICAL PHYSICS**
**01.03.01- ASTRONOMY**

**DISSERTATION OF THE DOCTOR OF PHILOSOPHY (PhD)**
**IN PHYSICS AND MATHEMATICS**

**Scientific supervisors:** Ahmedov Bobomurat Juraevich
doctor of sciences in physics and mathematics,
academician
Shaymatov Sanjar Ruzimurotovich
doctor of sciences in physics and mathematics

**Tashkent – 2025**

# Contents

**Acronyms**

| | |
|---|---|
| **DM** | **D**ark-**M**atter |
| **ADM** | **A**rnowitt-**D**eser-**M**isner |
| **BH** | **B**lack **H**ole |
| **CNG** | **C**ircular **N**ull **G**eodesics |
| **EHT** | **E**vent **H**orizon **T**elescope |
| **EM** | **E**lectro**m**agnetic |
| **EoS** | **E**quation **o**f **S**tate |
| **ESO** | **E**uropean **S**outhern **O**bservatory |
| **GR** | **G**eneral **R**elativity |
| **ISCO** | **I**nnermost **S**table **C**ircular **O**rbit |
| **LIGO** | **L**aser **I**nterferometer **G**ravitational-Wave **O**bservatory |
| **LISA** | **L**aser **I**nterferometer **S**pace **A**ntenna |
| **GW** | **G**ravitational-**W**aves |
| **SMBH** | **S**uppermassive **B**lack **H**ole |
| **ODE** | **O**rdinary **D**ifferential **E**quation |
| **OSCO** | **O**utermost **S**table **C**ircular **O**rbit |
| **LQG** | **L**oop-**Q**uantum **G**ravity |
| **RN** | **R**eissner-**N**ordström |
| **Sgr A*** | **S**ag**g**itta**r**ius **A*** |
| **VLT** | **V**ery **L**arge **T**elescope |

**Physical constants & other definitions**

| | |
|---|---|
| Speed of Light | $c = 2.998 \times 10^{10}$ cm s$^{-1}$ |
| Gravitational constant | $G = 6.672 \times 10^{-8}$ cm$^3$ g$^{-1}$ s$^{-2}$ |
| Mass of the Sun | $M_\odot = 1.989 \times 10^{33}$ g |
| Mass of Sgr A* | $M_* = 4.14 \times 10^6 M_\odot = 8.23 \times 10^{39}$ g |
| Schwarzschild radius of the Sun | $r_{Schw.} = 2GM_\odot/c^2 = 2.95 \times 10^5$ cm |
| Schwarzschild radius of Sgr A* | $R_{Schw.} = 2GM_*/c^2 = 1.22 \times 10^{12}$ cm |

1 parsec = 1 pc = 3.26 ly = $3.08 \times 10^{18}$ cm

1 eV = $1.6 \times 10^{-19}$J = $1.6 \times 10^{-12}$ erg

1 Gauss = 1 G = $10^{-4}$ T

# Introduction

**Relevance and necessity of the topic.** Nowadays, advanced astronomical instruments like the Laser Interferometer Gravitational-Wave Observatory (LIGO-VIRGO) and Event Horizon Telescope enable direct detection of gravitational waves from merging black holes and binary neutron stars , as well as capturing images of the supermassive black hole at the core of the M87 galaxy. The direct observation of gravitational waves and the detailed imaging of a supermassive black hole using these advanced instruments shed light on astrophysical events in strong gravitational fields. These cutting-edge observations are vital for developing new solutions in alternative gravity theories and for exploring challenges tied to accurately measuring parameters and understanding the essence of dark matter. Analyzing the interaction between dark matter (DM) and black holes (BHs) is crucial for enhancing our understanding of DM's fundamental nature. Given the significance of DM halos and their interplay with BH systems, studying and modeling DM through astrophysical data and simulations can provide valuable insights. To this end, several analytical models, such as the Einasto, Burkert, and Dehnen models, have been developed to describe BH solutions within DM halos. Our Republic places significant emphasis on fundamental research in the area of relativistic astrophysics of BHs. The primary areas of fundamental research and development, as well as their practical applications for advancing science in our nation, are detailed in the Strategy for the Further Development

of the Republic of Uzbekistan for 2022–2026[1]. Over the last three decades, the Republic has advanced relativistic astrophysics of gravitational compact objects, thoroughly investigating the energy and optical characteristics of BHs, wormholes, and naked singularities. New effects of general relativity have been discovered in the relativistic astrophysics of magnetized neutron stars, and progress has been made in understanding relativistic magnetospheres and plasma, as well as magnetized relativistic objects. The origins of fast radio bursts, partially emitting pulsars, and radio-quiet magnetars have been elucidated. The country is also establishing new fields, including gravitational wave astronomy, X-ray astronomy, and radio astronomy. This dissertation focuses on fulfilling objectives outlined in state regulatory documents, including Presidential Decree No. UP-4947 of February 7, 2017, on the Strategy for the Further Development of the Republic of Uzbekistan, and the "Roadmap of Key Structural Reform Directions in Uzbekistan for 2019–2021," issued by the Government of Uzbekistan on November 29, 2018.

**Conformity of the research to the main priorities of science and technology development of the republic.** The research has been conducted in line with the priority areas of science and technology in the Republic of Uzbekistan, specifically under the category II: "Power, Energy, and Resource-Saving."

**The aim of the research** is finding a novel analytical Schwarzschild-like BH in DM halo. Analyzing particle dynamics around SMBH and perform a comparative analysis of our findings with the observed position of the S2 star.

**The tasks of the research:**

to find a novel analytical Schwarzschild-like BH in Dehnen-type DM halo.

to analyze spacetime curvature characteristics and energy conditions of the obtained solution.

[1]Decree No. PF-60 of the President of the Republic of Uzbekistan dated January 1, 2022 “On the Development Strategy of New Uzbekistan for 2022-2026”

to derive the field equations and determine the electromagnetic four-vector for the case of self dual black hole in Loop Quantum Gravity (LQG).

to study the motion of magnetic dipoles and electrically charged particles in the vicinity of a BH in LQG, in the vicinity of the Schwarzschild BH immersed in external uniform magnetic field.

to investigate the bound and unbound motion of magnetized particles orbiting a Schwarzschild BH immersed in an external asymptotically uniform magnetic field.

to perform a comparative analysis of findings with the observed position of the S2 star carrying magnetic dipole moment around Sgr $A^*$.

**Connection of the topic of dissertation with the scientific works of scientific research organizations, where the dissertation was carried out.** The presentation was carried out within the framework of scientific projects funded by the Ministry of Innovative Development. FL-7923051796 "Modeling of Scalar Field Dynamics and Quantum Emitters in Spherically Symmetric Gravitational Fields",F-FA-2021-432 "Processing and Analysis of Satellite Data from Low Mass X-ray Binary Systems".

**The objects of the research** are astrophysical compact objects, particle dynamics, analytical models for DM halos, uniform magnetic fields in different spacetimes, S2 star trajectories.

**The subjects of the research** observational properties of black holes, Self dual BH immersed in magnetic field in LQG, particle dynamics around SMBH, analytical and numerical methods for solving differential equations of the motion of particles.

**The methods of the research** are the approaches involve theoretical physics and astrophysics, contemporary methods of theoretical astrophysics and mathematical physics, as well as analytical and numerical techniques for solving differ-

ential equations associated with field and particle dynamics.

**The scientific novelty of the research** is in the followings:

For the first time analytical Schwarzschild-like BH solution in Dehnen-type DM halo for core model has derived.

For the first time field equations and four-vector potential for the case of a self-dual BH in LQG is derived. The motion of magnetic dipoles and electric charged particles in the vicinity of a self-dual BH in LQG is learned.

For the first time bound and unboud motion of magnetized particles orbiting a Schwarzschild BH immersed in external uniform magnetic field is derived.

For the first time results of the obtained analysis is compared with the real positions of the S2 star and magnetic dipole of the star is estimated as $10^6 G \times cm^3$. Deflecting trajectories akin to gravitational Rutherford scattering is explored.

**Practical results** of the research are as follows:

Novel analytical Schwarzschild-like BH solution is derived, representing a static BH surrounded by a DM halo characterized by a Dehnen-type density profile (1,4,2). The properties of this BH is investigated by analyzing the spacetime curvature. The energy conditions, which are fundamental characteristics of the physicsl viability of spacetime, is examined.

A self-dual BH immersed in an external asymptotically uniform magnetic field is considered. The motion of magnetic dipoles and electrically charged particles in the environment surrounding the spacetime geometry in LQG is studied. The combined effects of the quantum correction parameter $P$ and the magnetic interaction parameter $\beta$ on the ISCO radius is studied. We analyzed captured, bound and escape orbits of magnetized and electrically charged particles restricted from moving on the equatorial plane of the self-dual black hole in LQG for various possible cases.

The bound and unbound orbits of the magnetized particles as they approached

a Schwarzschild BH in magnetic field are investigated. We derived and analyzed the effective potential experienced by approaching particles, classifying possible bound and unbound orbits based on their specific energy and angular momentum. Comparisons between observed positions of the S2 star around Sgr $A^*$ and theoretical predictions were made for two different values of $\beta$, calculating minimum and maximum values for this parameter and specific angular momentum of the S2 star.

**Reliability of the research results** is supported by the use of standard mathematical and theoretical physics methods in the dissertation, including highly effective numerical techniques and software. A meticulous verification was conducted to ensure the theoretical results aligned with existing data in limiting cases, observational evidence, and the findings of other researchers. Additionally, the conclusions are consistent with the core principles of the theory of gravitational compact objects in strong gravity regimes.

**Scientific and practical significance of the research results.** The scientific significance of the research results is that proposed a novel analytical Schwarzschild-like BH in DM halo can explain the nature of the dark matter.

The practical significance of the research results is that proposed model can explain environment of the Sgr $A^*$ and help to estimate magnetic dipole of the S2 star.

**Application of the research results.** Drawing on the dynamics of the compact objects, the scientific findings related to their properties have been utilized in studies by international researchers and published in high-impact foreign journals, including (Journal of Cosmology and Astroparticle Physics, 2025(03), Volume 2025, Web-Sc, IF: 5.9; The European Physical Journal C, Volume 85, Article number 786, Web-Sc, IF: 4.2; The European Physical Journal C, Volume 85, Article number 494, Web-Sc, IF: 4.2; Universe, Web-Sc, IF: 2.6;)

These scientific results were used within the framework of programs supported by the Vellore Institute of Technology (based on an official letter provided by Dr. Pankaj Sheoran).

**Volume and structure of the dissertation. The dissertation consists of an introduction, three chapters, conclusion and a bibliography. The size of the dissertation is 122 pages.**

**List of published papers [1, 2, 3].**

**Part I.**

1. U. Uktamov, M. Alloqulov, S. Shaymatov, T. Zhu, and B. Ahmedov, "Particle dynamics and the accretion disk around a Self-dual Black Hole immersed in a magnetic field in Loop Quantum Gravity," Phys. Dark Univ., vol. 47, p. 101743, 2025.

2. U. Uktamov, M. Fathi, J. Rayimbaev, and A. Abdujabbarov, "Orbits of particles with magnetic dipole moment around magnetized Schwarzschild black holes: Applications to the S2 star orbit," Phys.Rev.D, vol. 110, no. 8, p. 084084, Oct. 2024.

3. U. Uktamjon, B. Narzilloev, and B. Ahmedov, "Perturbation of spacetime and electromagnetic field due to massive charged particle around electrically charged stringy black hole," Eur. Phys. J. Plus, vol. 139, no. 10, p. 903, 2024.

**Part II.**

4. U.Uktamov, "Quasiperiodic oscillations around a Schwarzschild black hole surrounded by a Dehnen type dark matter halo", Fundamental and Applied Research in Physics, NUUz, May 16-17, 2025, pgs.156-157.

5. U.Uktamov, "On description shadow of the rotating Bardeen black hole with string clouds field", Fizika fanining rivojida iste'dodli yoshlarning o'rni (RIAK-XVI-2023), 28-29-aprel 2023-yil.

# Chapter I

# Schwarzschild-like black holess in dark matter halo

## 1.1 Dark matter halo

In general relativity (GR), BHs arise naturally as exact solutions to Einstein's gravitational field equations. These theoretical predictions were made a long time back; nearly a century later, observational evidence for the existence of BHs was found through modern revolutionary Event Horizon Telescope (EHT) and LIGO-VIRGO observations [4, 5, 6, 7]. These triumphal observations are expected to provide stringent tests that probe the nature and unknown aspects of BHs. However, open questions remain regarding the behavior of BHs and their interaction with their surroundings. Among them, the nature and existence of DM are long-standing problems in GR. Consequently, identifying evidence for DM within the BH environment has become a crucial task in GR.

In many astrophysical scenarios, supermassive BHs at the centers of galaxies are believed to be enveloped by matter distributions, including DM halos. It is well established that BHs are characterized by complex and dynamic environments, and there is substantial evidence to suggest that supermassive BHs at the center of most galaxies are the primary drivers of active galactic nuclei [8, 9] and are

surrounded by a DM halo [10, 11]. In addition to the possibility of DM enveloping supermassive BHs, considerable evidence suggests that DM significantly influences galactic rotation curves [12], bullet clusters [13], and the large-scale structure of the universe [14].

The discovery of unexpectedly flat galactic rotation curves in large spiral and elliptical galaxies led to the postulation of the existence of DM. This DM, now supported by extensive astrophysical observations, is estimated to constitute approximately 90% of the mass of a galaxy, the remaining 10% being luminous baryonic matter [15]. Initially concentrated near galactic centers, facilitating star formation and clustering, DM gradually migrated outward during galactic evolution, forming DM halos around the galaxy through various dynamical processes. Astrophysical observations reveal that many large spiral and elliptical galaxies harbor a central supermassive BH (sometimes binary systems) embedded within this DM halo [16, 6, 17, 7]. A substantial amount of DM in our universe is necessary to provide a satisfactory explanation for the observed phenomena. This is supported by cosmic microwave background observations, which reveal that DM comprises roughly 27% of the universe, alongside 68% dark energy. The rest of the universe, only around 5%, is considered normal matter. Numerous theoretical particle candidates, predicted by extensions of the standard-model, are being investigated as potential components of DM [18, 19, 20, 21], such as weakly interacting massive particles (WIMPs), axions, and sterile neutrinos. With this in view, properties of DM can then be probed gravitationally in the case of weak interaction within standard-model particles. Therefore, DM may be highly concentrated around supermassive BHs, commonly found in galactic centers [10, 11], significantly influencing extreme [22] and intermediate [23, 24] mass ratio inspirals and potentially revealing the distribution of the DM halo. The influence of DM halos on supermassive BHs is a critical area of research, driven by the need

to understand the DM-BH interaction. DM halo structures demonstrably affect galactic rotation curves [12, 11, 13] and dynamics observed in events such as the Bullet Cluster collision [25]. Although current models primarily describe DM as interacting gravitationally, a substantial body of evidence convincingly supports its existence [26, 27, 28].

Motivated by these findings, it is important to analyze the DM-BH interaction and look for DM models to help improve our understanding of the fundamental nature of DM. Given this fundamental importance of DM halos and their interaction with BH systems, the exploration and analysis of DM models can yield valuable insights, relying on astrophysical data and simulation studies. Motivated by this, several analytical models have been developed to describe BH solutions within DM halos, including the Einasto [29, 30], Navarro-Frenk-White [31], and Burkert [32] models, as well as the Dehnen model [33, 34, 35, 36, 37]. Additionally, some models incorporate a DM profile linked to a phantom scalar field [38, 39, 40, 41]. Furthermore, analytical models exhibiting supermassive BH solutions embedded in a DM halo have also been investigated in Refs. [42, 43, 44].

Investigations within the Dehnen-type DM halo model have also explored DM-BH interactions from various perspectives. For instance, one study examined the influence of density profile slopes on the survival of low star formation efficiency star clusters after rapid gas expulsion [34]. Other scenarios have also considered star clusters with Plummer and Dehnen profiles, focusing on differing slope cusps at the time of formation. Furthermore, the BH-Dehnen-type DM halo solution has been proposed to investigate ultra-faint dwarf galaxies [36]. Recent studies have also introduced new BH solutions surrounded by Dehnen-type DM halos, specifically $(1, 4, 0)$ [35] and $(1, 4, 5/2)$ [37] profiles, using Schwarzschild BH within the halo environment. Thermodynamics and null geodesics of the effective BH-DM halo system were analyzed [35], with a subsequent study constraining the DM

halo parameters [45]. Finally, the impact of the DM halo on quasinormal modes, the photon sphere radius and the BH shadow [46, 47], as well as gravitational waveforms from periodic orbits [48], were investigated within the solution of the BH-Dehnen-$(1, 4, 5/2)$ DM halo.

In this dissertation , we derive a new Schwarzschild-like BH solution immersed in a DM halo characterized by a Dehnen-type density profile $(1, 4, 2)$. To accomplish this, we adopt the method developed in [49, 50, 37]. We first analyze the spacetime curvature invariants and subsequently investigate the associated energy conditions. Finally, we explore the influence of the DM profile on timelike particle geodesics, providing deeper insights into how the DM halo affects particle geodesics.

The structure of this chapter is organized as follows: In Sec. 1.2, we present a new Schwarzschild-like BH solution surrounded by a DM halo with a Dehnen-type density profile. In Sec. 1.3, we investigate the spacetime curvature invariants and analyze the corresponding energy conditions. Finally, we summarize our findings and conclusions in Sec. 1.4. We use $(-, +, +, +)$ for the spacetime metric and the system of units $c = G = M = 1$ throughout the dissertation.

## 1.2 Schwarzchild-like black hole spacetime with the dark matter halo

Here, following the developed method [49, 50, 37] we consider a Schwarzschild-like BH spacetime surrounded a DM halo characterized by a Dehnen-type density profile. We first consider a background spacetime involving the DM distribution and then derive the BH-DM solution by solving Einstein's field equations. In this case, a Schwarzschild BH can be considered with a Dehnen-type DM halo mass distribution. This is determined by the DM density distribution (see details in Ref. [51]). With this approach, we start by describing the spacetime geometry

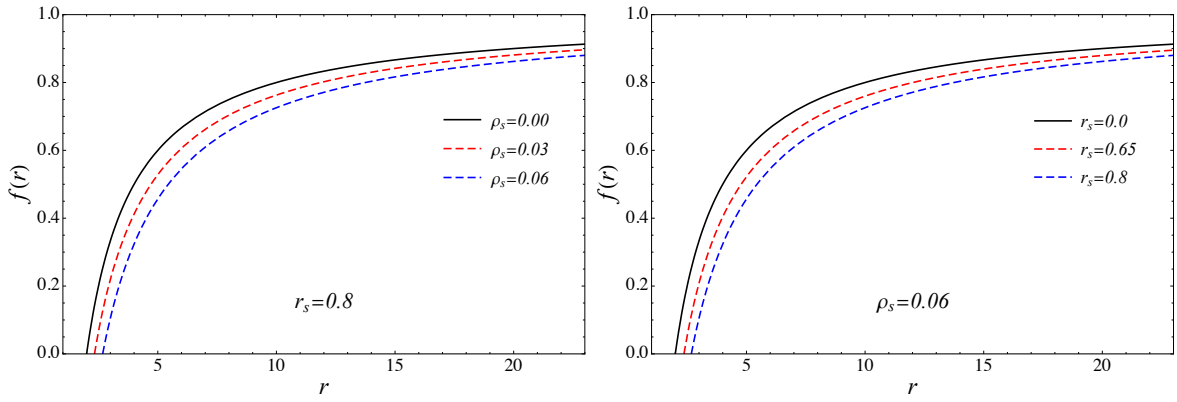


Figure 1.1: Radial profile of function $f(r)$ for various values of the characteristic density $\rho_s$ and characteristic scale $r_s$ of the DM halo. Hereafter, we shall for simplicity set $M = 1$.

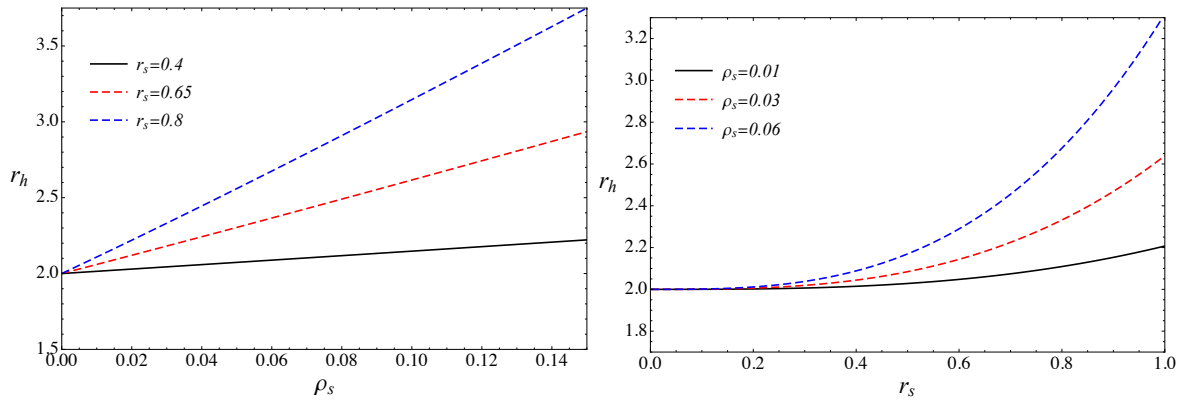


Figure 1.2: The dependence of BH event horizon on the density $\rho_s$ and the characteristic scale $r_s$ of the DM halo.

with the DM halo first and then include the Schwarzschild BH spacetime geometry. Now, we write the general form of the density profile in order to further derive the Dehnen-type DM halo mass distribution, which is defined by

$$\rho(r) = \rho_s \left(\frac{r}{r_s}\right)^{-\gamma} \left[\left(\frac{r}{r_s}\right)^{\alpha} + 1\right]^{\frac{\gamma-\beta}{\alpha}}, \tag{1.1}$$

where $\rho_s$ and $r_s$ are the characteristic density and characteristic scale of the DM halo, respectively. It must be emphasized that, apart from the characteristic DM halo parameters, $\alpha$, $\beta$ and $\gamma$ are specific parameters of the density profile. For example, $\gamma$ can range only from 0 to 3. In this work, we use the following Dehnen-type density distribution $(\alpha, \beta, \gamma) = (1, 4, 2)$ for the DM halo. Taken together

with Eq. (1.1), we derive the mass profile as follows:

$$M_D(r) = \int_0^r 4\pi\rho(r_{_1})r_{_1}^2 dr_{_1} = \frac{4\pi\rho_s r_s^3}{1+\frac{r_s}{r}}\,. \tag{1.2}$$

We then define the line element of the DM halo, including redshift $A(r)$ and shape $B(r)$ functions, which is given by

$$ds^2 = -A(r)dt^2 + \frac{dr^2}{B(r)} + r^2 d\Omega^2\,, \tag{1.3}$$

where $d\Omega^2 = d\theta^2 + \sin^2\theta d\phi^2$ is referred to as the solid angle in spherical coordinates. The point to be noted here is that $A(r)$ can be used to define the tangential velocity of particles moving within the DM halo as follows:

$$v_D^2 = \frac{1}{r}\partial_r\left(\log\sqrt{A(r)}\right) = \frac{M_D}{r}\,, \tag{1.4}$$

which enables us to determine $A(r)$ as

$$\begin{aligned} A(r) &= \left(1+\frac{r_s}{r}\right)^{-8\pi r_s^2\rho_s} \\ &\approx 1 - \frac{2M_D(r)}{r_s}\left(1+\frac{r_s}{r}\right)\log\left(1+\frac{r_s}{r}\right). \end{aligned} \tag{1.5}$$

For the DM halo itself (1.3), the Einstein field equation yields as ([50, 37]):

$$R_{\mu\nu} - \frac{1}{2}g_{\mu\nu}R = 8\pi T_{\mu\nu}(D)\,, \tag{1.6}$$

where the source part $T_{\mu\nu}(D)$ is given by

$$T_\mu^\nu(D) = g^{\nu\alpha}T_{\mu\alpha}(D) = \text{diag}[-\rho(r), P_r(r), P_t(r), P_t(r)]\,,$$

which stands for the energy-momentum tensor of the Dehnen type DM halo spacetime. Similarly, the line element for the BH spacetime, including the DM halo, can be written as a result of the combined BH-DM halo system

$$ds^2 = -\left[A(r)+F_1(r)\right]dt^2 + \frac{dr^2}{B(r)+F_2(r)} + r^2 d\Omega^2\,, \tag{1.7}$$

for which the Einstein field equation reads

$$R_{\mu\nu} - \frac{1}{2}g_{\mu\nu}R = 8\pi\left[T_{\mu\nu}(D) + T_{\mu\nu}(BH)\right]\,, \tag{1.8}$$

with the energy-momentum tensor $T_{\mu\nu}(BH)$ of the BH spacetime. For the combined BH-DM halo system, Einstein field equations can be written as follows: (1.6,1.8) and line elements (1.3,1.7) we will have:

$$\begin{aligned}\Big[B(r) &+ F_2(r)\Big]\Big[\frac{1}{r}\frac{B'(r)+F_2'(r)}{B(r)+F_r(r)}+\frac{1}{r^2}\Big]\\ &= B(r)\Big[\frac{1}{r}\frac{B'(r)}{B(r)}+\frac{1}{r^2}\Big],\end{aligned} \tag{1.9}$$

$$\begin{aligned}\Big[B(r) &+ F_2(r)\Big]\Big[\frac{1}{r}\frac{A'(r)+F_1'(r)}{A(r)+F_1(r)}+\frac{1}{r^2}\Big]\\ &= B(r)\Big[\frac{1}{r}\frac{A'(r)}{A(r)}+\frac{1}{r^2}\Big].\end{aligned} \tag{1.10}$$

Consequently, the above equations lead to the space-time metric, including the DM halo, which can be written as

$$\begin{aligned}ds^2 &= -\exp\left[\int\frac{B(r)}{B(r)-\frac{2M}{r}}\left(\frac{1}{r}+\frac{A'(r)}{A(r)}\right)dr\right]dt^2\\ &- A(r)dt^2+\frac{dr^2}{B(r)-\frac{2M}{r}}+r^2\left(d\theta^2+\sin^2\theta d\phi^2\right),\end{aligned} \tag{1.11}$$

It must be emphasized that one can recover $A(r)=B(r)=1$ in the case of vanishing DM halo, the resulting integral gives $(1-\frac{2M}{r})$ that exhibits the Schwarzschild BH solution with the mass $M$. As a result, Eqs. (1.9) and (1.10) solve to give

$$\begin{aligned}F_1(r) &= exp\Big[\int\left(\frac{B(r)}{B(r)+F_2(r)}\Big(\frac{1}{r}+\frac{A'(r)}{A(r)}\Big)-\frac{1}{r}\right)dr\Big]\\ &\quad -A(r)\,,\end{aligned} \tag{1.12}$$

$$F_2(r) = -\frac{2M}{r}\,, \tag{1.13}$$

where prime $'$ denotes derivative with respect to $r$. At this stage, we shall for simplicity consider the condition $A(r)=B(r)$, leading to the resulting spacetime metric describing the Schwarzschild-like BH with the DM halo characterized by

the Dehnen-type density distribution profile $(1, 4, 2)$. The resulting spacetime metric derived as the exact solution of the field equations (1.6) reads as

$$ds^2 = -f(r)dt^2 + \frac{1}{f(r)}dr^2 + r^2\left(d\theta^2 + \sin^2\theta d\phi^2\right) , \tag{1.14}$$

where

$$f(r) = 1 - \frac{2M}{r} - \frac{8\pi\rho_s r_s^2}{1+\frac{r_s}{r}}\left(1+\frac{r_s}{r}\right)\log\left(1+\frac{r_s}{r}\right). \tag{1.15}$$

We now turn to studying the behavior of $f(r)$ and demonstrate its radial dependence in Fig. 1.1, highlighting how it changes under the DM halo parameters. As can be seen from Fig. 1.1, the behavior of $f(r)$ reduces to the flat spacetime at larger distances, especially at infinity. Furthermore, the curves are slightly shifted to the right to larger $r$ as the DM halo parameters $\rho_s$ and $r_s$ increase, resulting in the strength of the gravitational potential increasing.

The spacetime Eq. (1.14) has an event horizon, where a corotating observer's 4-velocity becomes null, resulting from setting $f(r) = 0$. It is then straightforward to obtain the event horizon, $r_h$, in the form

$$r_h = \frac{r_s}{\frac{4\pi\rho_s r_s^3}{M}\,W\left(\frac{M\exp\left[\frac{2M+r_s}{8\pi\rho_s r_s^3}\right]}{4\pi\rho_s r_s^3}\right) - 1}, \tag{1.16}$$

where $W(z)$ is referred to as the Lambert function, defined as the principal solution of $W\exp(W) = z$ for arbitrary $z$. In Fig. 1.2, we show the behavior of the event horizon based on the density $\rho_s$ and the characteristic scale $r_s$ of the DM halo. From Fig. 1.2, one can easily observe that an increase in $\rho_s$ and $r_s$ leads to an increase in the event horizon. It can be seen from Eq. (1.2) that the DM halo parameters (i.e., $\rho_s$ and $r_s$) contribute to an increase in mass, enhancing the gravitational potential.

## 1.3 The spacetime curvature characteristics and energy conditions

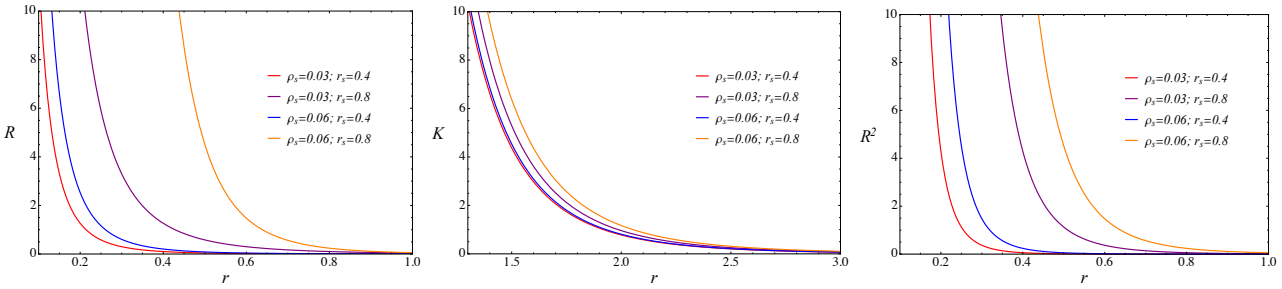


Figure 1.3: The Ricci scalar ($R$) (left panel), the Kretschmann scalar ($K$) (middle panel), and the square of the Ricci tensor ($R^2$) (right panel) as a function of $r$ for a Schwarzschild-like BH in a DM halo for varying $\rho_s$ and $r_s$ parameters.

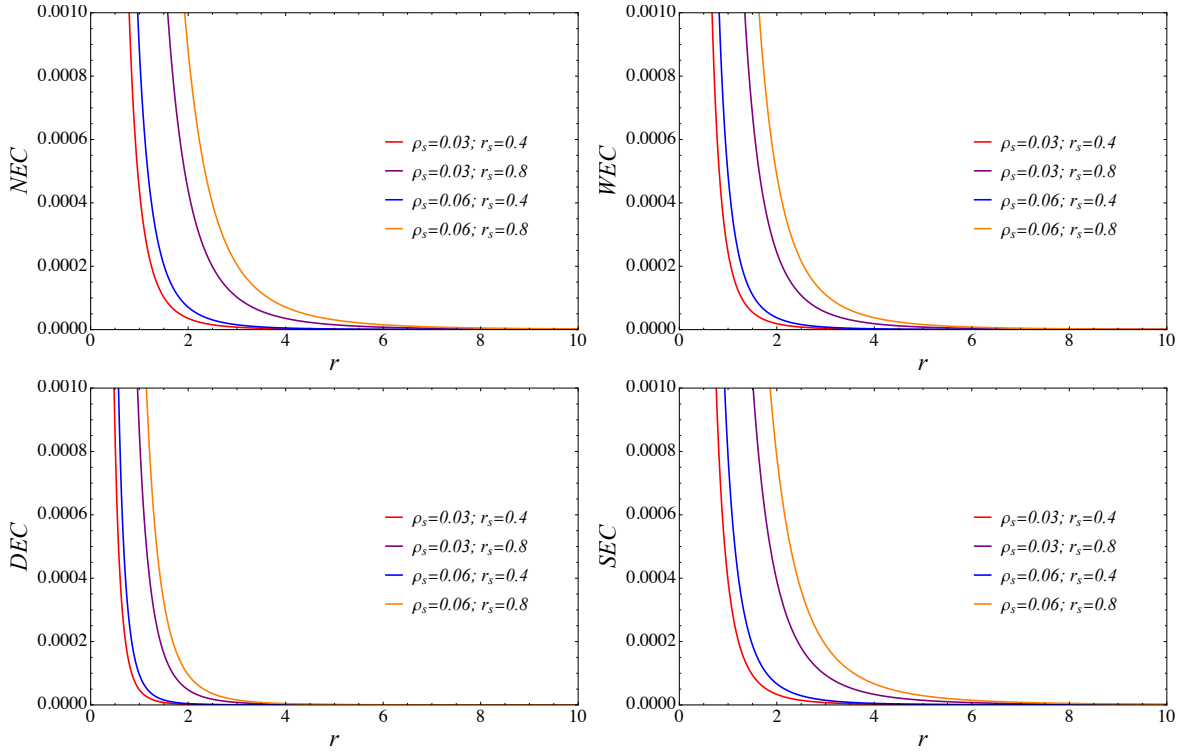


Figure 1.4: The radial dependence of the NEC (top left), WEC (top right), DEC (bottom left), SEC (bottom right) for varying $\rho_s$ and $r_s$ parameters.

Now we analyze the spacetime curvature invariants of a novel Schwarzschild-like BH spacetime metric with a DM halo characterized by a Dehnen-type density profile. To accomplish this, one needs to evaluate the curvature invariants of

the spacetime metric, including the Ricci scalar $R$, Ricci square $R_{\mu\nu}R^{\mu\nu}$, and Kretschmann scalars $R_{\mu\nu\alpha\beta}R^{\mu\nu\alpha\beta}$. To determine whether there is a spacetime singularity or not at $r = 0$, we further examine these fundamental invariants. We begin to analyze the Ricci scalar $R$, which for this BH-DM spacetime metric reads as

$$R = \frac{8\pi\rho_s r_s^2 \left[2\mathcal{N}\log\mathcal{F}^{\mathcal{F}} - r_s\mathcal{F}\mathcal{M}\right]}{r^4\mathcal{F}}\,. \tag{1.17}$$

It is obvious that the Ricci-flat for the Schwarzchild case (i.e., $\rho_s = 0$) but it is true in the BH-DM halo system halo. The Kretschmann scalar reads as follows:

$$\begin{aligned} K &= \frac{48M^2}{r^6} + \frac{64\pi M\rho_s r_s^2\left[\frac{r_s(4r+3r_s)}{(r+r_s)^2} + 2\log\mathcal{F}\right]}{r^5} \\ &+ O(\rho_s^2)\,, \end{aligned} \tag{1.18}$$

which reduces to the Schwarzschild case, $K = \frac{48M^2}{r^6}$, when $\rho_s = 0$. Meanwhile, the Ricci square reads as

$$\begin{aligned} R^2 &= \mathcal{A}\Big[\mathcal{B}\mathcal{F}^2 + 4r_s^2r^2\mathcal{F}^2\log\mathcal{F}\left(\mathcal{C}\log\mathcal{F} + \mathcal{D}\right) - 4r^2r_s\mathcal{F} \\ &\times \mathcal{G}\log\mathcal{F}^{\mathcal{F}} + \mathcal{H}\log^2\mathcal{F}^{\mathcal{F}}\Big]\,, \end{aligned} \tag{1.19}$$

Here we note that we use the following notations in Eqs. (1.17)-(1.19), which are

given by

$$\mathcal{A} = \frac{32\pi^2\rho_s^2 r_s^4}{r^4(r+r_s)^6}, \tag{1.20a}$$

$$\mathcal{F} = 1 + \frac{r_s}{r}, \tag{1.20b}$$

$$\mathcal{B} = r_s^2 r^2 \left(4r^2 + 8rr_s + 5r_s^2\right), \tag{1.20c}$$

$$\mathcal{C} = \left(r^2 + 2rr_s + 2r_s^2\right), \tag{1.20d}$$

$$\mathcal{D} = 2r^2 + 4rr_s + 3r_s^2, \tag{1.20e}$$

$$\mathcal{G} = \Big[2r^3 + 8r^2 r_s + 2\left(r^3 + 4r^2 r_s + 5rr_s^2 + 3r_s^3\right) \tag{1.20f}$$

$$\times \log\mathcal{F} + 10rr_s^2 + 5r_s^3\Big], \tag{1.20g}$$

$$\mathcal{H} = 4r^2\left(r^4 + 6r^3 r_s + 13r^2 r_s^2 + 12rr_s^3 + 5r_s^4\right), \tag{1.20h}$$

$$\mathcal{N} = \left(r^2 + 3rr_s + 3r_s^2\right), \tag{1.20i}$$

$$\mathcal{M} = \left[2(r+2r_s)\log\mathcal{F} + 2r + 3r_s\right]. \tag{1.20j}$$

From these equations, one can deduce that the spacetime singularity appears at $r = 0$. Furthermore, we show the radial behavior of these curvature invariants in Fig. 1.3. Also, the behavior of the spacetime singularity is clearly seen in Fig. 1.3. These curvature invariants, respectively, approach zero and infinity when $r \to \infty$ and $\to 0$, i.e.,

$$\lim_{r\to\infty} R, R_{\mu\nu}R^{\mu\nu}, R_{\mu\nu\alpha\beta}R^{\mu\nu\alpha\beta} \to 0\,, \tag{1.21}$$

and

$$\lim_{r\to 0} R,\ R_{\mu\nu}R^{\mu\nu},\ R_{\mu\nu\alpha\beta}R^{\mu\nu\alpha\beta} \to \infty\,. \tag{1.22}$$

The energy conditions are also considered to be fundamental characteristics of spacetime, like the curvature invariants. Here, we provide some insight by analyzing the corresponding energy conditions.

We then turn to solving Einstein's Eq. (1.6) together with the energy-momentum tensor $T_\mu^\nu = \text{diag}[-\rho(r), P_r(r), P_\theta(r), P_\phi(r)]$. Consequently, we derive the stress-

energy tensor elements as

$$-\rho(r) = P_r(r) = \frac{M_D(r)}{4\pi r^3}\Big[1 - \log\left(1 + \frac{r_s}{r}\right)^{(1+\frac{r}{r_s})}\Big], \tag{1.23}$$

$$P_\theta(r) = P_\phi(r) = \frac{M_D(r) r_s}{8\pi r^3 (r + r_s)}\,.$$

Taking the above equations into consideration, we further examine energy conditions for the source fluid. It is worth noting that the stress-energy tensor must satisfy certain inequalities. Therefore, we further consider the null, weak, dominant, and strong energy conditions.

- The null-energy condition (NEC) is a fundamental requirement in GR and plays a crucial role in the study of gravitational physics. It ensures that the energy density associated with matter and fields in spacetime is always positive or zero, preventing the occurrence of exotic phenomena such as negative energy densities or violations of energy conditions. The NEC is a key ingredient in the formulation of the Einstein field equations and is essential for maintaining the consistency and physical viability of the theory. Taken all together, the NEC implies [52, 37]:

$$T_{\mu\nu} n^\mu n^\nu \geq 0, \tag{1.24}$$

or

$$\rho(r) + P_i(r) \geq 0, \quad (i = r, \theta, \phi),$$

where $n^\alpha$ is the null vector. One can easily conclude from Eq. (1.23) that $P_r(r) + \rho(r) = 0$ and:

$$\rho(r) \quad + \quad P_\beta(r) = \tag{1.25}$$

$$= \frac{\rho_s r_s^3 \left[\log\left(1 + \frac{r_s}{r}\right)^{2r_s(1+\frac{r}{r_s})^2} - 2r - r_s\right]}{2r^2(r + r_s)^2}\,,$$

with $\beta = \theta, \phi$. From Eq.(1.25) it is obvious:

$$\lim_{r\to 0}[\rho(r) + P_\beta(r)] = \infty, \tag{1.26}$$

$$\lim_{r\to \infty}[\rho(r) + P_\beta(r)] = 0.$$

The behavior of the NEC is demonstrated in Fig 1.4 for various possible cases of the DM halo parameters.

- The weak energy condition (WEC) is also a fundamental requirement in GR and imposes the requirement that the total energy density measured by an observer traversing a timelike curve cannot be negative, which implies [52, 37]:

$$\rho \geq 0,\ \ \rho(r) + P_i(r) \geq 0,\ \ \ (i = r, \theta, \phi). \tag{1.27}$$

We depict the behavior of the WEC in Fig. 1.4 for various possible cases.

- The dominant energy condition (DEC) states that for any future-directed causal vector field (whether timelike or null), the vector $-T^\mu_\nu \mathbf{Y}^\nu$ must also be a future-directed causal vector. This condition, which is stronger than the WEC, physically implies that the local energy density is non-negative and that energy flux cannot propagate faster than light relative to any local observer. The DEC implies following condition [37]:

$$\rho(r) - |P_{\theta,\phi}| \geq 0, \tag{1.28}$$

$$\frac{\rho_s r_s^3 \left[2(r+r_s)\log\left[\left(1+\frac{r_s}{r}\right)^{1+\frac{r}{r_s}}\right] - 2r - 3r_s\right]}{2r^2(r+r_s)^2} \geq 0\,.$$

The above equation guarantees the satisfaction of this energy condition. Similar behavior is also shown in Fig. 1.4 for various possible cases.

- Finally, the strong energy condition (SEC) can be determined by [37]

$$(T_{\mu\nu} - \frac{1}{2}Tg_{\mu\nu})n^{\mu}n^{\nu} \geq 0, \tag{1.29}$$

or

$$\rho + \sum_{i=1}^{3} P_i \geq 0,$$

which gives

$$\frac{\rho_s r_s^4}{r^2(r+rs)^2} \geq 0\,. \tag{1.30}$$

Based on the above analysis of the energy conditions, we obtain compelling results indicating that all energy conditions are well satisfied. This conclusion is further supported by a graphical analysis for the obtained BH spacetime metric within a Dehnen-type DM halo, presented in Eq. 1.14. Additionally, we present a clear analysis that illustrates the radial behavior of NEC, WEC, DEC, and SEC, as seen in Fig. 1.4. Both analytical and graphical investigations consistently confirm the validity of all energy conditions.

## 1.4 Conclusion

BHs interact gravitationally with their surrounding environments, making the study of BH-DM systems increasingly important task in astrophysical contexts. It is widely believed that supermassive BHs at the centers of galaxies are embedded in complex, dynamic matter distributions, including DM halos [8, 9, 10, 11, 16, 6]. Motivated by this, we derived a novel analytical Schwarzschild-like BH solution, representing a static BH surrounded by a DM halo characterized by a Dehnen-type density profile $(1, 4, 2)$.

We first investigated the properties of this BH by analyzing the spacetime curvature properties. Specifically, we computed the curvature invariants of the

spacetime metric to determine the presence of singularities. Our results indicated that a spacetime singularity appears at $r = 0$, as illustrated in Fig. 1.3. We also examined the energy conditions, which are fundamental characteristics of the physical viability of spacetime. Our analysis showed that all energy conditions are well satisfied for the derived BH solution within the Dehnen-type DM halo. This conclusion was further supported by graphical results, as presented in Fig. 1.4, with analytical and graphical analyzes consistently confirming the validity of all energy conditions.

Our approach offers fundamental astrophysical implications, particularly concerning the significant role of DM halos around supermassive BHs in galactic nuclei. Specifically, the Dehnen-type density distribution used here supports the existence of a BH solution with a DM halo within the density profile $(1, 4, 2)$. Our finding could offer a novel perspective on the formation of DM halos, providing a potential alternative framework for understanding their fundamental properties.

# Chapter II

# Dynamics of gravitational objects in supermassive black hole environment.

## 2.1 Lyapunov exponents. Timelike geodesics around Schwarzschild-like black hole immersed in Dehnen-type dark matter halo

In this chapter we start with analyzing the trajectory of a particle with mass $m$, total energy $E$, and angular momentum $L$ in the vicinity of a Schwarzschild-like BH in the DM halo, we start with the Hamilton-Jacobi equation [53, 40, 41]:

$$g^{\mu\nu}\frac{\partial S}{\partial x^{\mu}}\frac{\partial S}{\partial x^{\mu}} = -m^2\,, \tag{2.1}$$

where $S = -Et + L\phi + S(r)_r + S_\theta(\theta)$ is the Hamilton-Jacobi action. Subsequently, we can express the Lagrangian of a test particle as:

$$\mathcal{L} = \frac{1}{2} m g_{\mu\nu} u^{\mu} u^{\nu}\,, \tag{2.2}$$

which enables us to find the four-momenta as:

$$p_{\mu} = \frac{\partial \mathcal{L}}{\partial \dot{x}} = m g_{\mu\nu} u^{\nu}\,. \tag{2.3}$$

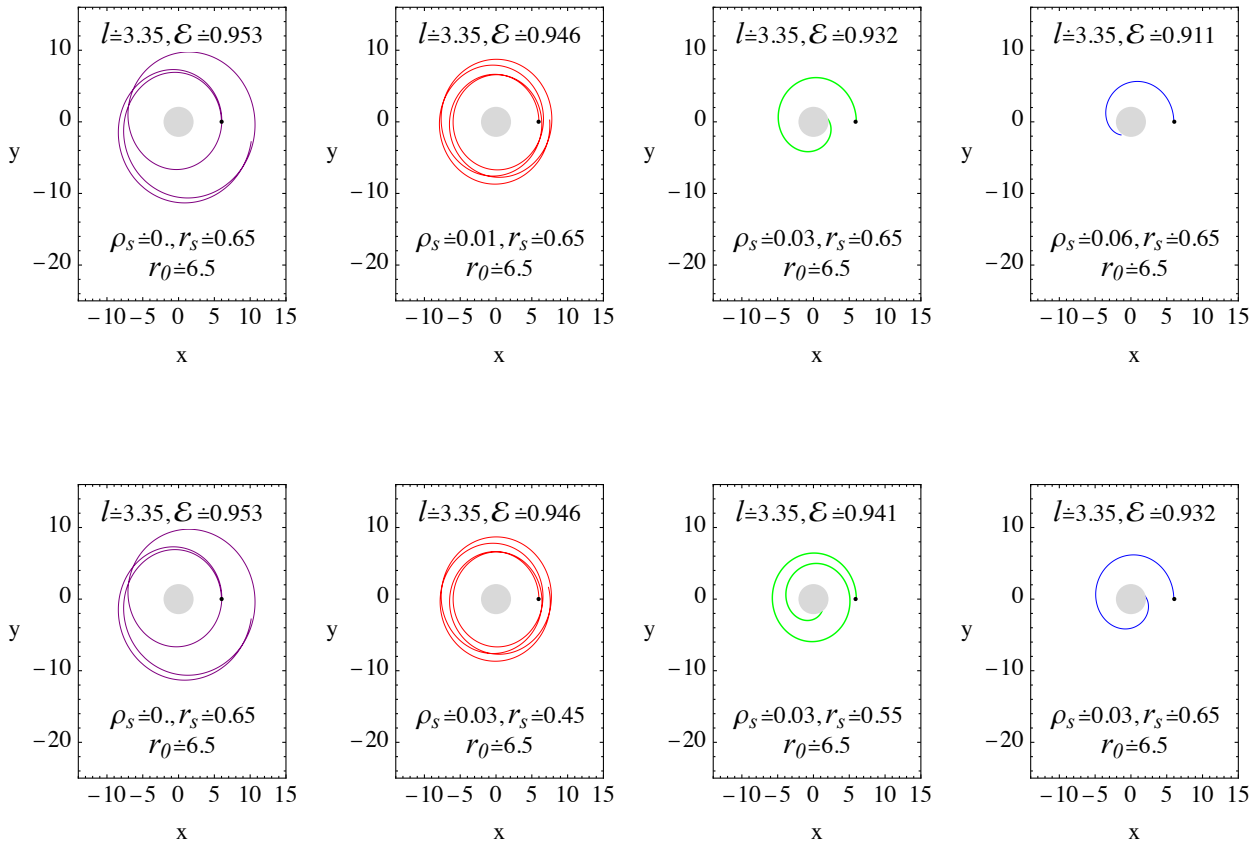


Figure 2.1: The trajectories of the timelike particle in the vicinity of a Schwarzschild-like BH in a DM halo for varying $\rho_s$ and $r_s$ parameters.

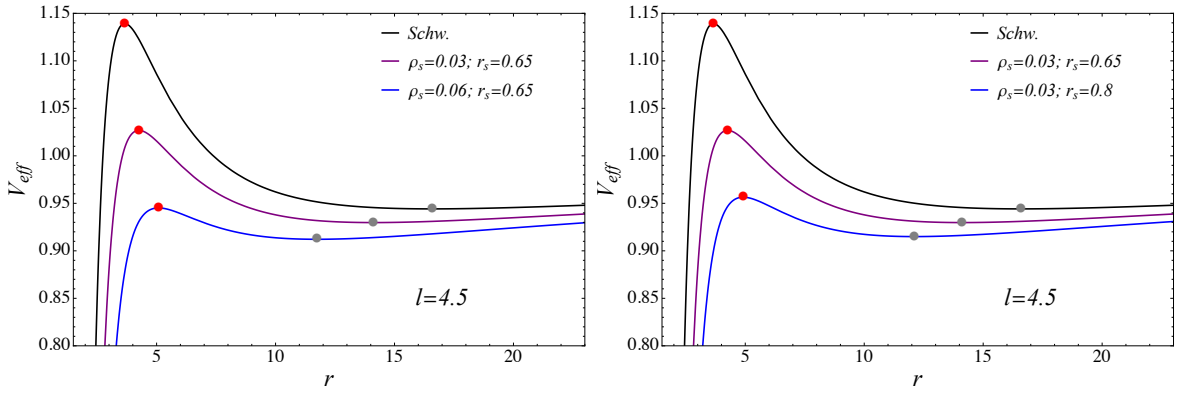


Figure 2.2: The radial dependence of the effective potential for varying DM halo parameters, $\rho_s$ and $r_s$. Here, we note note that red and gray points indicate unstable and stable circular orbits, respectively.

Based on the above equations, we illustrate the trajectory of test particles starting from a point $r_0$ with the appropriate specific energy $\mathcal{E} = \frac{E}{m}$ and angular

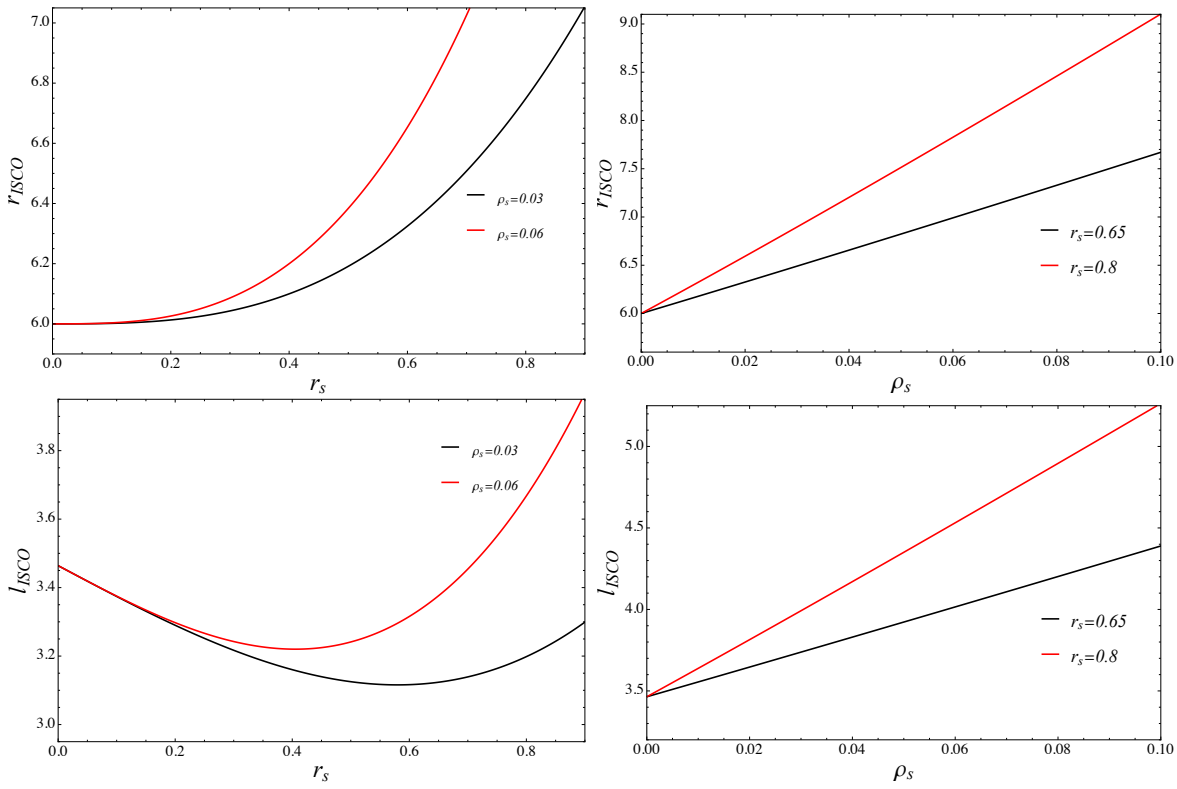


Figure 2.3: The ISCO parameters, $r_{ISCO}$ (top row) and $l_{ISCO}$ (bottom row) of the timelike particles are plotted as a function of the density $\rho_s$ and characteristic scale $r_s$ of the DM halo.

momentum $l = \frac{L}{m}$ [1], as shown in Fig 2.1. It can be observed that there are two types of orbits in Fig. 2.1: captured and bound orbits. An increase in the values of the DM halo parameters, $\rho_s$ and $r_s$, results in the orbits becoming captured.

For further analysis, we shall confine the motion to the equatorial plane (i.e., $\theta = \frac{\pi}{2}$):

$$\dot{t} = -\frac{\mathcal{E}}{f(r)}\,, \tag{2.4a}$$

$$\dot{\phi} = \frac{l}{r^2}\,, \tag{2.4b}$$

$$\dot{r}^2 = \mathcal{E}^2 - V_{eff}(r)\,, \tag{2.4c}$$

where the effective potential, $V_{eff}(r)$, is given by

$$V_{eff}(r) = \left[1 - \frac{2M}{r} - \frac{2M_D(r)}{r_s}\left(1 + \frac{r_s}{r}\right) \times \log\left(1 + \frac{r_s}{r}\right)\right]\left(1 + \frac{l^2}{r^2}\right)\,. \tag{2.5}$$

We further examine the effective potential, $V_{\rm eff}$, for the timelike particles around the BH in the DM halo characterized by the Dehnen-type density profile, highlighting how the presence of the novel Dehnen-type DM halo affects the gravitational dynamics and modifies particle trajectories. To accomplish this, we illustrate the radial behavior of the effective potential for various possible cases, as shown in Fig. 2.2. As can be seen from Fig. 2.2, it is evident that the effective potential has two extreme points that correspond to stable circular and unstable circular orbits. It can be observed from Fig. 2.2 that an increase in the density $\rho_s$ and characteristic scale $r_s$ of the DM halo results in both stable and unstable circular orbits of the particles expanding in the BH- DM halo system. It should also be noted that the effective potential curves exhibit a slight rightward shift, indicating larger radial distances $(r)$, while the potential maximum decreases with increasing $\rho_s$ and $r_s$, as seen in Fig. 2.2.

We now turn to studying the innermost stable circular orbits (ISCOs). For the timelike particles to be on the ISCO, one need to solve the following equations simultaneously [54, 55]

$$V_{eff} = \mathcal{E}^2_{ISCO}, \ \frac{\partial V_{eff}}{\partial r} = \frac{\partial^2 V_{eff}}{\partial r^2} = 0\,. \tag{2.6}$$

We now proceed to analyze the behavior of the ISCO radii for particles orbiting around the Schwarzschild-like BH surrounded by the Dehnen-type DM halo. In Fig. 2.3, we highlight how the ISCO parameters, specifically the energy $\mathcal{E}_{ISCO}$ and the angular momentum $l_{ISCO}$ of the timelike particles, are influenced by the presence of the DM halo. As shown in Fig. 2.3, an increase in the DM halo $\rho_s$ leads to a corresponding increase in both $r_{ISCO}$ and $l_{ISCO}$ of timelike particles on the ISCO around the BH. Similarly, increasing the characteristic scale $r_s$ results in a larger $r_{ISCO}$ radius; however, $l_{ISCO}$ initially decreases until a critical value of $r_s$ is reached, after which it begins to increase again, as depicted in Fig. 2.3.

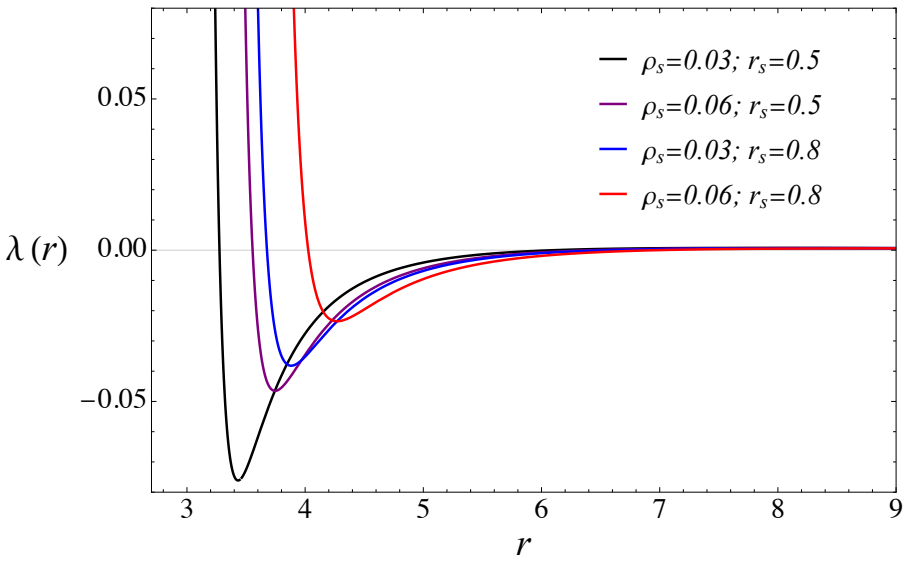


Figure 2.4: Radial profile of the Lyapunov exponent for varying the density $\rho_s$ and characteristic scale $r_s$ of the DM halo.

Finally, we turn to examining the Lyapunov exponent, which is a powerful tool for understanding the stability of timelike particles. Hereafter, we analyze the Lyapunov exponent to study the stability (instability) of the circular orbits for timelike particles in the vicinity of the Schwarzschild-like BH in the DM halo [56]:

$$\lambda = \sqrt{-\frac{\partial_r^2 V_{eff}}{2\dot{t}^2}}\,. \tag{2.7}$$

Additionally, we use requirements for circular orbits, $\mathcal{E}^2 = V_{eff}(r)$ and $\frac{\partial V_{eff}}{\partial r} = 0$, which solve to gives

$$\mathcal{E}^2 = \frac{2f^2(r)}{2f(r) - rf'(r)}\,, \tag{2.8a}$$

$$l^2 = \frac{r^3 f'(r)}{2f(r) - rf'(r)}\,, \tag{2.8b}$$

where $'$ denotes a derivative with respect to $r$.

To better understand the Lyapunov exponents, we present the radial profile of $\lambda$ in Fig. 2.4. As shown in Fig. 2.4, the radii of stable ($\lambda < 0$) and chaotic ($\lambda > 0$) orbits of the timelke particles grow when the density $\rho_s$ and the characteristic

scale $r_s$ of the DM halo are increased, coinciding with the analysis of the effective potential $V_{eff}(r)$, as depicted in Fig. 2.2. In particular, bifurcation points occur when the curves intersect the horizontal axis (that is, $\lambda = 0$), making the ISCO location. From Fig. 2.4, as a consequence of an increase in the DM halo parameters, $\rho_s$ and $r_s$, both the Lyapunov exponent curves and the corresponding stable circular orbits shift to the right to larger radial distances, as also reflected in Fig. 2.3.

## 2.2 Particle dynamics and the accretion disk around a Self-dual black hole immersed in a magnetic field in Loop Quantum Gravity

Even though GR has been considered the most successful theory of gravity, it has faced notable theoretical and observational challenges. From a theoretical point of view, GR's lack of incorporation of quantum principles hinders its unification with quantum mechanics, a significant unresolved issue [57, 58]. Furthermore, GR predicts singularities, points where known physics breaks down, both at the universe's inception [59, 60] and within BH spacetimes [61]. Observationally, GR struggles to explain phenomena such as DM and dark energy. All these issues indicate that the classical GR might need to be modified. In particular, the spacetime singularities ought to be resolved after quantum gravitational effects are taken into account. These challenges motivate the exploration of modified gravity theories and quantum gravity as potential solutions. Rigorous testing of these modified theories is crucial to determine which, if any, can ultimately provide a comprehensive and accurate model of gravity.

LQG presents an elegant solution to classical Big Bang and BH singularities. Recently, a regular static spacetime metric known as the self-dual spacetime has

been derived within a mini-superspace framework using the polymerization procedure in LQG [62]. This spacetime demonstrates regularity and lacks any spacetime curvature singularity. The polymerization procedure in the quantization of the BH spacetime introduces two intrinsic parameters: the minimal area and the Barbero-Immirzi parameter, which control the quantum effects on the self-dual spacetime. Furthermore, it has been shown that this spacetime exhibits self-duality, aligning with T-duality principles [63, 64]. This is also the reason that we call it the self-dual spacetime. In recent years, extensive research has focused on the quantum extensions of BHs within the LQG framework, with notable references including [65, 66, 67, 68, 69, 70, 71]. For a more comprehensive understanding, readers are encouraged to explore review articles such as [72, 73, 74, 75, 76].

The quantum effects on the self-dual spacetime are controlled by the two intrinsic parameters: the minimal area and the Barbero-Immirzi parameter. This raises the intriguing question of whether these quantum effects can leave any observational signatures for the current and/or forthcoming experiments so that the quantum effects can be tested or constrained directly. Such considerations have resulted in a flourish of studies during the past decades from different kinds of experiments and observations [77, 78, 79, 80, 81, 64, 82, 83, 84, 85, 86, 87, 88]. For instance, a detailed exploration in [87] elaborates on how the quantum effects of LQG can impact the shadow of a rotating BH, offering comparisons with the latest observations by the Event Horizon Telescope (EHT) of the supermassive BH M87*. Furthermore, the gravitational lensing in the self-dual spacetime has been under scrutiny, with the polymeric function from LQG being constrained using data from geodetic very-long-baseline interferometry measurements of the solar gravitational deflection of radio waves [64]. Recent studies, like those in [88], have extended this investigation to the solar system, deriving observational constraints on the polymeric function $P$ of LQG. It is interesting to note that

the phenomenological study of the self-dual BH and other types of loop quantum BHs has also been extensively explored, see [89, 90, 91, 92, 93, 94, 95, 96, 97, 98, 99, 100, 101, 102, 103, 104, 105, 106] and references therein.

In this chapter, we consider a self-dual BH in LQG in the presence of an external magnetic field. To understand the nature of spacetime geometry we analyze the effects of a new quantum correction parameter and existing fields in the surrounding environment. For that, we investigate the motion of particles with magnetic dipole moment and electrically charged particles around the aforementioned spacetime geometry.

The important point to note is that the solution of either GR or alternative theories of gravity can be tested through astrophysical processes, such as X-ray data [107, 108] and the accretion disk [109] with recent observations [110, 111, 112] around astrophysical compact objects, playing a pivotal role as very useful tests. On the other hand, as one possible attempt, it is also valuable to analyze the motion of test particles around compact objects to understand more deeply their unique aspects. The particle motion can also be used to model the accretion disk [113, 114]. Therefore, the aforementioned tests may come into play to reveal unknown aspects of astrophysical compact objects and to provide some departures from their expected behaviors. It is to be emphasized that, from an astrophysical viewpoint, the presence of external magnetic fields can play a pivotal role in determining the motion of charged particles in the vicinity of compact objects. The effects of electromagnetic fields have been widely considered and examined on test particles with an electric charge and with a nonzero magnetic dipole moment around BHs in different gravity theories [115, 116, 117, 39, 118, 119, 120, 121, 122, 123, 124, 125, 126, 127, 128, 129, 40, 130, 131, 132].

In an astrophysical scenario, a BH does not have its own magnetic field due to gravitational collapse, which decays at least with $t^1$ in the quasistationary ap-

proach (see, for example, [133, 134]). However, one can assume existence of an external test magnetic field that can be produced by nearby objects, e.g., accretion disks existing around rotating BHs [135], neutron stars [115, 133, 136], and magnetars [137, 138]. The magnetic field existing in the surrounding environment was estimated to be of the order of $B_1 \sim 10^8$ G for stellar and $B_2 \sim 10^4$ G for supermassive black holes, respectively (see, e.g., [139, 140, 141]). It does not significantly distort the spacetime geometry, so it can be considered a test field that satisfies $B_{1,2} \ll B_{max} \sim 10^{19}(M_\odot/M)$ G. However, recent observational findings from EHT on M87 regarding the magnetic field strength around BHs reported that the magnetic field is of the order of $B \sim 33.1 \pm 0.9$ G in the corona for the binary BH system $V404$ Cygni [142]. Additionally, EHT collaborations announced in their report that the average magnetic field strength is of the order of $B \sim 1 - 30$ G in the emission region around the supermassive BH of the M87 galaxy [143, 144]. In this dissertation, we explore properties of the self-dual BH in LQG immersed in an external magnetic field, which is asymptotically uniform at large distances and oriented along the $z$-axis. However, it should be emphasized that, in a realistic astrophysical scenario, the magnetic field can have a complex configuration in the close vicinity of a BH, especially very close to its horizon, but it can be approximated as a uniform field at a specific distance, particularly in a local part of space. This is a well-accepted approximation for magnetic fields in the surrounding environment of BHs. For example, the magnetic field generated by a current loop in the accretion disk around the BH can be approximated to be uniform provided that the BH size is much smaller compared to the disk size (see, e.g., [145, 146]). Additionally, the magnetic field can be considered as a nearly uniform field when the BH is located at a sufficient distance away from the equatorial plane of a magnetar [138, 147]. These investigations suggest that the magnetic field can be regarded as an asymptotically uniform magnetic field at a

relatively far distance.

This section is organized as follows: In Subsec. 2.3, we briefly discuss a BH spacetime in LQG and the surrounding magnetic field properties. In Subsec. 2.4, we study the motion of particles with a magnetic dipole moment, which is followed by the study of dynamics of electrically charged particles around a self-dual BH immersed in an external uniform magnetic field in Subsec. 2.5. In 3.7, we consider the solution of field equations associated with the magnetic field existing in the environment surrounding a self-dual black hole in LQG.

## 2.3 Loop quantum black hole immersed in the external uniform magnetic field

We begin with an introduction to the quantum corrected Schwarzschild spacetime in LQG proposed in Ref. [62], commonly referred to as the self-dual spacetime. In effective models of BHs within LQG, a polymer-like quantization method is typically employed. This approach involves replacing the canonical variables $(b, c)$ in the phase space of BH spacetime with their regularized counterparts: $b \to \frac{\sin(\delta_b b)}{\delta_b}$ and $c \to \frac{\sin(\delta_c c)}{\delta_c}$. The parameters $\delta_b$ and $\delta_c$ are quantum polymeric parameters that determine the scales at which quantum effects manifest in LQG. In the limit where $\delta_b, \delta_c \to 0$, the classical physics is recovered. However, a complete theory of quantum gravity is not yet available, and thus, a comprehensive framework for choosing $\delta_b$ and $\delta_c$ remains unclear. In this paper, we explore the self-dual spacetime arising from a specific choice that treats $\delta_b$ and $\delta_c$ as constants, known as the $\mu_0$-scheme in LQG. Ref. [62] demonstrates that identifying the minimal area in the solution with the minimum area $A_{\rm min}$ of LQG allows for one of the free parameters to be reduced. Consequently, in the self-dual spacetime, the LQG effects are characterized by two parameters: the minimal area $A_{\rm min}$ and the polymeric parameter $\delta$ (where $\delta_b$ is denoted as $\delta$ hereafter).

The effective metric of the self-dual BH in LQG is given by [62]

$$d\tau^2 = -A(r)dt^2 + \frac{dr^2}{B(r)} + C(r)(d\theta^2 + \sin^2\theta d\phi^2), \tag{2.9}$$

where $A(r)$, $B(r)$, $C(r)$ are given by

$$\begin{aligned} A(r) &= -g_{tt} = \frac{(r-r_+)(r-r_-)(r+r_*)^2}{r^4+a_0^2}, \\ B(r) &= \frac{1}{g_{rr}} = \frac{(r-r_+)(r-r_-)r^4}{(r+r_*)^2(r^4+a_0^2)}, \\ C(r) &= \frac{g_{\phi\phi}}{\sin^2\theta} = r^2 + \frac{a_0^2}{r^2}, \end{aligned} \tag{2.10}$$

where $r_+ = 2M/(1+P)^2$ and $r_- = 2MP^2/(1+P)^2$ refers to the BH's two horizons, while $r_* = \sqrt{r_+ r_-} = 2MP/(1+P)^2$ with ADM mass $M$ of the BH. Here, we only restrict ourselves to the outer horizon. We note here that the function $P$ stemming from quantum correction is given by

$$P \equiv \frac{\sqrt{1+\varepsilon^2}-1}{\sqrt{1+\varepsilon^2}+1}. \tag{2.11}$$

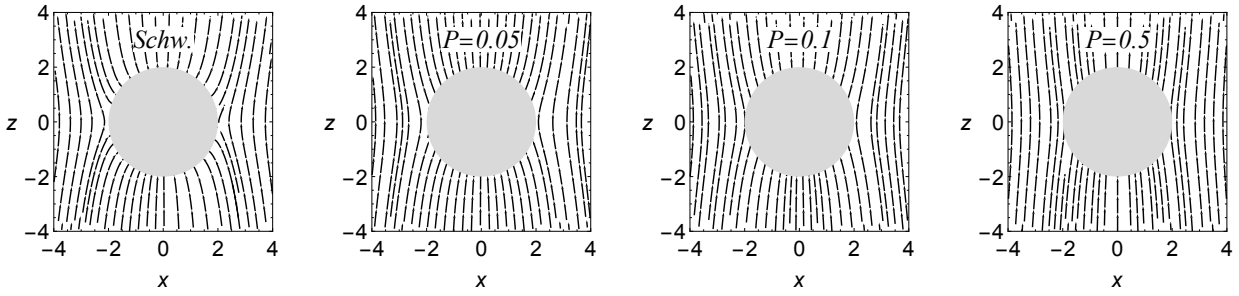


Figure 2.5: The plot shows the magnetic field lines in the vicinity of the self-dual BH in LQG for various combinations of the quantum correction parameter $P$, referred to as $\epsilon = 0.3571$ and $\epsilon = 0.4707$, respectively.

Here, $\varepsilon = \gamma\delta$ denotes a product of the Immirzi parameter $\gamma$ and the polymeric parameter $\delta$ which is introduced to define the paths one integrates the connection along to define the holonomies in the quantum corrected Hamiltonian constraint in the polymerization procedure in LQG, satisfying $\varepsilon < 1$. The point to be noted is that we further focus on $P$ only to explore the quantum effects resulting

from LQG. The $a_0$ parameter is defined by the equation $a_0 = \frac{A_{min}}{8\pi}$ with $A_{min} \approx 4\pi\gamma\sqrt{3}l_{Pl}^2$ refers to the minimum area gap of LQG. Here, $l_{Pl}$ is the Planck length. The Planck length can be considered negligible. Therefore we consider $a_0 = 0$. Here our main objective is to examine a charged particle motion in the close vicinity of the LQG black hole in the presence of an external magnetic field that refers to as asymptotically uniform with the strength $B_0$. To that end, we further need to find the four potential of the electromagnetic field, $A^\mu$. Following [135, 148], we assume the magnetic field to be uniform and oriented along the axis of symmetry of the LQG black hole due to its asymptotic properties. In doing so, one can write the vector potential's ansatz for a non-rotating BH as follows:

$$A^\mu = c_t(r, B_0)\xi_t^\mu + \left[\frac{B_0}{2} + c_\phi(r, B_0)\right]\xi_\phi^\mu \,, \tag{2.12}$$

where $\xi_t^\mu = (1, 0, 0, 0)$ and $\xi_\phi^\mu = (0, 0, 0, 1)$ refer to the time-like and space-like killing vectors. The explicit form of $A^\mu$ can be determined as a solution of the source-free Maxwell equations [148]. For a non-rotating vacuum BH the Maxwell field equations can be defined by $F^{\phi\nu}_{;\nu} = 0$ with the electromagnetic field tensor $F_{\mu\nu} = \partial_\mu A_\nu - \partial_\nu A_\mu$. One can then write the Maxwell field equation for $A^\mu$ in the LQG spacetime as follows:

$$A^{\phi;\nu}_{;\nu} - R^\phi_\nu A^\nu = 0 \,. \tag{2.13}$$

Similarly, the same form is satisfied for Killing vector $\xi$, and it is written as

$$\xi^{\mu;\nu}_{;\nu} - R^\mu_\nu \xi^\nu = 0 \,, \tag{2.14}$$

with the Ricci tensor $R_{\mu\nu}$. Eq. (2.14) takes the simpler form in the case of source-free satisfying the condition with Ricci tensor vanished, i.e., $\Box\xi^\mu = 0$ that can then be extended the same form of the Maxwell equation, $\Box A^\mu = 0$. Based on the equations underlined above with Eq. (2.12) one can have the following differential

equation:

$$C''_{\phi}r^2(r-r_+)(r-r_-)+C'_{\phi}r\left[2(r_+r_--2r^2)\right.$$
$$\left.-3r(r_++r_-)\right]-2C_{\phi}(r_+r_-+r_*(r_*+2r))=0, \tag{2.15}$$

where we have denoted $C_{\phi}=\left[\frac{B_0}{r}+c_{\phi}(r,B_0)\right]$. Note that $'$ and $''$ denote the first and second derivatives with respect to $r$. We provide details in relation to solution of the above equation in 3.7. Here, solving Eq.(2.15) yields to the solution for the four potential as:

$$A^{\mu}=\frac{B_0}{2}(\mathcal{B})^{\mathcal{A}}\ {}_2F_1\left(\mathcal{A},\mathcal{A}+3;2\mathcal{A}+3;\mathcal{B}\right)\xi^{\mu}_{\phi}. \tag{2.16}$$

Here, ${}_2F_1(a,b;c;z)=\Sigma_{n=0}^{\infty}\frac{(a)_n(b)_n}{(c)_n}\frac{z^n}{n!}$ is the Hypergeometric function, while $\mathcal{A}=\sqrt{\frac{1-2P}{1+2P}}-1$ and $\mathcal{B}=\frac{r(1+4P)}{2M(1+2P)}$ refer to new variables, as introduced in 3.7. It is obvious that for $P=0$ the four potential is reduced to the Schwarzschild case, i.e., $A_{\phi}=\frac{1}{2}B_0r^2\sin^2\theta$. In Fig. 2.5, we demonstrate the magnetic field lines in the vicinity of the self-dual BH in LQG. From Fig. 2.5, one can observe that the quantum correction parameter $P$ can influence the magnetic field lines in the close vicinity of the self-dual BH, compared to the Schwarzschild BH case. On the basis of the four potential Eq. (2.16), it is straightforward to obtain non-vanishing components of electromagnetic tensors, and they are given as follows:

$$\begin{aligned}F_{r\phi} &= \frac{(\mathcal{B})^{\mathcal{A}}}{2}B_0r\sin^2\theta\\ &\times \left[\frac{\mathcal{B}\mathcal{C}r\ {}_2F_1\left(\mathcal{A}+1,\mathcal{A}+4;2(\mathcal{A}+2);\mathcal{B}\right)}{\Xi}+\right.\\ &+ \left.(\mathcal{A}+2)_2\,F_1\left(\mathcal{A},\mathcal{A}+3;2\mathcal{A}+3;\mathcal{B}\right)\right],\end{aligned} \tag{2.17}$$

$$F_{\theta\phi}=\frac{(\mathcal{B})^{\mathcal{A}}}{2}B_0r^2\ \sin 2\theta\times\ {}_2F_1\left(\mathcal{A},\mathcal{A}+3;2\mathcal{A}+3;\mathcal{B}\right). \tag{2.18}$$

It is to be emphasized here that we denote new variables, such as $\mathcal{C}=\sqrt{1-4P^2}-6P-1$ and $\Xi=2\sqrt{1-4P^2}+2P+1$. In doing so, we can then unable to find the magnetic field components using $B^{\beta}=-\frac{1}{\sqrt{-g}}\epsilon^{\alpha\beta\sigma\gamma}F_{\sigma\gamma}u_{\alpha}$. Here, $g$ is

the determinant of the metric Eq. (2.9) and $\epsilon^{\alpha\beta\sigma\gamma}$ the pseudo-tensorial form of the Levi-Civita symbol and $u_\alpha$ the four velocity of the observer. After that the orthonormal component of the magnetic field can be obtained as

$$B^{\hat{\theta}} = \frac{F_{r\phi}}{\sqrt{g_{rr}g_{\phi\phi}}}. \tag{2.19}$$

Here we assume that a distant observer is located at zero angular momentum observer (ZAMO). Therefore, the normalization condition, $u_\alpha u^\alpha = -1$, allows to find $u_t = \frac{1}{\sqrt{-g^{tt}}}$.

We further investigate the particle dynamics for two different cases around the BH in LQG in the presence of an external magnetic field. This is what we intend to examine in the next section.

## 2.4 The motion of particles with nonzero magnetic dipole moment near a self-dual black hole immersed in an external magnetic field in Loop Quantum Gravity

We now consider the motion of particles with a magnetic dipole moment around the BH in LQG immersed in an external magnetic field. To that end we write the Hamilton-Jacobi equation for the particle interacting with the magnetic field, i.e., it is given by ([115, 149]):

$$g^{\mu\nu}\frac{\partial S}{\partial x^\mu}\frac{\partial S}{\partial x^\nu} = -m^2\left(1 - \frac{\mathcal{U}}{m}\right), \tag{2.20}$$

where $\mathcal{U} = D^{\mu\nu}F_{\mu\nu}$ refers to the magnetic interaction as a product of the polarization tensor $D^{\mu\nu}$ and electromagnetic tensor $F_{\mu\nu}$, which can also be defined by $\mathcal{U} = \mu_{\hat{\alpha}}B^{\hat{\alpha}}$. Following to [150], the Lagrangian of the system for a magnetized particle motion is written as follows

$$\mathcal{L} = \frac{1}{2}(m + \mathcal{U})g_{\mu\nu}u^\mu u^\nu - \frac{1}{2}\mathcal{U}. \tag{2.21}$$

From the Lagrangian (2.21), one is able to find the four-momentum as

$$p_\mu = \frac{\partial \mathcal{L}}{\partial \dot{x}^\mu} = (m + U)\, g_{\mu\nu} u^\nu \,. \tag{2.22}$$

Based on the separable Hamilton-Jacobi action, $S = -Et + L\phi + S_r + S_\theta$, the equation for the magnetized particle can be obtained as

$$g_{tt}\Big[\frac{l^2}{r^2 \sin^2\theta} + 1 - \frac{\mathcal{U}}{m} + g_{rr}\left(1 + \frac{\mathcal{U}}{m}\right)^2 \dot{r}^2\Big] + \mathcal{E}^2 + \\ + g_{tt} g_{\theta\theta}\left(1 + \frac{\mathcal{U}}{m}\right)^2 \dot{\theta}^2 = 0\,. \tag{2.23}$$

For further analysis, we shall restrict ourselves to the equatorial plane (i.e., $\theta = \pi/2$) and then assume that the magnetic dipole of the particles is perpendicular to the equatorial plane, thus allowing us to have the components of the particle's magnetic moment as $\mu^{\hat{\alpha}} = (0, 0, \mu, 0)$ ([115]). That is, the particle's magnetic moment is assumed to be oriented with the magnetic field aligned along the $z$-axis, typically perpendicular to the equatorial plane. This orientation allows the dipole moment to interact with the magnetic field by surviving its $\mu^{\hat{\theta}}$ component, following the energy minimization principle. This choice not only simplifies our calculations but also enhances our qualitative understanding of magnetic interactions under the gravitational field of the self-dual BH in LQG. This, in turn, allows one to have $\mathcal{U} = \frac{\mu F_{r\phi}}{\sqrt{g_{rr} g_{\phi\phi}}}$ for the magnetic interaction. For the magnetized particle motion we then rewrite the Hamilton-Jacobi action at the equatorial plane as

$$S = -Et + L\phi + S_r \,, \tag{2.24}$$

where we denote the total energy and angular momentum of the magnetized particle by $p_t = -E$ and $p_\phi = L$, respectively. Taking all together, the motion of the magnetized particles around the LQG BH takes the following forms

$$\dot{t} = -\frac{\mathcal{E}}{(1 + \frac{\mathcal{U}}{m}) g_{tt}} \,,$$

$$\dot{\phi} = \frac{l}{(1+\frac{\mathcal{U}}{m})g_{\phi\phi}}\,,$$

$$\dot{r}^2 = \frac{1}{-g_{rr}g_{tt}}(\mathcal{E}^2 - V_{eff})\,, \tag{2.25}$$

where $\mathcal{E} = E/m$ and $l = L/m$ refer to the specific energy and angular momentum of particles, respectively. From Eq. (2.25) the effective potential for radial motion can be obtained as

$$V_{eff} = A(r)\left(1 + \frac{l^2}{r^2} - \frac{\mathcal{U}}{m}\right)\,, \tag{2.26}$$

which includes the dimensionless the magnetic interaction/coupling parameter

$$\beta = \frac{\mu B_0}{m}\,, \tag{2.27}$$

which characterizes the magnetic field strength on the particles with a magnetic dipole or simply represents the interaction between external uniform magnetic field and these magnetized particles.

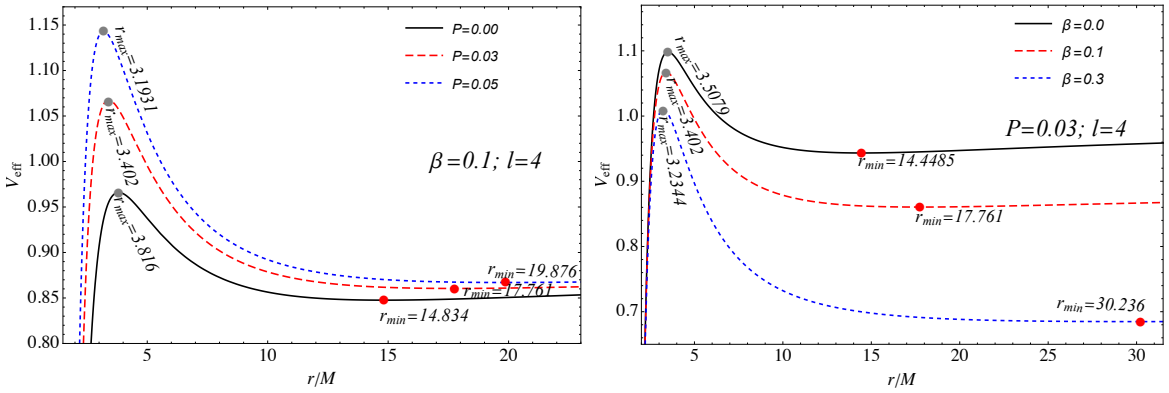


Figure 2.6: Radial profile of the effective potential for the particles with a nonzero magnetic dipole momentum around the self-dual BH in the presence of an external asymptotically uniform magnetic field for different selected combinations of the quantum correction parameter $P$ (left panel) and the magnetic interaction parameter $\beta$ (right panel). One can observe that the minima ($r_{min}$) and the maxima ($r_{max}$) correspond to the stable and unstable circular orbits, respectively.

We then turn to analyze the effective potential for radial motion of the magnetized particles moving around the BH in LQG in the case in which an external

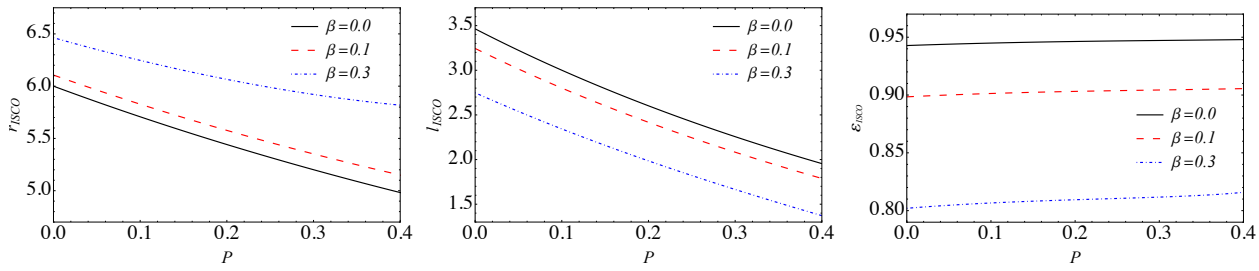


Figure 2.7: The ISCO parameters, $r_{ISCO}$, $l_{ISCO}$, $\mathcal{E}_{ISCO}$ for the magnetized particles are plotted as a function of the quantum correction parameter $P$ for various combinations of the magnetic interaction parameter $\beta$.

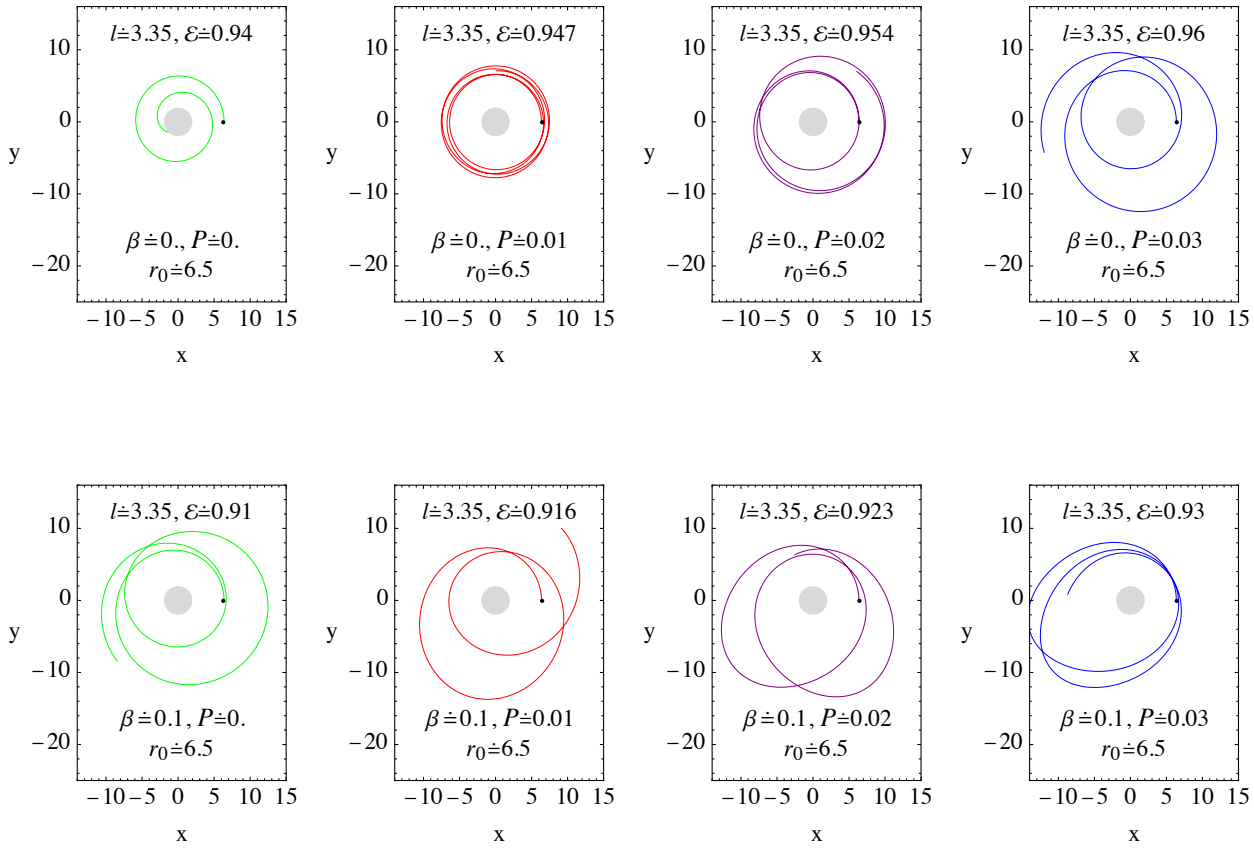


Figure 2.8: The trajectories of the test particle with magnetic dipole moment in the vicinity of the self-dual BH immersed in an external uniform magnetic field for various possible cases. Here, we note that $\beta$ is the magnetic interaction parameter that represents the interaction between an external uniform magnetic field and a particle with a magnetic dipole moment.

magnetic field is present. In Fig. 3.1, we depict the radial dependence of the effective potential $r$. Namely, we show the impact of the quantum correction pa-

rameter $P$ on the behavior of the effective potential for fixed magnetic interaction parameter $\beta$, while the impact of the magnetic interaction parameter for fixed $P$. As can be seen from Fig. 3.1 the effective potential has two extreme points that correspond to stable and unstable circular orbits for particles with magnetic dipole moment in the LQG BH vicinity, i.e., the minimum $r_{min}$ and the maximum $r_{max}$ represent stable and unstable circular orbits. From Fig. 3.1, the shape of the effective potential is shifted upward to its higher values, but the stable orbits are shifted to the right to larger $r$ as the quantum correction parameter $P$ increases. Similar behavior is also observed for unstable orbits. One can then deduce that the gravity in the background spacetime is significantly enhanced as a consequence of the effect of parameter $P$. Similarly, we observe a resembling effect on the behavior of stable and unstable circular orbits under the effect of the magnetic interaction parameter $\beta$, which causes the radius of stable circular orbits to increase. Unlike stable orbits, the radius of unstable circular orbits begins to decrease as the magnetic coupling parameter $\beta$ rises. Additionally, it is important to find circular orbits on which particles with the magnetic dipole moment move around the self-dual BH in LQG immersed in an external uniform magnetic field. To this end, one needs to impose the condition, $\frac{\partial^2 V_{eff}}{\partial r^2} > 0$ that solves to give stable circular orbits. We do however utilize a general condition $\frac{\partial V_{eff}}{\partial r} = \frac{\partial^2 V_{eff}}{\partial r^2} = 0$ to determine and analyze innermost stable circular orbits (ISCOs). In Fig. 2.7, we show the ISCO radius, angular momentum and energy as a function of the quantum correction parameter $P$ for various combinations of the magnetic interaction parameter $\beta$. As can be seen from the left panel of Fig. 2.7, the ISCO radius for the magnetized particles increases with the increasing magnetic interaction parameter, but it decreases under the effect of parameter $P$. Interestingly, it is observed that the effect of $P$ on the ISCO behavior reduces for larger values of the magnetic interaction parameter $\beta$. Furthermore, we also demonstrate other

ISCO parameters, such as the angular momentum and the energy as a function of $P$ for different values of the magnetic coupling parameter $\beta$; see the middle and the right panels of Fig. 2.7. It is obvious that the combined effects of $\beta$ and $P$ can cause the angular momentum of the magnetized particles to decrease at the ISCO. However, the ISCO energy of magnetized particles slightly increases as the parameter $P$ increases, whereas it significantly decreases as a consequence of the magnetic interaction parameter $\beta$, as seen in the right panel of Fig. 2.7.

To gain a deeper understanding about the impact of the magnetic interaction and the quantum correction parameters, we also plot the magnetized particle trajectory restricted from moving on the equatorial plane of the self-dual BH in LQG in the presence of an external magnetic field; see Fig. 2.8. There can exist various orbits, e.g., captured, bound and escape orbits due to different values of parameters, as seen in Fig. 2.8. From the particle trajectory, one can observe that the orbits are the captured when considering the vanishing both parameters, but these orbits turn to be bounded and then be escaping orbits when the quantum correction parameter $P$ increases; see the top row of Fig. 2.8. Interestingly, it is observed that the magnetized particle trajectories slightly become chaotic under the combined effects of $P$ and $\beta$, as shown in the bottom row of Fig. 2.8.

Additionally, to be more informative we explore the ISCO parameters of the magnetized particle numerically and tabulate their values in Table 2.1. Together with the ISCO radii, the specific angular momentum and energy of the magnetized particle moving at the ISCO, we also explore the magnetized particle's linear velocity (the azimuthal velocity) [41, 151]

$$v_\phi = \Omega \sqrt{\frac{g_{\phi\phi}}{g_{tt}}}, \tag{2.28}$$

with the Keplerian angular velocity/frequency, as tabulated in Table 2.1, which

is written by

$$\Omega = \sqrt{-\frac{\partial_r g_{tt}}{\partial_r g_{\phi\phi}}}\,. \tag{2.29}$$

The behavior of Figs. 2.7 and 2.8 is also reflected in Table 2.1. As can be seen from

| $P$ | $\beta$ | $r_{ISCO}$ | $l_{ISCO}$ | $\mathcal{E}_{ISCO}$ | $v_{ISCO}$ | $\Omega_{ISCO}$ |
|---|---|---|---|---|---|---|
| 0.00 | 0.0 | 6 | $2\sqrt{3}$ | $\frac{2\sqrt{2}}{3}$ | 1/2 | $\frac{1}{6\sqrt{6}}$ |
| 0.01 | 0.0 | 5.88230 | 3.36591 | 0.94385 | 0.49665 | 0.06916 |
| 0.02 | 0.0 | 5.76906 | 3.27137 | 0.94491 | 0.49326 | 0.07027 |
| 0.05 | 0.0 | 5.45429 | 3.00811 | 0.94807 | 0.48293 | 0.07350 |
| 0.10 | 0.0 | 5.00308 | 2.62888 | 0.95335 | 0.46514 | 0.07846 |
| 0.20 | 0.0 | 4.31952 | 2.04469 | 0.96365 | 0.42784 | 0.08627 |
| | | | | | | |
| 0.00 | 0.1 | 6.10610 | 3.24455 | 0.89843 | 0.49349 | 0.06627 |
| 0.01 | 0.1 | 5.99407 | 3.15118 | 0.89959 | 0.48969 | 0.06723 |
| 0.02 | 0.1 | 5.88649 | 3.06118 | 0.90074 | 0.48584 | 0.06816 |
| 0.05 | 0.1 | 5.58893 | 2.81000 | 0.90409 | 0.47404 | 0.07080 |
| 0.10 | 0.1 | 5.16910 | 2.44653 | 0.90939 | 0.45349 | 0.07455 |
| 0.20 | 0.1 | 4.57350 | 1.88065 | 0.91868 | 0.40859 | 0.07859 |

Table 2.1: Numerical values of the ISCO parameters, $r_{ISCO}$, $l_{ISCO}$, $\mathcal{E}_{ISCO}$, $v_{ISCO}$ and $\Omega_{ISCO}$ of the magnetized particles orbiting on the ISCO orbits around the self-dual BH in the presence of an external magnetic field.

Table 2.1, the particle's linear velocity at the ISCO decreases with the increasing quantum correction parameter $P$ and magnetic interaction parameter $\beta$, whereas the Keplerian angular velocity increases with an increasing $P$, but it decreases as a consequence of an increase in $\beta$.

We examined unique effects of the quantum correction parameter on the dynamics of particles with magnetic dipole moment and their non-geodesics around a self-dual BH immersed in an external uniform magnetic field in LQG. We then focus on the dynamics of electrically charged particles around the BH considered here. This is what we intend to take up in the next section.

## 2.5 The motion of the charged particles near a self-dual black hole immersed in an external magnetic field in Loop Quantum Gravity

Here, we investigate the dynamics of electrically charged particles around a self-dual BH immersed in an external uniform magnetic field in LQG. For that, we begin to write the Hamilton-Jacobi equation for electrically charged particle with the rest mass $m$ and charge $q$ as follows:

$$g^{\mu\nu}\left(\frac{\partial S}{\partial x^{\mu}}+qA_{\mu}\right)\left(\frac{\partial S}{\partial x^{\nu}}+qA_{\nu}\right)=-m^{2}, \tag{2.30}$$

where the four potential of electromagnetic field $A_{\alpha}$ is give in Eq. (2.16). The Lagrangian of the system for an electrically charged particle is then given by

$$\mathcal{L}=\frac{1}{2}mg_{\mu\nu}u^{\mu}u^{\nu}+qu^{\mu}A_{\mu}\,, \tag{2.31}$$

which allows to write the four-momentum as

$$p_{\mu}=mg_{\mu\nu}u^{\nu}+qA_{\mu}\,. \tag{2.32}$$

Following to the Hamilton-Jacobi action, $S=-Et+L\phi+S_{r}+S_{\theta}$, the equation of motion for a charged particle at the equatorial plane (i.e., $\theta=\pi/2$) is defined by

$$g_{tt}\Big[1+g_{rr}\dot{r}^{2}+\left(\frac{l}{r\sin\theta}+\frac{qA_{\phi}}{mr\sin\theta}\right)^{2}\Big]+\mathcal{E}^{2}=0\,, \tag{2.33}$$

where we have defined $\mathcal{E}=\frac{E}{m}$ and $l=\frac{L}{m}$ as the specific energy and angular momentum of the electrically charged particle per unit mass. Here, we note that for the further analysis we shall for simplicity restrict the motion of an electrically charged particle to the equatorial plane, $\theta=\frac{\pi}{2}$. Taking all into consideration the equation of the radial motion of charged particles moving around of the self-dual BH is written as

$$\dot{r}^2 = \frac{1}{-g_{rr}g_{tt}}\Big(\mathcal{E}^2 - V_{eff}\Big)\,. \tag{2.34}$$

From the radial equation of motion, the effective potential, $V_{eff}$, reads as

$$V_{eff} = A(r)\left[1 + \left(\frac{l}{r} + \frac{qA_\phi}{mr}\right)^2\right]\,. \tag{2.35}$$

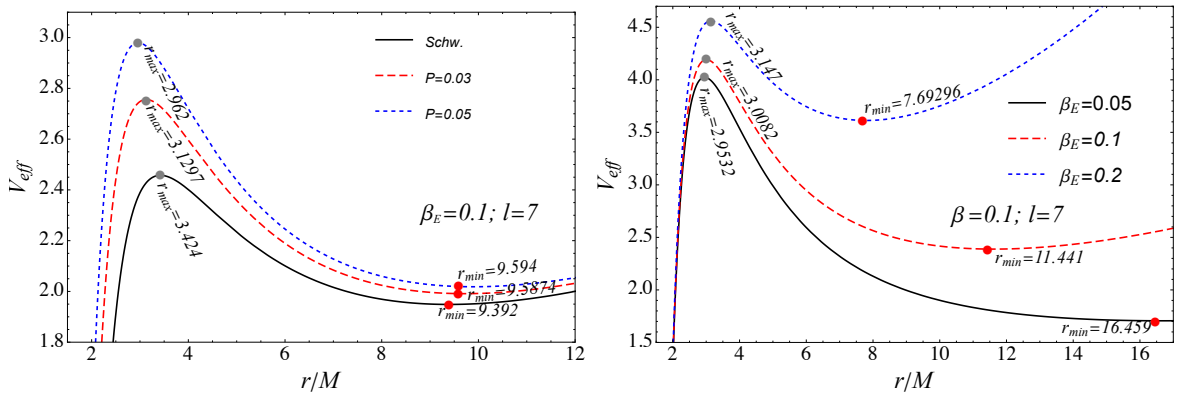


Figure 2.9: Radial profile of the effective potential for the electrically charged particles around the self-dual BH in the presence of an external uniform magnetic field for various combinations of the quantum correction parameter $P$ (left panel) and the magnetic parameter $\beta_E$ (right panel). We note that the minima ($r_{min}$) and the maxima ($r_{max}$) correspond to the stable and unstable circular orbits, respectively.

To gain a deeper understanding of the non-geodesic motion of an electrically charged particle around the BH we shall further examine the effective potential for radial motion. In Fig. 2.9, we show the radial profile of the effective potential for the charged particle for various possible cases. The left panel of Fig. 2.9 reflects the impact of the quantum correction parameter $P$ on the radial profile of the effective potential while keeping the magnetic interaction parameter $\beta$ fixed, while the right panel reflects the impact of $\beta_E$ for the fixed $P$. It is worth noting that the magnetic field can drastically influence the motion of a charged particle, causing its geodesics to alter around a BH. Here, it is valuable to note that the magnetic field parameter plays a crucial role in comparing the relative strength

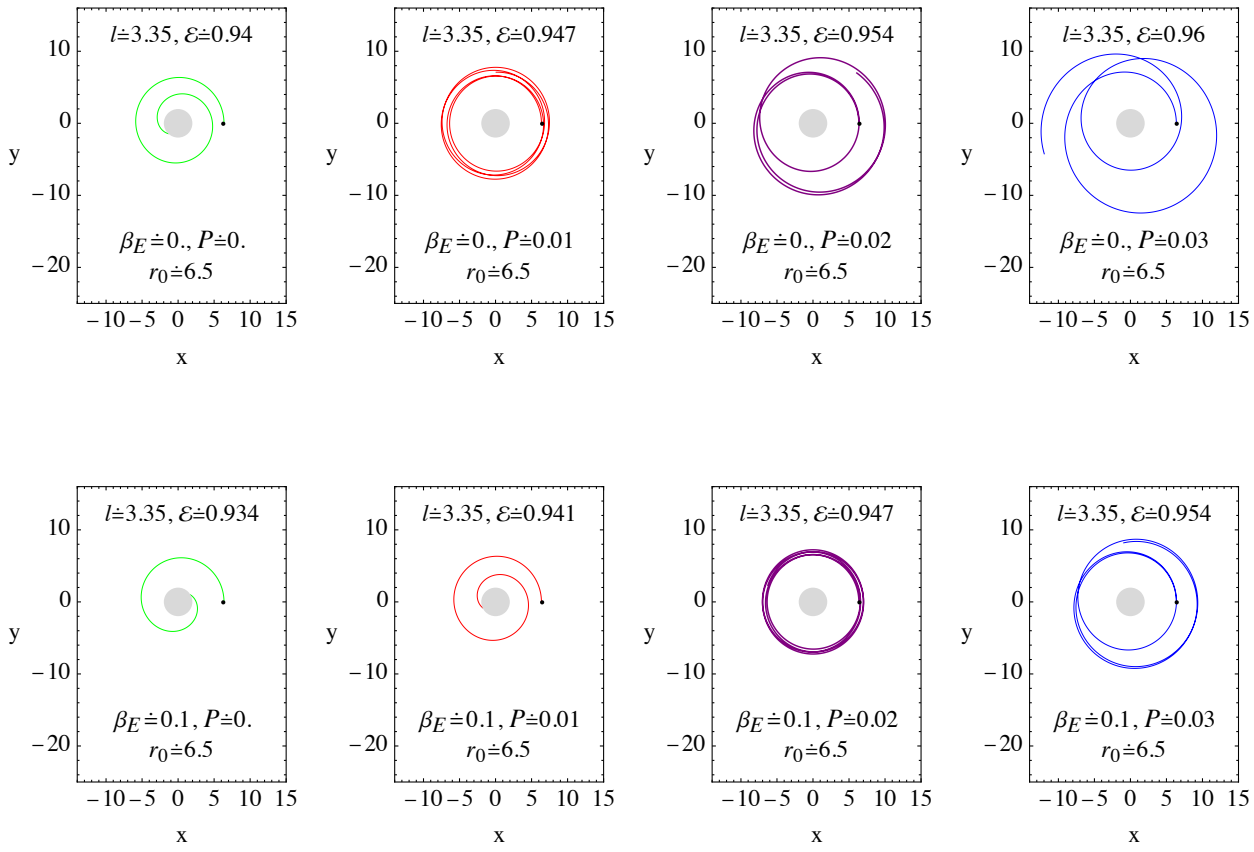


Figure 2.10: The trajectories of the electrically charged test particles in the vicinity of the self-dual BH immersed in an external uniform magnetic field for various possible cases. Here, we note that $\beta_E$ is the magnetic parameter that represents the interaction between an external uniform magnetic field and an electrically charged particle.

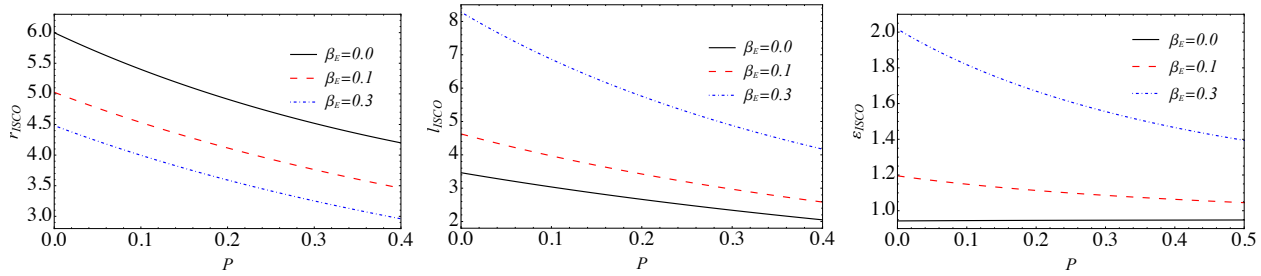


Figure 2.11: The ISCO parameters, $r_{ISCO}$, $l_{ISCO}$, $\mathcal{E}_{ISCO}$ for electrically charged particles are plotted as a function of the quantum correction parameter $P$ for various combinations of the magnetic parameter $\beta_E$.

of the magnetic and gravitational fields acting on a charged particle's motion around the BH. Unlike, in a flat spacetime where the contribution of gravity no

longer exists, a test particle with an electric charge $q$ and rest mass $m$ can have a characteristic cyclotron frequency in a magnetic field with strength $B$

$$\Omega_c = \frac{|qB|}{m}\,, \tag{2.36}$$

which serves as the magnetic field parameter. However, in a curved spacetime, together with gravity, a charged particle can, in addition to the characteristic cyclotron frequency, have the Keplerian frequency when orbiting around a BH with mass $M$, i.e.,

$$\Omega = \frac{r_g^{1/2}}{\sqrt{2}\, r^{3/2}}\,. \tag{2.37}$$

where $r_g$ is the BH gravitational radius $r_g$. The impact on the particle motion moving around a BH (i.e., $r \sim r_g$) is interpreted by the dimensionless parameter, usually referred to as the magnetic field parameter $\beta_E$, which relates to the strength of the magnetic field (see, for example, [146])

$$\beta_E \equiv \frac{\Omega_c}{\Omega} \equiv \frac{qB_0M}{m}\,, \tag{2.38}$$

where $B_0$ refers to the strength of the uniform external magnetic field surrounding the BH. To be quantitative we estimate $\beta_E$ as a dimensionless quantity. For example, for a proton $\beta_E$ can take values on the order of $\sim 10^7$ around a BH of mass $M \sim 10M_\odot$ and of $\sim 10^{11}$ around a BH of mass $M \sim 10^9 M_\odot$ with the mass of the Sun, $M_\odot$. However, one can find that $\beta_E$ takes even larger values for an electron, showing that the magnetic field can drastically affect a charged particle motion due to the Lorentz force dominating over the gravitational field in the close vicinity of a BH [146, 119, 40]. As shown in Fig. 2.9, the curves of the effective potential shift upward toward larger values with increasing parameters $P$ and $\beta_E$, causing the strength of the gravitational potential to decrease. It is also observed from Fig. 2.9 that an increase in the quantum correction parameter $P$ shifts stable circular orbits to larger $r$, while they become closer to the central object under the influence of the magnetic parameter $\beta_E$, resulting in the radius

of stable circular orbits decreasing. Additionally, we demonstrate the trajectory of electrically charged particles restricted from moving on the equatorial plane of the self-dual black hole in LQG for various possible cases; see Fig. 2.10. Here, we analyze the effects of both $P$ and $\beta_E$ on the behavior of captured, bound, and escape orbits around the black hole. In Fig. 2.10, the top row shows the impact of parameter $P$ on the trajectory of electrically charged particles, while the bottom row shows the change in the behavior of particle trajectories when considering the magnetic parameter $\beta_E$. It is observed from the particle trajectory that orbits are captured when considering the vanishing of both parameters, but these orbits become bounded and escaping orbits when increasing the parameter $P$; as seen in the top row of Fig. 2.10. The interesting point to note here is that the role of the magnetic parameter can make bounded orbits turn into captured orbits, causing the electrically charged particle to fall into the black hole; see the bottom row of Fig. 2.10. Interestingly, one can observe that the lose of the electrically charged particle's energy, $\mathcal{E}$, decreases with an increasing quantum correction parameter $P$. This suggests that the effect of $P$ allows the particles to retain their energy when orbiting around the black hole, preventing them from falling into the black hole, as shown in the third panels of both the top and bottom rows of Fig. 2.10.

Similar to what is observed to the previous section, here, we also turn to examine the ISCO parameters of the electrically charged particle moving around the self-dual black hole immersed in an external magnetic field in LQG. The following conditions, required for the particles to be on the ISCO,

$$V_{eff}(r) = \mathcal{E}^2_{ISCO} \text{ and } \frac{\partial V_{eff}(r)}{\partial r} = \frac{\partial^2 V_{eff}(r)}{\partial r^2} = 0\,. \tag{2.39}$$

solve to give the ISCO parameters. In Fig. 2.11, we show the ISCO parameters, such as the ISCO radii, the energy and the angular momentum of the electrically charged particles. As shown in Fig. 2.11, the ISCO parameters decrease with an increasing parameter $P$, similar to what is observed in previous section. However,

these parameters are influenced significantly by the magnetic parameter $\beta_E$. Interestingly, unlike the magnetic interaction parameter $\beta$ between magnetic field and particle's magnetic dipole momentum, an increase in the magnetic parameter $\beta_E$ decreases the ISCO radii but increases the angular momentum and the energy of the electrically charged particle, as seen in Fig. 2.11. Furthermore, together

| $P$ | $\beta_E$ | $r_{ISCO}$ | $l_{ISCO}$ | $\mathcal{E}_{ISCO}$ | $v_{ISCO}$ | $\Omega_{ISCO}$ |
|---|---|---|---|---|---|---|
| 0.00 | 0.1 | 5.02571 | 4.62678 | 1.19536 | 0.57489 | 0.08875 |
| 0.01 | 0.1 | 4.93044 | 4.46667 | 1.18750 | 0.57108 | 0.09025 |
| 0.02 | 0.1 | 4.83816 | 4.31457 | 1.18017 | 0.56730 | 0.09174 |
| 0.05 | 0.1 | 4.57811 | 3.90153 | 1.16099 | 0.55607 | 0.09620 |
| 0.10 | 0.1 | 4.19459 | 3.33319 | 1.13652 | 0.53779 | 0.10353 |
| 0.20 | 0.1 | 3.57576 | 2.51660 | 1.10660 | 0.50334 | 0.11771 |
| | | | | | | |
| 0.00 | 0.2 | 4.63195 | 6.32663 | 1.57136 | 0.61639 | 0.10031 |
| 0.01 | 0.2 | 4.53872 | 6.07161 | 1.54979 | 0.61315 | 0.10225 |
| 0.02 | 0.2 | 4.44858 | 5.83139 | 1.52955 | 0.60991 | 0.10420 |
| 0.05 | 0.2 | 4.19539 | 5.18963 | 1.47584 | 0.60022 | 0.11005 |
| 0.10 | 0.2 | 3.82382 | 4.33350 | 1.40524 | 0.58431 | 0.11985 |
| 0.20 | 0.2 | 3.22674 | 3.16359 | 1.31271 | 0.55439 | 0.13961 |

Table 2.2: Numerical values of the ISCO parameters, $r_{ISCO}$, $l_{ISCO}$, $\mathcal{E}_{ISCO}$, $v_{ISCO}$ and $\Omega_{ISCO}$ of the electrically charged particles orbiting on the ISCO orbits around the self-dual BH in the presence of an external magnetic field in LQG, similar to what is observed in Table 2.1 for the magnetized particles.

with $r_{ISCO}$, $l_{ISCO}$, and $\mathcal{E}_{ISCO}$ of electrically charge particles orbiting at the ISCO, we examine the charged particle's linear (orbital) velocity

$$v_\phi = \Omega \sqrt{\frac{g_{\phi\phi}}{g_{tt}}}, \tag{2.40}$$

with the Keplerian angular velocity/frequency, $\Omega$, which can be defined using non-geodesic equation for charged particles [152]:

$$g_{tt,r} + \Omega^2 g_{\phi\phi,r} = -\frac{2q}{m}\left(A_{t,r} + \Omega A_{\phi,r}\right)\left(-g_{tt} - \Omega^2 g_{\phi\phi}\right), \tag{2.41}$$

then expression for $\Omega$:

$$\begin{aligned}\Omega^2 &= \left[\Omega_0^2 - 2g_{tt}\left(\frac{qA_{\phi,r}}{mg_{\phi\phi,r}}\right)^2 \pm \frac{2qA_{\phi,r}}{mg_{\phi\phi,r}} \times\right. \\ &\times \left.\left\{-\Omega_0^2 g_{tt} - \Omega_0^4 g_{\phi\phi} + \left(\frac{qA_{\phi,r}\, g_{tt}}{mg_{\phi\phi,r}}\right)^2\right\}^{1/2}\right] \times \\ &\times \left[1 + 4g_{\phi\phi}\left(\frac{qA_{\phi,r}}{mg_{\phi\phi,r}}\right)^2\right]^{-1}, \end{aligned} \tag{2.42}$$

which, in the limit of $q \to 0$, reduces to

$$\Omega_0 = \sqrt{-\frac{\partial_r g_{tt}}{\partial_r g_{\phi\phi}}}\,. \tag{2.43}$$

All numerical estimations for the ISCO parameters together with $v_{ISCO}$, $\Omega_{ISCO}$ are also reflected in Table 2.2 for the electrically charged particles orbiting on ISCO around the self-dual black hole in LQG in the presence of an external magnetic field. As shown in Table 2.1, the electrically charged particle's linear velocity at the ISCO decreases with the rise in the quantum correction parameter $P$, but it increases under the effect of the magnetic field parameter $\beta_E$, while the Keplerian angular velocity increases with increasing $P$ and $\beta_E$.

## 2.6 Conclusion

In this chapter, we considered a self-dual BH immersed in an external asymptotically uniform magnetic field in LQG. To have information about spacetime geometry and test its nature one needs to delve into the effects of a quantum correction parameter and electromagnetic interactions on the particle geodesics. To this end, we studied the motion of magnetic dipoles and electrically charged particles in the environment surrounding the spacetime geometry in LQG. We derived the field equations and determined the electromagnetic four-vector potential for the case of the self-dual BH in LQG.

We began to study the influence of the DM halo on the ISCO parameters, specifically, the energy $\mathcal{E}_{ISCO}$, angular momentum $l_{ISCO}$ and the ISCO radius $r_{ISCO}$ for timelike particles orbiting the Schwarzschild-like BH surrounded by a Dehnen-type DM halo. Our analysis showed that increasing the DM density $\rho_s$ results in a corresponding increase in both $r_{ISCO}$ and $l_{ISCO}$. Interestingly, the characteristic scale $r_s$ has a nonmonotonic effect on $l_{ISCO}$, i.e, while $r_{ISCO}$ increases with $r_s$, the angular momentum $l_{ISCO}$ initially decreases up to a critical value of $r_s$, beyond which it begins to increase again, as shown in Fig. 2.3. Finally, we investigated the Lyapunov exponent to understand the stability of timelike particle orbits in the BH vicinity. The radial profile of the Lyapunov exponent, presented in Fig. 2.4, clearly shows a slight rightward shift in the curves with increasing $\rho_s$ and $r_s$, suggesting that the corresponding stable circular orbits are displaced to larger radial distances. This behavior is consistent with the change in ISCO radii observed in Fig.2.3.

We also examined the motion of magnetized particles around the BH in the presence of an external magnetic field. We studied the stable and unstable circular orbits for particles with a magnetic dipole moment and showed that the stable orbits are shifted to exist at larger $r$ under the influence of the quantum correction parameter $P$. We also showed that similar behavior is also observed for unstable orbits. It was found that the gravity in the spacetime of the self-dual BH in LQG is significantly enhanced by the impact of parameter $P$. Similarly, we also observed a similar behavior of stable and unstable circular orbits under the influence of the magnetic interaction parameter $\beta$. We also showed that stable orbits of electrically charged particles become closer to the BH under the influence of the magnetic parameter $\beta_E$, causing the radius of these orbits to decrease.

We also studied the combined effects of the quantum correction parameter $P$ and the magnetic interaction parameter $\beta$ on the ISCO radius. We showed that

the ISCO radius for magnetized particles decreases under the influence of the quantum correction parameter but it increases with an increasing magnetic interaction parameter $\beta$. However, unlike the magnetic interaction parameter $\beta$, the ISCO radius of electrically charged particles decreases with an increasing magnetic parameter $\beta_E$ decreases. Notably, we showed that the ISCO radius of magnetized particles is greater than that of electrically charged particles due to the magnetic field interaction. Further, we examined the ISCO parameters, such as the angular momentum $l_{ISCO}$ and the energy $\mathcal{E}_{ISCO}$, and showed that the angular momentum of the magnetized particles orbiting on the ISCO decreases under the effects of both the magnetic coupling parameter $\beta$ and the quantum correction parameter. Interestingly, we observed that the ISCO energy of magnetized particles increases due to the impact of $P$, while it decreases as a consequence of the influence of $\beta$. Unlike the magnetic interaction parameter $\beta$, the angular momentum and the energy of the electrically charged particles increase with a rise in the value of the magnetic parameter $\beta_E$.

We also showed that the particle's linear velocity $v_{ISCO}$ decreases, but the Keplerian angular velocity $\Omega_{ISCO}$ increases as a consequence of the influence of the quantum correction parameter $P$. However, when the effect of the magnetic interaction parameter $\beta$ is included, $v_{ISCO}$ and $\Omega_{ISCO}$ for the magnetized particles decrease with a rise in the value of $\beta$, whereas these parameters increase with an increasing magnetic field parameter $\beta_E$ for the electrically charged particles orbiting on the ISCO around the self-dual BH immersed in an external uniform magnetic field in LQG.

Furthermore, we analyzed captured, bound and escape orbits of magnetized and electrically charged particles restricted from moving on the equatorial plane of the self-dual BH in LQG for various possible cases. We showed that the orbits of the magnetized particles are captured when considering the vanishing of the

quantum correction parameter $P$ and the magnetic interaction parameter $\beta$, but they turn to be bounded and then become escaping orbits as a consequence of an increasing quantum correction parameter $P$. Interestingly, it turns out that the magnetized particle trajectories slightly become chaotic under the combined effects of $P$ and $\beta$. However, from the trajectories of electrically charged particles we showed that the role of the magnetic parameter $\beta_E$ can make bounded orbits turn into captured orbits, causing the electrically charged particle to fall into the BH. Unlike the magnetized particle case, we observed that the loss of the electrically charged particle's energy (i.e., $\mathcal{E}$) decreases with an increasing quantum correction parameter $P$, causing the particles to retain their energy when orbiting around the BH and preventing them from falling into the BH. This is a remarkable and distinguishing feature of orbits of electrically charged particles compared to the magnetized particles around the self-dual BH in LQG. We also investigated the timelike geodesics of particles in the BH-DM spacetime, highlighting how the novel Dehnen-type DM halo influences the gravitational dynamics and affects particle trajectories. We analyzed the trajectory of timelike particles with the appropriate specific energy $\mathcal{E}$ and angular momentum $l = \frac{L}{m}$. We showed that there exist two types of orbits: captured and bound orbits. Our analysis indicated that these orbits become captured with increasing $\rho_s$ and $r_s$, as represented in Fig. 2.1. Using the Lagrangian formalism, we derived the effective potential and analyzed its radial behavior for timelike particle motion. The effective potential exhibits two extrema, corresponding to stable and unstable circular orbits. Our results showed that increasing the DM halo's density $\rho_s$ and characteristic scale $r_s$ leads to an outward shift of both stable and unstable circular orbits, effectively expanding the influence region of the BH–DM system. The effective potential curves exhibit a slight shift to the right, indicating larger orbital radii, while the maximum effective potential decreases with an increase in $\rho_s$ and $r_s$, as illustrated

in Fig. 2.2.

# Chapter III

# Orbits of particles with magnetic dipole moment around magnetized Schwarzschild black holes: Applications to S2 star orbit

## 3.1 Introduction

The investigation of free-falling objects in gravitational fields links geometry and gravity through the GR, where the curvature of spacetime plays the principal role. This fundamental understanding gained popularity early once it was recognized that planets and light follow geodesics. Outstanding discoveries, right after the proposition of the Schwarzschild solution [153], was the verification of light deflection during the 1919 solar eclipse expedition [154]. The precise evaluation of the anomalous precession in the perihelion of Mercury [155], which constitute the primary standard tests of general relativity. However, the complex nature of the partial differential equations governing particle dynamics in curved spacetimes necessitates simplified or numerical solutions to compare theoretical results with observational tests.

Analytical expressions have several advantages since they serve as benchmarks for numerical methods, and hence, they facilitate comprehensive parameter space exploration for predicting astrophysical observables. Efforts to find exact analyt-

ical solutions for geodesic equations of particles have intensified since Hagihara's studies in 1931 [156], followed by works by Darwin, Mielnik, and Plebański [157, 158, 159]. These methods, which are based on the theories of elliptic functions and modular forms, were studied by nominated nineteenth-century mathematicians such as Jacobi [160], Abel [161], Riemann [162, 163], and Weierstrass [164] (see also Ref. [165] for a complete textbook review on these discoveries). Particularly noteworthy is the application of modular forms in solving (hyper-)elliptic integrals involved in particle trajectory studies, garnering significant attention in recent decades. These methods, rooted in the theories of elliptic functions and modular forms, have been the focus of numerous investigations analyzing trajectory curves in BH spacetimes inferred from general relativity and its extensions (see, for example, Refs. [166, 167, 168, 169, 170, 171, 172, 173, 174, 175, 176, 177, 178, 179, 180, 181, 182, 183, 184, 185, 186, 187, 188, 189, 190, 191, 192, 193, 194, 195, 196]).

Building upon this scientific foundation, contemporary research continues to explore the properties and dynamics of particles falling in gravitational fields in diverse astrophysical contexts bound and unbound particle orbits, in particular, represent fundamental aspects of motion that offer valuable insights into the structure and evolution of the universe. Bound orbits, characterized by closed trajectories around central masses, are found extensively in celestial systems, ranging from planetary orbits in the solar system to the motion of stars in galaxies [197, 198]. These orbits contribute to astrophysical objects' stability and long-term dynamics and provide essential constraints on theoretical models of gravitational dynamics and cosmological evolution.

On the other hand, unbound particle orbits extend indefinitely through space, either escaping to infinity (deflecting trajectories) or falling into gravitational singularities (plunge or captured orbits). These orbits play a critical role in understanding cosmic phenomena such as the formation and evolution of galaxies

and the dynamics of stellar populations within galactic clusters (see, for example, Ref. [199] and the book [200]). They are also useful for modeling particle orbits within DM halos [201]. Unbound orbits provide valuable information about the escape velocity of celestial bodies, shedding light on the mechanisms underlying stellar ejection and galactic interactions. Moreover, the study of unbound orbits offers insights into the gravitational interactions between celestial objects and their surrounding environments, contributing to our understanding of the large-scale structure and evolution of the universe [200].

The study of trajectories of magnetized particles around magnetized astrophysical objects, particularly BH, is of great importance in understanding the nature of astrophysical phenomena. Magnetized BHs, characterized by intense magnetic fields generated by rapidly rotating neutron stars or stellar-mass BHs, exhibit intricate interactions between gravitational and electromagnetic forces that give rise to a diverse range of astrophysical phenomena [202, 203, 204, 205, 206, 207, 208, 131]. Charged particles, such as electrons and protons, spiraling along magnetic field lines near these objects undergo complex dynamics, including acceleration, deflection, and emission of radiation. These processes play a crucial role in shaping the observational properties of various astrophysical sources, including pulsars, gamma-ray bursts, and active galactic nuclei [209, 210, 211]. By studying the trajectories of magnetized particles, researchers can gain insights into the mechanisms driving particle acceleration, the formation of relativistic jets, and the emission of high-energy radiation observed across the electromagnetic spectrum. Furthermore, understanding the interplay between gravitational and electromagnetic forces near magnetized astrophysical objects offers valuable insights into fundamental aspects of plasma physics, high-energy astrophysics, and GR [212, 213, 214].

Given the importance of this subject, our study aims to investigate the dy-

namics of magnetized particles affected by the magnetic field of an astrophysical object, in this case, a magnetized Schwarzschild BH. In this study, we analyze the dynamics and motion of particles possessing magnetic dipole moments analytically as they move in the exterior geometry of a Schwarzschild BH with an associated magnetic field. We utilize elliptic integrals to express exact analytical solutions to the equations of motion governing the behavior of these particles. Particularly, the deflecting trajectories are considered akin to a type of gravitational Rutherford scattering, which is also treated analytically.

To accomplish our objective, we structure this chapter as follows: In Section 3.2, we introduce the spacetime under study and develop a Lagrangian formalism, leading to the equations of motion for the test particles. In Section 3.3, we initiate our main study by providing a general classification of the possible orbits based on the radial profile of the effective potential experienced by the particles. In this section, we provide a precise derivation of the planetary orbits with different eccentricities, also assessed by observational tests regarding the S-star orbits at the center of the Milky Way. In Section 3.4, we continue our study by investigating the unbound orbits, consisting of deflecting trajectories. These trajectories are either deflected beyond the BH or inexorably fall into the event horizon. The former is termed gravitational Rutherford scattering in Refs. [182, 188]. To complete this investigation, in Section 3.5, we present a fully analytical study of the purely radial trajectories. We conclude in Section 3.6.

## 3.2 Motion of magnetized particles around a Schwarzschild black hole immersed in magnetic fields

In this section, we derive the equations of motion governing magnetized test particles orbiting a Schwarzschild BH in the presence of an externally applied asymptotically uniform magnetic field. The line element describing the exterior

spacetime of a Schwarzschild BH with mass $M$ is given by

$$ds^2 = -f(r)dt^2 + f(r)^{-1}dr^2 + r^2 d\Omega^2, \tag{3.1}$$

in the usual Schwarzschild coordinates $x^\alpha = (t, r, \theta, \phi)$, with $d\Omega^2 = d\theta^2 + \sin^2\theta d\phi^2$, where the lapse function is given by

$$f(r) = 1 - \frac{2M}{r}. \tag{3.2}$$

### 3.2.1 Magnetization of Schwarzschild-like black holes

Here, we assume that the BH is surrounded by an external, asymptotically uniform magnetic field with a constant value of $B$ at infinity. According to Wald's approach, the four-potential, being solutions of Maxwell's equations, can be expressed as $A^\mu = \frac{B}{2}\xi^\mu_\phi$ [215], where $\xi^\mu_\phi = (0, 0, 0, 1)$ represents a space-like Killing vector. Consequently, we can immediately obtain the non-vanishing components of the electromagnetic tensor as

$$F_{r\phi} = Br\sin^2\theta, \tag{3.3a}$$

$$F_{\theta\phi} = \frac{B}{2}r^2\sin 2\theta. \tag{3.3b}$$

The components of the magnetic field around the BH, as measured by zero angular momentum observers (ZAMOs), can be calculated as

$$B^i = \frac{1}{2}\eta^{i\beta\sigma\mu}F_{\beta\sigma}w_\mu, \tag{3.4}$$

where $i = (r, \theta, \phi)$, $\boldsymbol{w}$ represents the four-velocity of the ZAMOs with $w^\mu = 1/\sqrt{f(r)}(1, 0, 0, 0)$, and $\eta_{\alpha\beta\sigma\gamma}$ denotes the pseudo-tensorial form of the Levi-Civita symbol $\epsilon_{\alpha\beta\sigma\gamma}$ with the following relations:

$$\eta_{\alpha\beta\sigma\gamma} = \sqrt{-g}\,\epsilon_{\alpha\beta\sigma\gamma}, \quad \eta^{\alpha\beta\sigma\gamma} = -\frac{1}{\sqrt{-g}}\epsilon^{\alpha\beta\sigma\gamma}, \tag{3.5}$$

where $g = \det|g_{\mu\nu}| = -r^4\sin^2\theta$, corresponding to the spacetime metric (3.1). Hence, one can obtain expressions for the non-zero orthonormal components of

the magnetic field using the tetrads carried by the ZAMOs [216]. Furthermore, the non-zero orthonormal components of the magnetic field measured by the ZAMOs are calculated as

$$B^{\hat{\theta}} = \sqrt{f(r)}\, B \sin\theta, \tag{3.6a}$$

$$B^{\hat{r}} = B\cos\theta. \tag{3.6b}$$

### 3.2.2 Magnetized particle dynamics

The dynamics of polarized particles within the spacetime described by the line element (3.1) can be expressed using the Lagrangian [217]

$$\mathscr{L} = \frac{1}{2}(m+U)g_{\mu\nu}u^{\mu}u^{\nu} - \frac{1}{2}\kappa U, \tag{3.7}$$

where $\kappa = 1$ and the magnetic interaction term is represented by $U = D^{\mu\nu}F_{\mu\nu}$. The calculation of the magnetic interaction term has been undertaken by various authors (see, for example, Ref. [218]). Specifically, it is given by $U = \mu_{\hat{\alpha}}B^{\hat{\alpha}}$. Furthermore, suppose we limit the motion of the magnetized particles to the equatorial plane and assume that the magnetic dipole of the particles is perpendicular to this plane. In that case, we can express the components of the magnetic moment four-vectors as $\mu^{\hat{\alpha}} = (0, 0, \mu, 0)$. Consequently, we can derive the conjugate momenta as

$$p_{\mu} = \frac{\partial\mathscr{L}}{\partial\dot{x}^{\mu}} = (m+U)g_{\mu\nu}u^{\nu}, \tag{3.8}$$

based on which, the two constants of motion

$$-\mathcal{E} = \big[1+\beta\mathcal{F}(r,\theta)\big]g_{tt}\dot{t}, \tag{3.9}$$

$$l = \big[1+\beta\mathcal{F}(r,\theta)\big]g_{\phi\phi}\dot{\phi}, \tag{3.10}$$

can be defined in accordance with the symmetries of the spacetime, where $\beta = \mu B/m$, and $\mathcal{F}(r,\theta) = \sqrt{f(r)}\sin\theta$. Here, $\mathcal{E} = E/m$ and $l = L/m$ represent the

magnetized particle's specific energy and specific angular momentum, respectively. Furthermore, one can express the Hamilton-Jacobi equation while accounting for the magnetic field as follows:

$$g^{\mu\nu}\frac{\partial \mathcal{S}}{\partial x^{\mu}}\frac{\partial \mathcal{S}}{\partial x^{\nu}} = -m^2\left(1-\frac{U}{m}\right)^2. \tag{3.11}$$

with $\mathcal{S}$ denoting the Jacobi action, and motion restricted to the equatorial plane, the action can be expressed as $\mathcal{S} = -Et + L\phi + \mathcal{S}_r(r)$, and in this context, we have $m = 1$. Therefore, the radial motion can be easily described in terms of the following equation:

$$\dot{r}^2 = \mathcal{E}^2 - V_{\text{eff}}, \tag{3.12}$$

in which

$$V_{\text{eff}}(r;l) = f(r)\left(\left[1-\beta\mathcal{F}(r,\pi/2)\right]^2 + \frac{l^2}{r^2}\right). \tag{3.13}$$

is the effective potential felt by the test particles. In Fig. 3.1, we illustrate how the radial dependence of the effective potential varies with the specific angular momentum (left panel) and the magnetic interaction parameter $\beta$ (middle panel). The maximum of the effective potential denotes instability. Furthermore, these plots indicate that increasing the specific angular momentum $l$ of the magnetized particles and the magnetic interaction parameter $\beta$ leads to an increase in the stable circular orbits (at $r_{\text{min}}$) of the test particles with magnetic dipole momentum. Conversely, an increase in the specific angular momentum of the magnetized particle results in a decrease in the unstable circular orbits (at $r_{\text{max}}$) of the particles with magnetic dipole moment. Moreover, escalating the magnetic coupling parameter $\beta$ leads to an increase in the unstable circular orbits of the magnetized particles. Additionally, Fig. 3.1 presents the radial profile of the effective potential with the specific angular momentum $l_{\text{ISCO}}$ of the magnetized particles in the Innermost Stable Circular Orbit (ISCO) for a given value of $\beta = 0.1$. Consequently,

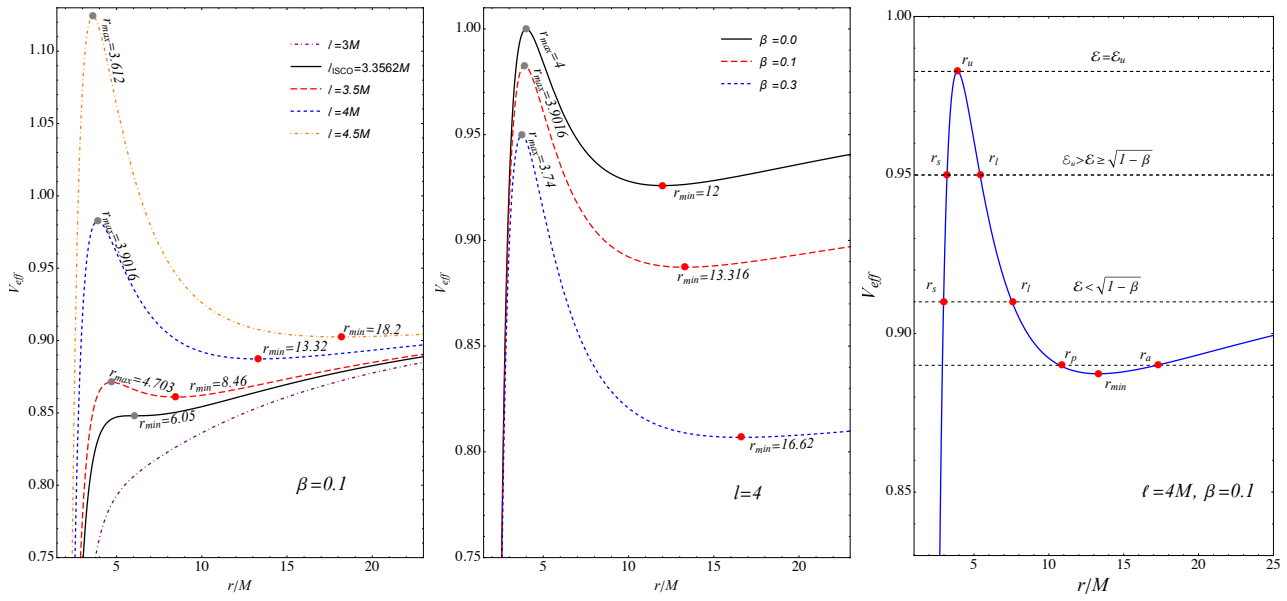


Figure 3.1: The radial profile of the effective potential is depicted for fixed values of the magnetic coupling parameter $\beta$ (left panel), and the specific angular momentum $l$ (middle panel). The minima ($r_{\rm min}$) in the effective potential corresponded to stable circular orbits, while the maxima ($r_{\rm max}$) correspond to unstable circular orbits. Additionally, the turning points $r_s$, $r_l$, $r_p$, $r_a$, and the radius of the unstable circular orbit $r_u$ are indicated in the right panel.

Fig. 3.1 indicates that for specific angular momentum values $l > l_{\rm ISCO}$, there are two extreme points in the effective potential, namely $r_{\rm max}$ corresponding to unstable circular orbits and $r_{\rm min}$ corresponding to stable circular orbits. For the specific angular momentum value $l = l_{\rm ISCO}$, there is only one extreme point $r_{\rm min}$, corresponding to the stable circular orbit. However, for specific angular momentum values $l < l_{\rm ISCO}$, there are no extreme points in the effective potential, indicating the absence of any circular orbits in this case. Additionally, insights into the orbits of magnetized test particles can be obtained from the effective potential. In the right panel of Fig. 3.1, we depict the turning points $r_s$ and $r_l$ corresponding to the deflecting trajectories. Furthermore, concerning the planetary bound orbits, we have also denoted the turning points $r_p$ (periapsis), the smallest orbital separation, and $r_a$ (apoapsis), the largest orbital separation, of particles possessing magnetic dipole moment orbiting a Schwarzschild BH within magnetized fields. We will later explore that test particles establish bound orbits if their specific

energy $\mathcal{E}$ is less than $\sqrt{1-\beta}$ and unbound orbits if $\mathcal{E}_u > \mathcal{E} \geq \sqrt{1-\beta}$, where $\mathcal{E}_u^2 = V_{\rm eff}(r_u)$ represents the energy corresponding to the unstable circular orbits at $r_u = r_{\rm max}$.

One can utilize Eqs. (3.9) and (3.12) to derive the general equation of motion in the equatorial plane for angular trajectories. This yields the differential equation

$$\left(\frac{dr}{d\phi}\right)^2 = \frac{r^4\left(1+\beta\sqrt{f(r)}\right)^2}{l^2} \times\left[\mathcal{E}^2 - f(r)\left(1+\frac{l^2}{r^2}-\beta\sqrt{f(r)}\right)\right]. \quad (3.14)$$

In the forthcoming sections of the paper, we will employ this equation to analytically analyse the bound and unbound orbits of magnetized test particles in the spacetime under consideration.

## 3.3 The bound orbits

Following the same procedure as in Ref. [219] to determine the $(l, \mathcal{E})$ parameter space for circular orbits, in this section we will investigate how this space varies with the magnetic coupling constant $\beta$. Subsequently, by employing the conditions $\mathcal{E}^2 = V_{\rm eff}$ and $V'_{\rm eff} = 0$, we can ascertain the specific energy $\mathcal{E}$ and specific angular momentum $l$ of the magnetized particles as

$$l^2 = \frac{Mr_0^2\left[\beta^2 f(r_0) + \left(2-3\beta\sqrt{f(r_0)}\right)\right]}{2(r_0-3M)}, \quad (3.15)$$

$$\mathcal{E}^2 = f(r_0)\left(1-\frac{1}{2}\beta\sqrt{f(r_0)}\right)^2 + \frac{M\left[2-\beta\sqrt{f(r_0)}\left(3-\beta\sqrt{f(r_0)}\right)\right]}{2(r_0-3M)}, \quad (3.16)$$

corresponding to circular orbits at the radius $r = r_0$. It is well-known that to identify stable circular orbits, one should examine the second derivative of the effective potential, namely $V''_{\rm eff} > 0$ indicates stable circular orbits, while

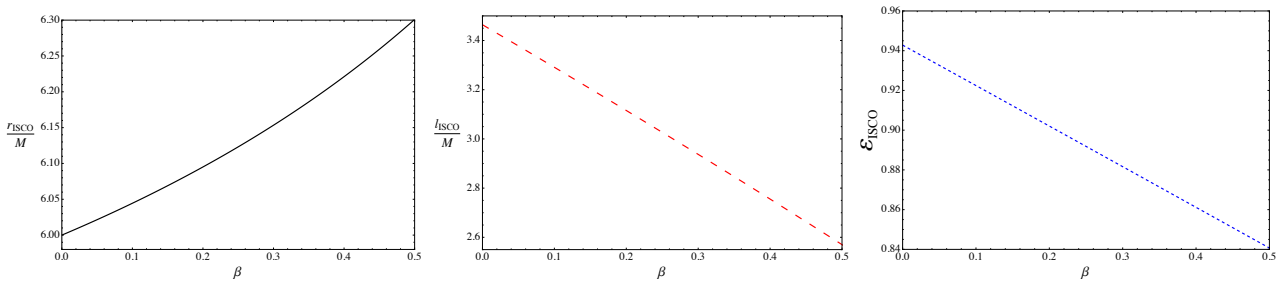


Figure 3.2: Graphical representation of the ISCO radius $r_{\rm ISCO}$, ISCO specific angular momentum $l_{\rm ISCO}$, and the ISCO specific energy $\mathcal{E}_{\rm ISCO}$ along the magnetic coupling parameter $\beta$.

$V''_{\rm eff} < 0$ indicates unstable circular orbits. However, our determination of stable and unstable circular orbits depends on $\beta$. Therefore, in Table 3.1, we present the values of the critical radii of the unstable circular orbits. It is evident that $V''_{\rm eff} > 0$ for $r_0 > r_{\rm max}$, corresponding to stable orbits, and $V''_{\rm eff} < 0$ for $r_{\rm min} < r_0 < r_{\rm max}$, corresponding to unstable orbits. Surely, $r_0 = r_{\rm min}$ corresponds to the ISCO. Therefore, from Table 3.1, one can easily conclude that increasing the magnetic coupling constant $\beta$ leads to an increase in the value of the ISCO radius. To provide more precise insight, in Fig. 3.2, we illustrate how the ISCO radius

| $\beta$ | $r_{\rm min}$ | $r_{\rm max}$ |
|---|---|---|
| 0.0 | $3M$ | $6M$ |
| 0.1 | $3M$ | $6.09984M$ |
| 0.3 | $3M$ | $6.36414M$ |
| 0.5 | $3M$ | $6.78254M$ |

Table 3.1: The radii of stable and unstable circular orbits for different values of the magnetic coupling constant $\beta$.

$r_{\rm ISCO}$, the specific energy $\mathcal{E}_{\rm ISCO}$, and the specific angular momentum $l_{\rm ISCO}$ of the magnetized particle in the ISCO depend on the magnetic coupling constant $\beta$. From Fig. 3.2, one can readily conclude that increasing the magnetic coupling parameter $\beta$ results in a decrease in the specific energy $\mathcal{E}_{\rm ISCO}$ and the specific angular momentum $l_{\rm ISCO}$ of the magnetized particles in the ISCO. In contrast,

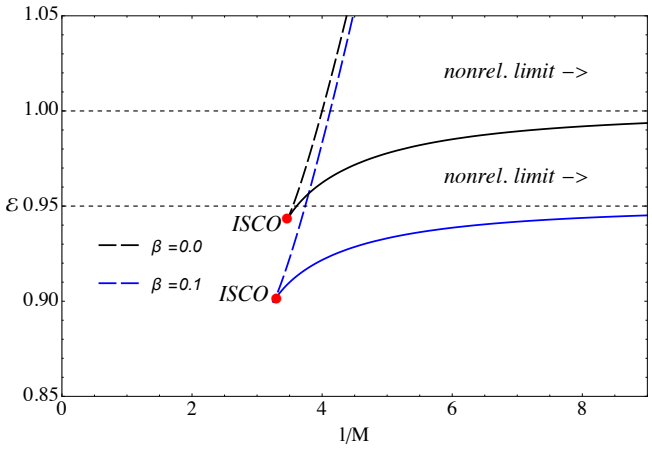


Figure 3.3: Values of the specific energy $\mathcal{E}$ and specific angular momentum $l$ for circular orbits plotted for fixed values of the magnetic coupling parameter $\beta$. Solid lines represent stable circular orbits, while dashed lines represent the radius of unstable circular orbits.

increasing the magnetic interaction term $\beta$ leads to an increase in the value of the ISCO radius $r_{\rm ISCO}$ of the particles with the magnetic dipole moment. Additionally, in Fig. 3.3, we have plotted the domain (for the quantities $\mathcal{E}$, $l/M$, and the line representing the non-relativistic limit, i.e. $l/M \to \infty$), within which, magnetized particles can possess circular orbits.

### 3.3.1 Analytical solution for the angular trajectories

We now endeavor to utilize the classification scheme developed by Levin and Perez-Giz (refer to Ref. [220]) to determine potential values for specific energy $\mathcal{E}$ and specific angular momentum $l$ for a given orbit. To begin this process, we introduce a new variable, $u = 1/r$, in Eq. (3.14), which yields

$$\frac{du}{d\phi} = \pm\frac{\left(1+\beta\sqrt{1-2Mu}\,\right)}{l} \times\sqrt{\mathcal{E}^2-(1-2Mu)\left(1+l^2u^2-\beta\sqrt{1-2Mu}\right)}. \quad (3.17)$$

Subsequently, employing the approximation $\beta\sqrt{1-2Mu} \approx \beta - \beta Mu + \beta\mathcal{O}\left(u^2\right)$ and neglecting the $\beta^2u^4$ term, we arrive at the expression

$$\left(\frac{du}{d\phi}\right)^2 = (1+\beta)\left(au^3-bu^2+cu+d\right), \quad (3.18)$$

where

$$a = 2M\left[(2\beta+1) - \frac{2\beta^2 M^2}{l^2}\right], \tag{3.19a}$$

$$b = (\beta+1) + \frac{2\beta(1-4\beta)M^2}{l^2}, \tag{3.19b}$$

$$c = \frac{M\left[2-\beta\left(5\beta+2\mathcal{E}^2-1\right)\right]}{l^2}, \tag{3.19c}$$

$$d = \frac{(\beta+1)\left(\beta+\mathcal{E}^2-1\right)}{l^2}. \tag{3.19d}$$

From Eq. (3.18), it is evident that for $\mathcal{E}^2 < 1-\beta$, bound orbits occur, which is the primary focus of this section. We assume $u_1 < u_2 < u_3$, where $\{u_1, u_2, u_3\}$ represent the real roots of Eq. (3.18). In the scenario where all these roots are positive, in accordance with the right panel of Fig. 3.1, the radii of the particle orbits vary between $r_a = 1/u_1$ and $r_p = 1/u_2$ (that is, $u_1 \leq u \leq u_2$). This situation corresponds to planetary bound orbits (see, for example, Ref. [221]), wherein the radial position of the test particles oscillates between the apoapsis $u_1$ and the periapsis $u_2$. If one of these roots is negative (for instance, $u_2 < 0$ and $0 < u_1 < u_3$), the test particles will either deflect to infinity at the turning point $r_l = 1/u_1$ or plunge into the black hole at the turning point $r_s = 1/u_3$, as denoted in the right panel of Fig. 3.1. The former type of orbits is termed orbits of the first kind (OFK), while the latter is designated as orbits of the second kind (OSK). These types of orbits are discussed in the next section.

Now, to obtain a general analytical solution for the angular motion, we assume that the magnetized particles commence their motion from $u = u_1$ and $\phi = 0$. Then, Eq. (3.18) can be expressed as

$$\phi = \frac{1}{\sqrt{a(1+\beta)}}\int_{u_1}^{u}\frac{du}{\sqrt{(u-u_1)(u-u_2)(u-u_3)}}, \tag{3.20}$$

which yields the solution

$$\phi(u) = \frac{2F\left(\arcsin\sqrt{\frac{u-u_1}{u_2-u_1}}, k_0\right)}{\sqrt{a(1+\beta)(u_3-u_1)}}, \tag{3.21}$$

where

$$k_0 = \sqrt{\frac{u_2 - u_1}{u_3 - u_1}}. \tag{3.22}$$

In Eq. (3.21), $F(x, k)$ is the incomplete elliptic integral of the first kind, with argument $x$ and modulus $k$ [222]. By performing the inversion of the above solution and restoring the change of variable, we arrive at the analytical expression

$$r(\phi) = \frac{1}{u_1 + (u_2 - u_1)\mathrm{sn}^2(\theta_0, k_0)}, \tag{3.23}$$

where $\theta_0 \equiv \theta_0(\phi) = \sqrt{a(1+\beta)(u_3 - u_1)}\phi/2$. In the above relation, $\mathrm{sn}(\theta, k)$[1] denotes the Jacobi elliptic sine function, with argument $\theta$ and modulus $k$.

### 3.3.2 Periodic orbits for fixed topological characteristics and the impact of eccentricities

The roots of the characteristic polynomial (3.18) can be expressed in the following form [221]:

$$u_1 = \frac{1 - e}{\lambda}, \tag{3.24a}$$

$$u_2 = \frac{1 + e}{\lambda}, \tag{3.24b}$$

$$u_3 = \frac{b}{(1+\beta)a} - \frac{2}{\lambda}, \tag{3.24c}$$

[1]The well-known incomplete elliptic integral of the first kind is given by the general form [222]

$$\theta = F(\phi, k) = \int_0^{\phi} \frac{dt}{\sqrt{1 - k^2 \sin^2 t}},$$

where $\phi = F^{-1}(\theta, k) = \mathrm{am}(\theta, k)$ is the Jacobi amplitude. This way, the Jacobi elliptic sine function is defined as

$$\sin\phi = \sin\big(\mathrm{am}(\theta, k)\big) = \mathrm{sn}(\theta, k).$$

where $e$ and $\lambda$ denote eccentricity and the latus rectum, respectively. For bound orbits, the condition $0 \leq e < 1$ applies. Then we will have

$$u_3 - u_1 = \frac{b}{(1+\beta)a} - \frac{3-e}{\lambda}, \tag{3.25a}$$

$$u_2 - u_1 = \frac{2e}{\lambda}. \tag{3.25b}$$

Accordingly, the exact solution for bound orbits can be written as

$$r(\phi) = \frac{\lambda}{1 - e + 2e\mathrm{sn}^2(\theta_1, k_1)}, \tag{3.26}$$

in which

$$\theta_1 \equiv \theta_1(\phi) = \sqrt{b - \frac{a(1+\beta)(3-e)}{\lambda}}\,\frac{\phi}{2}, \tag{3.27a}$$

$$k_1 = \sqrt{\frac{2ea(1+\beta)}{\lambda - a(1+\beta)(3-e)}}. \tag{3.27b}$$

Considering the oscillation of the radial coordinate between $u_1$ and $u_2$ during one period of planetary orbits, one can determine the associated change in the azimuth angle using Eq. (3.21). This calculation results in,

$$\begin{aligned} \Delta\phi_u = 2\phi(u_2) &= \frac{4K(k_0)}{\sqrt{a(1+\beta)(u_3 - u_1)}} \\ &= \frac{4K(k_1)}{\sqrt{b - \frac{a(1+\beta)(3-e)}{\lambda}}}, \end{aligned} \tag{3.28}$$

where $K(k)$ is the complete elliptic integral of the first kind [222].

Levin and Perez-Giz [220] proposed a taxonomy scheme in the form

$$q + 1 = \omega + \frac{v}{z} + 1 = \frac{\Delta\phi_u}{2\pi}, \tag{3.29}$$

where $\omega$, $v$, and $z$ represent the whirl, vertex, and zoom numbers, respectively. Subsequently, Equation (3.28) can be reformulated as

$$q + 1 = \frac{2K(k_1)}{\pi\sqrt{b - \frac{a(1+\beta)(3-e)}{\lambda}}}. \tag{3.30}$$

Furthermore, for each $e$ and $\lambda$, the corresponding specific angular momentum and specific energy can be found using Eqs. (3.18) and (3.24) as

$$\begin{aligned}\mathcal{E}^2 &= \frac{1}{\lambda\Psi}\Big\{(1+\beta)\Big[2(1-\beta)\lambda^3 \\ &\quad -4\beta^2\left(1-e^2\right)^2 M^3\Big] + \Theta + \Phi\Big\}, \qquad (3.31)\\ l^2 &= \frac{(\beta+1)M\Xi}{\Psi}, \qquad (3.32)\end{aligned}$$

where the coefficients involved are provided in appendix 3.8.

Now, we can illustrate the periodic orbits of the magnetized particles for selected values of the periodic orbit parameters $(z, \omega, v)$ and eccentricity $e$. To achieve this, we numerically solve Eq. (3.30) to obtain $\lambda$ and then determine the corresponding specific energy and specific angular momentum using Eq. (3.32). In our numerical calculation of $\lambda$, we have disregarded the term $\sim \beta^2/l^2$ in $a$ and, $b$ as it is considerably smaller than $\sim \beta$. Subsequently, Tables (3.2), (3.3), and (3.4) present numerical values of the latus rectum $\lambda$, along with the corresponding specific energy $\mathcal{E}$ and specific angular momentum $l$, for the periodic orbits $(4, 0, 1)$, $(3, 0, 1)$, and $(2, 0, 1)$, respectively. These tables reveal that the magnetic interaction term $\beta$ leads to an enlargement of the orbits of magnetized particles. This expansion can be attributed to the repulsive interaction between magnetized particles and an external uniform magnetic field $B$. Subsequently, plotting orbits for these selected values is straightforward, as demonstrated in Cartesian coordinates in Fig. 3.4. The diagrams in this figure illustrate how the magnetic interaction term $\beta$ contributes to the expansion of periodic orbits for test particles with dipole magnetic moment.

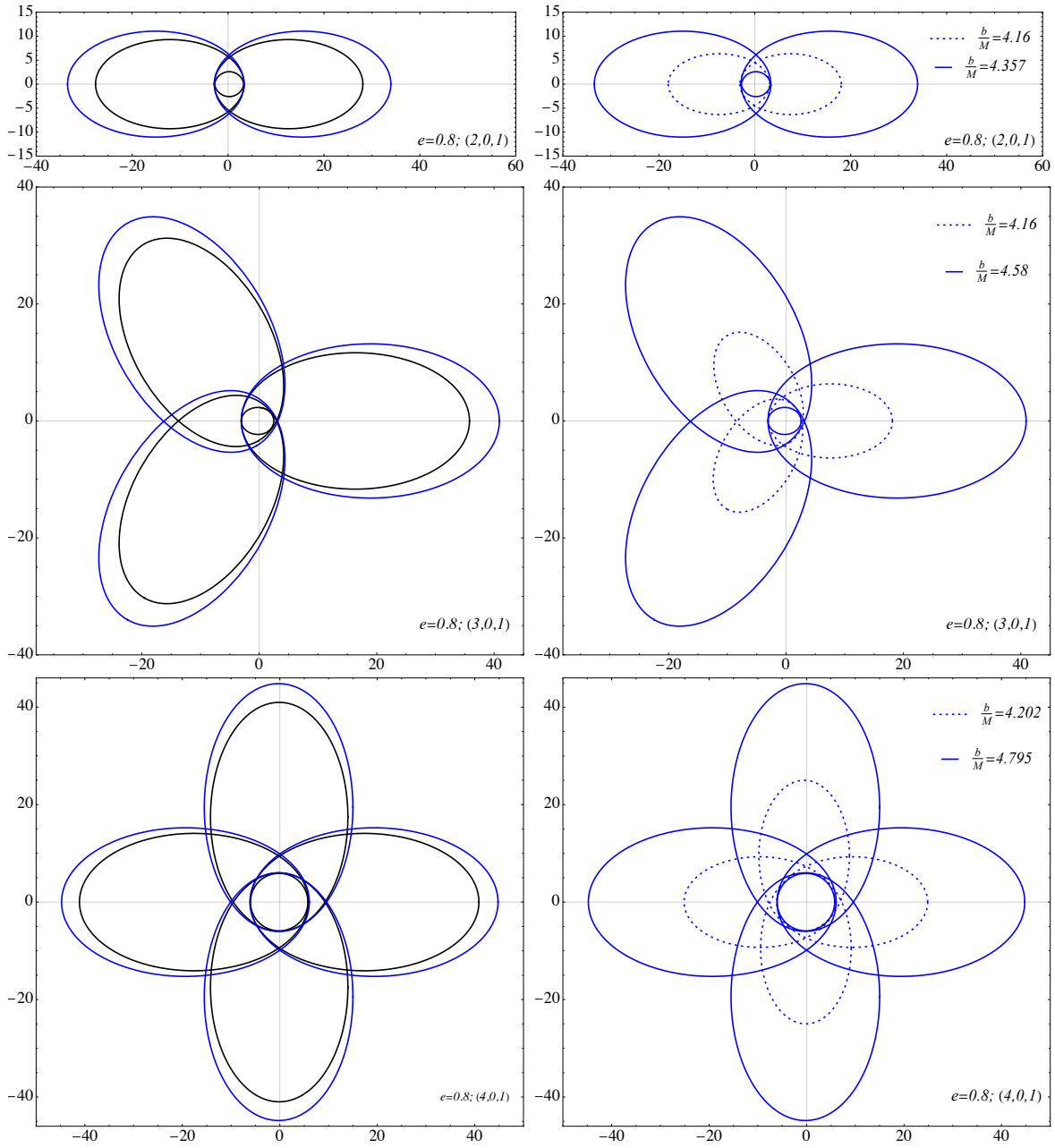


Figure 3.4: Orbits corresponding to various eccentricities: blue orbits represent $\beta = 0.1$, while black orbits represent $\beta = 0.0$. The black hole is assumed to be positioned at the origin. Here $b = \frac{l}{\mathcal{E}}$ is the impact parameter.

| $\beta$ | $e$ | $\lambda$ | $l$ | $\mathcal{E}$ |
|---|---|---|---|---|
| 0.0 | 0.5 | $16.7637M$ | $4.56019M$ | 0.978644 |
| 0.0 | 0.8 | $16.9124M$ | $4.64227M$ | 0.989591 |
| 0.0 | 0.8 | $8.40393M$ | $3.85035M$ | 0.98 |
| 0.1 | 0.5 | $17.8396M$ | $4.39676M$ | 0.930824 |
| 0.1 | 0.8 | $18.2964M$ | $4.50733M$ | 0.940086 |
| 0.1 | 0.8 | $11.1572M$ | $3.92914M$ | 0.935 |

Table 3.2: The specific energy $\mathcal{E}$ and specific angular momentum $l$ values corresponding to selected eccentricity $e$ and the periodic orbit $(4, 0, 1)$, with fixed values of the magnetic coupling parameter $\beta$.

| $\beta$ | $e$ | $\lambda$ | $l$ | $\mathcal{E}$ |
|---|---|---|---|---|
| 0.0 | 0.5 | $13.8243M$ | $4.25126M$ | 0.974472 |
| 0.0 | 0.8 | $13.9918M$ | $4.34876M$ | 0.987505 |
| 0.1 | 0.5 | $15.3592M$ | $4.17356M$ | 0.928205 |
| 0.1 | 0.8 | $15.8208M$ | $4.29611M$ | 0.938799 |
| 0.1 | 0.8 | $7.60573M$ | $3.86844M$ | 0.93 |

Table 3.3: The same table as in Table 3.2 for the periodic orbit $(3, 0, 1)$.

| $\beta$ | $e$ | $\lambda$ | $l$ | $\mathcal{E}$ |
|---|---|---|---|---|
| 0.0 | 0.5 | $10.9382M$ | $3.94488M$ | 0.968567 |
| 0.0 | 0.8 | $11.145M$ | $4.06822M$ | 0.984504 |
| 0.1 | 0.5 | $12.7528M$ | $3.94033M$ | 0.924563 |
| 0.1 | 0.8 | $13.2453M$ | $4.0825M$ | 0.936994 |
| 0.1 | 0.8 | $7.60573M$ | $3.86844M$ | 0.93 |

Table 3.4: The same table as in Table 3.2 for the periodic orbit $(2, 0, 1)$.

### 3.3.3 Estimating the magnetic coupling parameter $\beta$ using observed data from the S2 star

Studying the S2 star's orbits provides a unique opportunity to test General Relativity near Sgr A*. It offers insights into stellar dynamics and gravitational forces in the galactic center. The proximity of S2 to the black hole Sgr A* allows exploration of supermassive black hole properties, such as mass and spin. Tracking

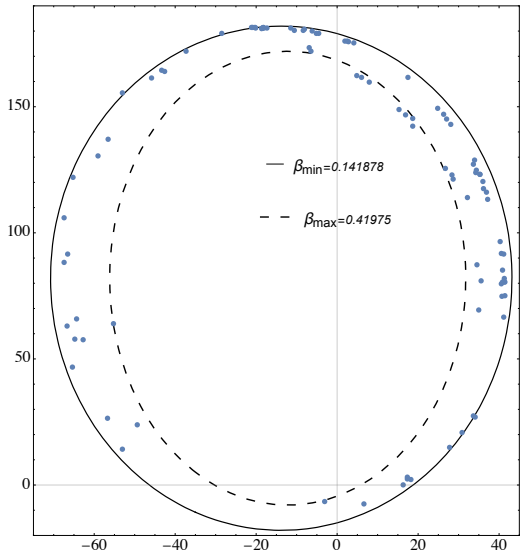


Figure 3.5: Observed trajectory of the star S2 orbiting SgrA*.

S2's orbit over time informs our understanding of black hole characteristics and the surrounding environment. Hence, observation data of the motion of the S2 star near Sgr A* offer a pathway to evaluate various physical theories (see, for example, [223]). In this subsection, we aim to determine the potential values of the magnetic coupling parameter $\beta$ based on the observation data provided in Ref. [224]. To achieve this, we utilize Eq. (3.30) to compute numerical values of $\beta$. Given numerical values of eccentricity $e$ and latus rectum $\lambda$, we can derive numerical values of $\beta$. For a simple elliptic trajectory, the orbit of the S2 star should be $(1, 0, 0)$. Thus, Eq. (3.30) can be represented as

$$\frac{\pi}{2} = \frac{K(k_1)}{\sqrt{b - \frac{a(1+\beta)(3-e)}{\lambda}}}. \tag{3.33}$$

We have depicted the periodic orbit corresponding to the observed trajectory of the S2 star orbiting Sgr A* in Fig. 3.5. In the trajectory calculation, we will assume the external magnetic field around Sgr A* and extend to the S2 star's orbit. In this coordinate system, the $x$ and $y$ axes correspond to offsets in the right ascension ($\Delta\text{RA}/M$) and declination ($\Delta\text{Dec}/M$) of Sgr A*. Additionally, the origin of the coordinate system coincides with the fitted center of mass of Sgr A*. Using Eq. (3.33) together with Eqs. (3.31) and (3.32), we computed the

| $\beta_{\rm max}$ | $\beta_{\rm min}$ | $l_{\rm max}$ | $l_{\rm min}$ | $\mathcal{E}_{\rm max}$ | $\mathcal{E}_{\rm min}$ |
|---|---|---|---|---|---|
| 0.419751 | 0.14249 | $5.02989M$ | $7.4095M$ | 0.871573 | 0.923948 |

Table 3.5: The magnetic coupling parameter $\beta$ values yield periodic orbits for the observed trajectory of the S2 star orbiting Sgr A*, alongside the respective specific energy and specific angular momentum of the S2 star.

possible values of the magnetic coupling parameter $\beta_{\rm min,max}$ and, correspondingly, the specific energy $\mathcal{E}_{\rm min,max}$ and the specific angular momentum $l_{\rm min,max}$ of the S2 star (see Table 3.5). Our calculations indicate that the specific energy and specific angular momentum of the S2 star lie within the ranges $0.871573 \leq \mathcal{E} \leq 0.923948$ and $5.02989M \leq l \leq 7.4095M$, respectively.

Our findings may help us to determine the limits for the magnetic dipole moment of the S2 star with the mass $\approx 14M_\odot$ [225]. The magnetic field in the vicinity of Sgr A* (at the ISCO $6M_{\rm SgrA*} \simeq 0.24$ AU) is approximately 5-100 G [226, 227], and near the orbit of the magnetar PSR 1745-2900 is about mG [228]. To estimate the magnetic dipole moment of the magnetized S2 star, we assume the magnetic field near its orbit is about 1 G. The estimated value of the magnetic interaction parameter $\beta = \mu B/m$ is

$$\mu \simeq 2\beta \times 10^6 \left(\frac{m}{14M_\odot}\right)\left(\frac{B}{1G}\right)^{-1} \mathrm{G}\cdot\mathrm{cm}^3. \tag{3.34}$$

One may have the possible range of the maximum and minimum of the magnetic dipole using the obtained $\beta_{\rm max,min}$ as

$$\frac{1}{3} \leq \left(\frac{\mu}{10^6 \mathrm{G}\cdot\mathrm{cm}^3}\right) \leq \frac{1}{2}. \tag{3.35}$$

## 3.4 unbound orbits

In this section, we will shift our focus from analyzing bound orbits to exploring unbound trajectories, particularly those involving deflection, which hold significant implications for understanding the dynamics of magnetized particles in BH

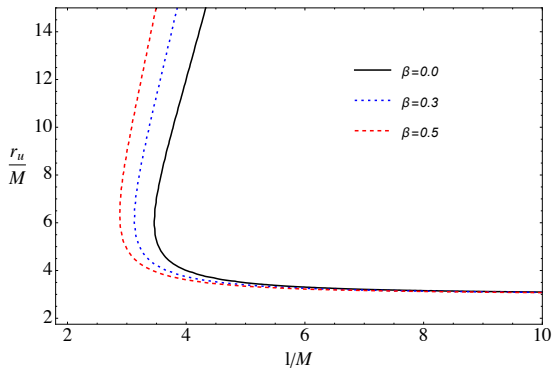


Figure 3.6: The relationship between the radius of unstable circular orbits and specific angular momentum for fixed values of the magnetic coupling constant $\beta$.

spacetimes.

### 3.4.1 Unstable circular orbits

According to the right panel of Fig. 3.1, unstable circular orbits occur at the maximum of the effective potential, where the condition $V'_{\rm eff} = 0$ is satisfied. Figure 3.6 illustrates the relationship between the radius of unstable circular orbits, $r_u$, and the specific angular momentum, considering fixed values of the coupling parameter $\beta$. As the diagram shows, as the $\beta$ parameter increases, the mutual dependence of the above quantities becomes less noticeable. In other words, for larger values of $\beta$, the changes in $r_u$ depend less strongly on the changes in $l$. Furthermore, utilizing Eq. (3.9), we can determine the period of unstable circular orbits as measured by both the comoving (proper) and distant observers for a long-term circular orbit. When considering a complete orbit (i.e. $\phi_u = 2\pi$), one can obtain the following:

$$T_\tau = \frac{2\pi r_u^2}{l_u}\Big[1 + \beta\mathcal{F}(r_u)\Big], \quad T_t = \frac{2\pi r_u^2 \mathcal{E}_u}{l_u f(r_u)}. \tag{3.36}$$

Furthermore, $l_u$ can be derived using the condition $V'_{\rm eff} = 0$. Furthermore, the expression $\dot{r} = 0$ or $\mathcal{E}_u^2 = V_{\rm eff}(r_u)$ leads to the determination of $\mathcal{E}_u$. Therefore, we

obtain,

$$T_\tau = 4\pi r_u \left[1 + \sqrt{f(r_u)}\,\beta\right] \Omega(r_u), \tag{3.37}$$

$$T_t = 4\pi r_u \Omega(r_u)\Lambda(r_u), \tag{3.38}$$

in which

$$\Omega^2(r) = \frac{r - 3M}{M\left(4 - 3\beta\sqrt{f(r)}\right)}, \tag{3.39a}$$

$$\Lambda^2(r) = \frac{1}{f(r)}\left(\frac{1 + l^2}{r^2} - \frac{1}{2}\beta\sqrt{f(r)}\right). \tag{3.39b}$$

We continue this section by exploring the deflecting trajectories.

### 3.4.2 Orbits of the first kind

From Eq. (3.18), it is evident that for $\mathcal{E}^2 \geq 1 - \beta$, magnetized particles follow unbound orbits. Utilizing the condition $dr/d\phi\,|_{r_t} = 0$ of a general turning point $r_t$, and Eq. (3.14), we can find the turning points of the particles, which helps to distinguish between OFK and OSK. Subsequently, in Fig. 3.7, we illustrate how the radii of the turning points depend on the angular momentum for fixed values of the specific energy $\mathcal{E}$ and magnetic coupling parameter $\beta$. From these diagrams, it is evident that particles exhibit two distinct turning point radii: the smallest orbital separation $r_s$ and the largest orbital separation $r_l$. The latter, $r_l$, corresponds to the OFK. Particles reaching this orbit either proceed to infinity following hyperbolic motion in the $\mathcal{E}_u^2 > \mathcal{E}^2 \geq 1 - \beta$ case or engage in periodic orbits when $r_l = r_a$, as observed previously, in the $\mathcal{E}^2 < 1 - \beta$ scenario. Notably, the equation of motion governing OFK is almost identical to that of bound orbits. However, it is crucial to consider that this is one of the roots of Eq. (3.18) is negative for unbound orbits. Consequently, assuming that a magnetized particle

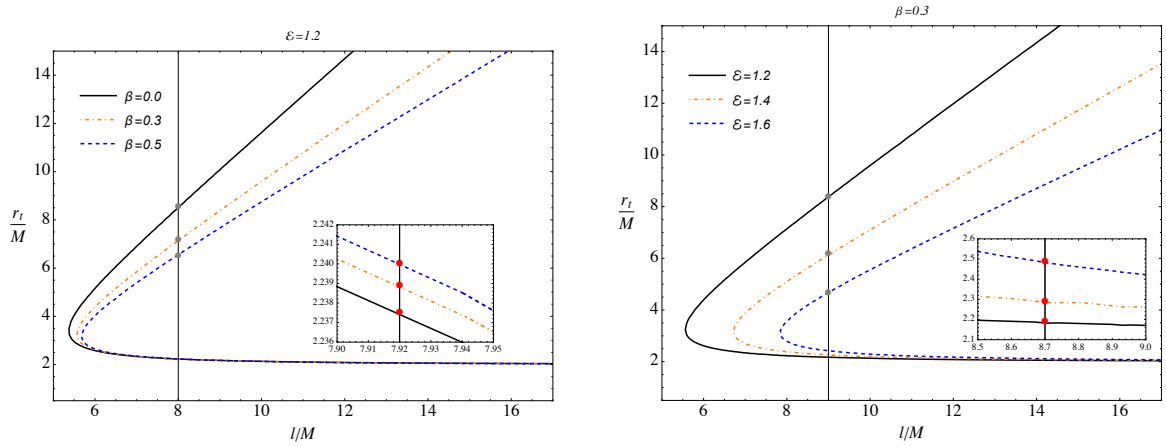


Figure 3.7: The variation of turning point radii with specific angular momentum for fixed values of specific energy $\mathcal{E}$ (left panel), and coupling parameter $\beta$ (right panel). Red points represent the smallest orbital separation $r_s$, while gray points denote the largest orbital separation $r_l$.

initiates its motion from $u = u_2$ and $\phi = 0$, Eq. (3.21) can be expressed as

$$\phi(u) = \frac{2F\left(\arcsin\sqrt{\frac{u-u_1}{u_2-u_1}}, k_0\right) - 2K\left(k_0\right)}{\sqrt{a(1+\beta)(u_3-u_1)}}. \tag{3.40}$$

Following some straightforward calculations, we obtain the trajectory of the magnetized particles as

$$r(\phi) = \frac{1}{u_1 + (u_2-u_1)\mathrm{sn}^2\Big(\theta_0 + K(k_0), k_0\Big)}. \tag{3.41}$$

Similarly to Eqs. (3.24), we can express the roots of Eq. (3.18) in the same manner, however, here $e \geq 1$ as we are dealing with hyperbolic orbits. Then Eq. (3.41) can be expressed as

$$r(\phi) = \frac{\lambda}{1 - e + 2e^2\Big(\theta_1 + K(k_1), k_1\Big)}. \tag{3.42}$$

We have determined the corresponding specific energy and angular momentum for each $e$ and $\lambda$ in Eq. (3.32). Furthermore, in Table 3.6, we have provided the values of the latus rectum and the specific angular momentum for the selected values of specific energy $\mathcal{E}$, eccentricity $e$, and magnetic coupling constant $\beta$. Hence, plotting the hyperbolic trajectories of the magnetized particles is now

| $\beta$ | $e$ | $\lambda$ | $l$ | $\mathcal{E}$ |
|---|---|---|---|---|
| 0.0 | 1.5 | $6.28198M$ | $6.18387M$ | 1.2 |
| 0.0 | 1.5 | $5.52617M$ | $10.5156M$ | 1.5 |
| 0.0 | 2.0 | $11.4327M$ | $5.43019M$ | 1.2 |
| 0.0 | 2.0 | $8.23412M$ | $7.41205M$ | 1.5 |
| 0.3 | 1.5 | $8.56076M$ | $13.1119M$ | 1.2 |
| 0.3 | 1.5 | $8.43699M$ | $19.1212M$ | 1.5 |
| 0.3 | 2 | $11.9084M$ | $8.70001M$ | 1.2 |
| 0.3 | 2 | $11.3611M$ | $12.3606M$ | 1.5 |

Table 3.6: The specific angular momentum and latus rectum values corresponding to selected specific energy and eccentricity, with fixed magnetic coupling parameter.

straightforward. In Fig. 3.8, we depict the OFK for the particles around the BH. Given the behavior of particles and their deflection from the BH, the concept of OFK in this context aligns with the magnetic counterpart of the gravitational Rutherford scattering (see Refs. [182, 188]). The scattering process can be either repulsive or attractive, depending on the eccentricity $e$ and, correspondingly, the specific energy $\mathcal{E}$ and specific angular momentum $l$ associated with this eccentricity. The diagrams show that neutral particles approach the BH more closely than magnetized particles just before heading toward infinity. Similarly to bound orbits, this phenomenon can be attributed to the repulsive nature of the magnetic interaction between magnetized test particles and the external magnetic field $B$. Furthermore, for identical specific energy values, the influence of eccentricity becomes apparent in the transition between attractive and repulsive OFK. An increase in this parameter enhances the tendency of particles to move away from the BH.

### 3.4.3 Orbits of the second kind

As depicted in Fig. 3.7, magnetized particles exhibit two distinct turning points during their unbound orbits. In particular, the smallest orbital separation,

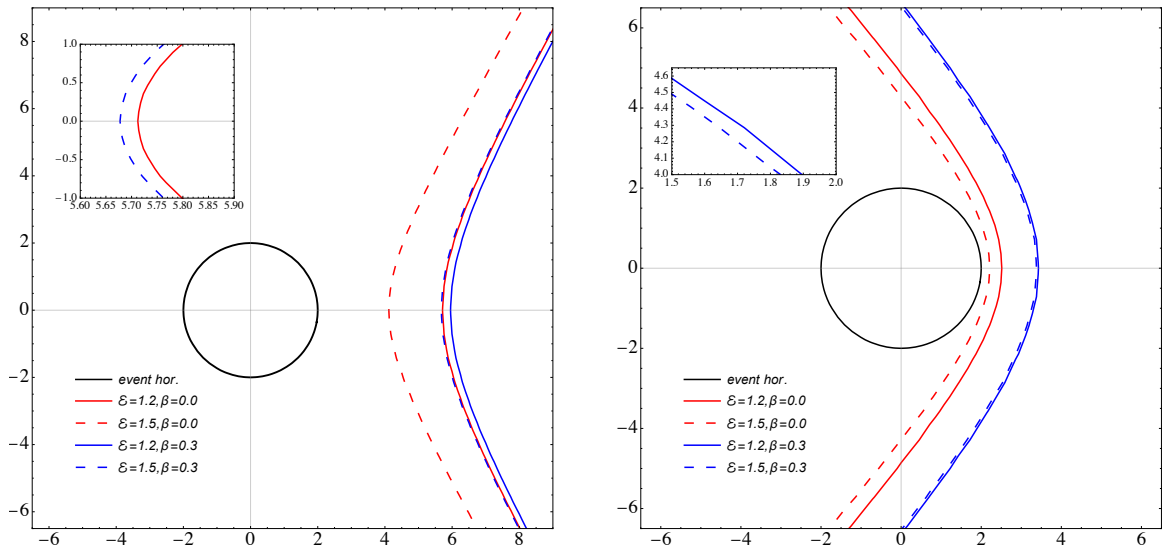


Figure 3.8: The gravitational Rutherford scattering plotted for $e = 1.5$ (left panel), and for $e = 2$ (right panel).

denoted as $r_s$, corresponds to the OSK. In this scenario, particles reaching $r_s$ are drawn into the event horizon by spiraling motion. Assuming particles commence their motion from the point $u = u_3 = 1/r_s$ and $\phi = 0$, integration of Eq. (3.20) yields

$$\phi(u) = \frac{2}{\sqrt{a(1+\beta)(u_3-u_1)}}\left[F\left(\arcsin\sqrt{\frac{u-u_1}{u_2-u_1}}, k_0\right)\right. \\ \left. -F\left(\arcsin\frac{1}{k_0}, k_0\right)\right], \quad (3.43)$$

which enables us to find the analytical solution for the OSK as

$$r(\phi) = \frac{1}{u_1 + (u_2-u_1)\mathrm{sn}^2\left(\theta_0 + F\left(\arcsin\frac{1}{k_0}, k_0\right), k_0\right)}. \quad (3.44)$$

In Fig. 3.9, we illustrate the trajectories of magnetized particles approaching the BH from a distance $r_s$, with fixed values of $\beta$ and the impact parameter $b = l/\mathcal{E}$. From the figure, we infer that a larger impact parameter results in a more noticeable bending of the trajectories as particles approach the BH, with the turning point positioned at a smaller distance. The magnetic interaction further enhances this bending, especially evident in the final segment before the particles

fall into the BH. Conversely, smaller impact parameters cause the trajectories to start their approach from a more distant location, indicating a turning point at a greater distance from the BH.

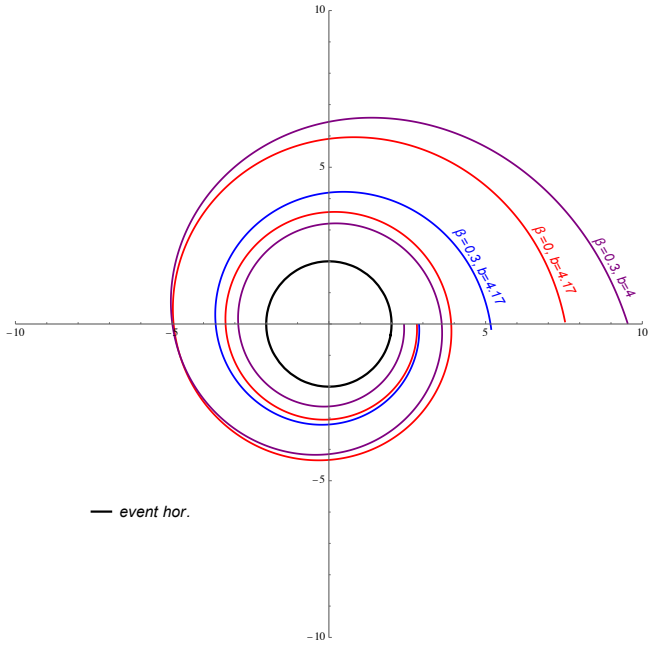


Figure 3.9: The OSK for different values of the $\beta$-parameter and the impact parameter $b$.

So far, we have comprehensively analyzed all possible angular trajectories for magnetized test particles and presented fully analytical solutions to the equations of motion. For the completeness of our study, in the next section, we proceed with the analysis of purely radial trajectories.

## 3.5 Radial trajectories

Studying particles in free fall with zero angular momentum offers several advantages for standard general relativistic tests. One key area of investigation is the gravitational clock effect experienced by falling observers in gravitational fields, which forms the theoretical basis for phenomena such as the gravitational redshift-blueshift of light rays passing near a BH. Another significant aspect is

the phenomenon of *frozen* infalling objects, observed by distant observers as they approach the event horizon of a BH. This stems from the disparities in time measurements between distant observers ($t$) and falling observers ($\tau$), and provides valuable insight into gravitational effects and their implications for our understanding of spacetime dynamics [229, 230, 231]. Hence, the radial motion of magnetized particles without angular momentum also presents an interesting subject to explore.

For purely radial orbits, the effective potential (3.13) adopts the following form:

$$V_{\rm eff} = f(r)\big[1-\beta\mathcal{F}(r)\big], \tag{3.45}$$

which, together with Eqs. (3.11) and (3.13) enables us to establish relationships for the radial velocities as

$$\left(\frac{dr}{d\tau}\right)^2 = \mathcal{E}^2 - f(r)\big[1-\beta\mathcal{F}(r)\big], \tag{3.46}$$

$$\left(\frac{dr}{dt}\right)^2 = \Big\{f(r)\big[1+\beta\mathcal{F}(r)\big]\Big\}^2 \times\Big\{1-\frac{f(r)}{\mathcal{E}^2}\big[1+\beta\mathcal{F}(r)\big]\Big\}. \tag{3.47}$$

In obtaining analytical representations for the time parameters, we derived power series expansions for Eqs. (3.46) and (3.47) centered at $\beta = 0$ up to the second order. Upon integrating these radial velocities, we can determine the radial dependence of the time parameters for magnetized particles that initiate their motion from the point $r_0$. This procedure yields

$$\tau(r) = \mathcal{T}_\tau(r_0) - \mathcal{T}_\tau(r), \tag{3.48}$$

$$t(r) = \mathcal{T}_t(r_0) - \mathcal{T}_t(r), \tag{3.49}$$

where

$$\mathcal{T}_\tau(r) = \frac{1}{8}\Big[\mathcal{A}_\tau + \mathcal{B}_\tau - \mathcal{C}_\tau + \mathcal{D}_\tau\Big], \tag{3.50a}$$

$$\mathcal{T}_t(r) = \frac{1}{8}\mathcal{E}\Big[\mathcal{A}_t + \mathcal{B}_t - \mathcal{C}_t - \mathcal{D}_t\Big]. \tag{3.50b}$$

The expansion coefficients are shown in the Appendix 3.9. In Fig. 3.10, we depict the dependency of the proper time and coordinate time of magnetized particles on their distance from the BH. This illustration highlights that while a falling observer may perceive particles crossing the event horizon, the process takes an infinite amount of time for a distant observer.

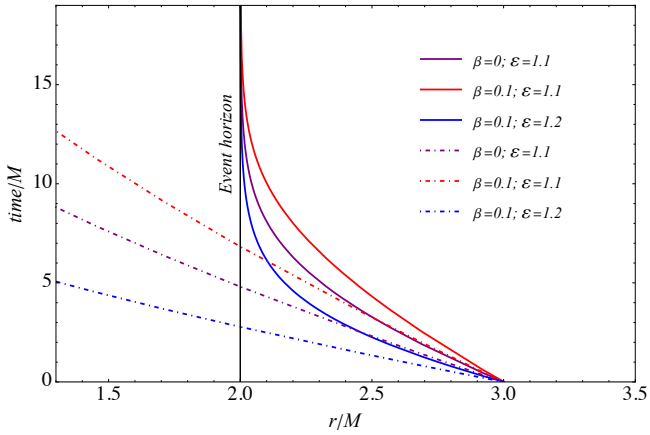


Figure 3.10: Radial profiles of proper time (dot-dashed curves) and coordinate time (solid curves) for test particles on radial orbits, plotted for various values of the $\beta$-parameter and specific energy.

Having thoroughly investigated the angular and radial motion of magnetized particles through comprehensive analytical methods, we have explored various aspects of their trajectory dynamics. With this in mind, we close our discussion at this point and proceed to summarize our findings in the next section.

## 3.6 Conclusion

This study investigated particles' bound and unbound orbits with a dipole moment as they approached a magnetized Schwarzschild BH. Magnetization of the BH was achieved by assuming proportionality between the four-potential and a space-like Killing vector. We constructed the Lagrangian dynamics for test particles, where the magnetic moment directly contributed to their conjugate momenta, with a magnetic interaction parameter $\beta$ playing a crucial role in determining the

magnetic field's effects on particle motion. We derived and analyzed the effective potential experienced by approaching particles, classifying possible bound and unbound orbits based on their specific energy and angular momentum. Bound orbits resembled planetary orbits oscillating between apoapsis and periapsis, with the possibility of complete circularity at the minimum of the effective potential, determining the ISCO. We noted that while the ISCO radius increased with $\beta$, it caused decreases in the specific energy and angular momentum of particles on the ISCO. Analytical solutions to the angular equations of motion for bound orbits were expressed in terms of elliptic integrals and Jacobi elliptic functions, with a precise classification of orbits based on topological characterization. Simulating various bound orbits with different eccentricities revealed topological variations and geometric extensions in the exterior spacetime of the BH. Comparisons between observed positions of the S2 star around Sgr A* and theoretical predictions were made for two different values of $\beta$, calculating minimum and maximum values for this parameter, as well as specific energy and specific angular momentum of the S2 star. We found that the magnetic dipole moment associated with the S2 star was on the order of $10^6\,\mathrm{G}\cdot\mathrm{cm}^3$. Unbound orbits, classified as unstable circular orbits, OFK, and OSK, either deflected from the BH to infinity or fell inexorably onto the event horizon. The period of unstable circular orbits was calculated for comoving and distant observers, and the OFK was likened to the magnetic counterpart of gravitational Rutherford scattering. For such deflecting trajectories, the characteristic polynomial of the equation of motion had only two positive roots, leading to analytical solutions differing in elliptic integrals' arguments. The scattering of test particles could be attractive or repulsive for the OFK, depending on eccentricity. The OSK trajectory curvature increased with the magnetic interaction parameter, resulting in a smaller turning point. Lastly, we explored purely radial orbits for magnetized particles, obtaining the radial

profile of proper time for infalling observers and coordinate time for distant observers. The study of magnetized particles in BH spacetimes offers new avenues for investigating relativistic stars at galaxy centers potentially associated with magnetic fields. Expanding models to include BHs with more degrees of freedom could advance research in relativistic astrophysics, a direction for future studies.

## 3.7 Appendix. A uniform magnetic field around the self-dual black hole in Loop Quantum Gravity

Here, we solve the differential Eq. (2.15) analytically. To this end, we expend it into powers of small $P \ll 1$ and obtain the second order differential equation as follows:

$$C''_\phi \left(4Pr\left(r^2 - Mr\right) + r^2(r-2M)\right) + C'_\phi\Big(2P\left(8r^2 - 6Mr\right) + \\ +2\left(2r^2 - 3Mr\right)\Big) - 8MPC_\phi + \frac{1}{r}O(P)^2 = 0\,, \tag{3.51}$$

which solves to give the following solution

$$C_\phi = K_2(-4Pr - r)^{-\frac{\sqrt{1-2P}}{\sqrt{2P+1}}-1}[2M(2P+1)]^{1-\frac{\sqrt{1-2P}}{\sqrt{2P+1}}}\Big[(4Pr+r)^{\frac{2\sqrt{1-2P}}{\sqrt{2P+1}}}$$

$$\times {}_2F_1\left(a_0, b_0; c_0; z_0\right) + K_1(-2M(2P+1))^{\frac{2\sqrt{1-2P}}{\sqrt{2P+1}}}$$

$$\times {}_2F_1\left(2-a_0, 4-b_0; 2-c_0; z_0\right)\Big]\,. \tag{3.52}$$

Here $K_1$, $K_2$ and ${}_2F_1(a,b;c;z) = \Sigma_{n=0}^{\infty}\frac{(a)_n(b)_n}{(c)_n}\frac{z^n}{n!}$ are the integration constants and Hypergeometric function, respectively. Also we have introduced new variables as $a_0 = \frac{\sqrt{1-2P}}{\sqrt{2P+1}} - 1$, $b_0 = \frac{\sqrt{1-2P}}{\sqrt{2P+1}} + 2$, $c_0 = \frac{2\sqrt{1-2P}}{\sqrt{2P+1}} + 1$, $z_0 = \frac{4Pr+r}{4PM+2M}$. It is obvious from the above equation that the constant $K_1$ can easily lose its meaning in the limit of $P = 0$ that restores Schwarzschild black hole case. Hence, recalling Eq. (3.53),

we derive the following expression for $C_\phi$

$$C_\phi = K_2 \left(2P + \frac{1}{2}\right)^{\frac{\sqrt{1-2P}}{\sqrt{2P+1}}-1} (M(2P+1))^{1-\frac{\sqrt{1-2P}}{\sqrt{2P+1}}} r^{\frac{\sqrt{1-2P}}{\sqrt{2P+1}}-1} \times {}_2F_1\left(a_0, b_0; c_0; z_0\right). \tag{3.53}$$

In the case when $P = 0$ (i.e., Schwarzschild black hole case), we derive $C_\phi = \frac{B_0}{2}$, which allows one to find $K_2 = \frac{B_0}{2}$ easily. Taken all together, for the self-dual black hole immersed in an external uniform magnetic field in LQG , the four potential of the electromagnetic field can be obtained as follows:

$$A^\mu = \frac{B_0}{2}(\mathcal{B})^{\mathcal{A}} \times_2 F_1\left(\mathcal{A}, \mathcal{A}+3; 2\mathcal{A}+3; \mathcal{B}\right) \xi^\mu_\phi\,, \tag{3.54}$$

where we have defined $\mathcal{A} = \sqrt{\frac{1-2P}{1+2P}} - 1$ and $\mathcal{B} = \frac{r(4P+1)}{2M(2P+1)}$ as new variables.

## 3.8 Appendix A: The coefficients of Eqs. (3.31) and (3.32)

These coefficients are as follows:

$$\Phi = 4\left(\beta+1\right)\left(2\beta+1\right)\left[\beta(5\beta-1)-2\right]\left(e^2+1\right)\lambda M^2, \tag{3.55a}$$

$$\Psi = 8\beta\left(\beta+1\right)\left(2\beta+1\right)\left(1-e^2\right)M^2 - 2\left(\beta+1\right)\lambda^2 - 2\lambda M\Big\{\beta\Big[3\beta(2\beta+5)+13\Big] + \Big[\beta(\beta+1)(2\beta+3)+1\Big]e^2 + 3\Big\}, \tag{3.55b}$$

$$\Xi = \left(-3\beta^2-\beta+2\right)\lambda^3 + 16\beta^3\left(1-e^2\right)M^3 - 4\left(\beta+1\right)\beta^2\left(e^2+3\right)\lambda M^2, \tag{3.55c}$$

$$\Theta = \lambda^2 M\Big\{\beta\Big[\beta\Big(6\beta(2\beta+3)-1\Big) + \Big(\beta\left(4\beta^2+6\beta-7\right)-5\Big)e^2 - 19\Big] - 8\Big\}. \tag{3.55d}$$

## 3.9 Appendix B: The coefficients of Eqs. (3.50)

These coefficients are as follows:

$$\mathcal{A}_\tau = \frac{r\sqrt{\mathcal{E}^2 - f(r)}\left[-4M^2\left(3\beta^2\mathcal{E}_1 - 8\mathcal{E}_0^2\right) - 4Mr\mathcal{E}_0\left(\beta^2\mathcal{E}_2 - 8\mathcal{E}_0^2\right) + r^2\mathcal{E}_0\left(3\beta^2 + 8\mathcal{E}_0^2\right)\right]}{\mathcal{E}_0^3\left(2M + r\mathcal{E}_0\right)^2}, \tag{3.56a}$$

$$\mathcal{B}_\tau = \frac{M\left[3\beta^2\left(6\mathcal{E}^2 - 1\right) + 8\mathcal{E}_0^2\right]\ln\left(\frac{2(M+r\mathcal{E}_0)}{\sqrt{\mathcal{E}_0}} + 2r\sqrt{\mathcal{E}^2 - f(r)}\right)}{\mathcal{E}_0^{7/2}}, \tag{3.56b}$$

$$\mathcal{C}_\tau = \frac{4\beta r\sqrt{f(r)}\sqrt{\mathcal{E}^2 - f(r)}\left(M\mathcal{E}_3 + r\mathcal{E}_0\right)}{\mathcal{E}_0^2\left(2M + r\mathcal{E}_0\right)}, \tag{3.56c}$$

$$\mathcal{D}_\tau = \frac{12\beta M\mathcal{E}^2\ln\left(2r\sqrt{f(r)}\sqrt{\mathcal{E}^2 - f(r)} - \frac{2\left[M\left(\mathcal{E}^2-2\right)-r\mathcal{E}_0\right]}{\sqrt{\mathcal{E}_0}}\right)}{\mathcal{E}_0^{5/2}}, \tag{3.56d}$$

$$\mathcal{A}_t = \frac{r\sqrt{\mathcal{E}^2 - f(r)}\left[4M^2\left(\beta^2\mathcal{E}_4 + 8\mathcal{E}_0^2\right) + 4Mr\mathcal{E}_0\left(\beta^2\mathcal{E}_5 + 8\mathcal{E}_0^2\right) + r^2\mathcal{E}_0^2\left(\beta^2\mathcal{E}_6 + 8\mathcal{E}_0^4\right)\right]}{\mathcal{E}_0^3\left(2M + r\mathcal{E}_0\right)^2}, \tag{3.56e}$$

$$\mathcal{B}_t = \frac{M\left[\beta^2\mathcal{E}_4 - 8\mathcal{E}_0^2\mathcal{E}_7\right]\ln\left(\frac{2(M+r\mathcal{E}_0)}{\sqrt{\mathcal{E}_0}} + 2r\sqrt{\mathcal{E}^2 - f(r)}\right)}{\mathcal{E}_0^{7/2}} - \frac{4\beta r\sqrt{f(r)(\mathcal{E}^2 - f(r))}\left(M\mathcal{E}_3 + r\mathcal{E}\right.}{\mathcal{E}_0^2\left(2M + r\mathcal{E}_0\right)} \tag{3.56f}$$

$$\mathcal{C}_t = \frac{4\beta M\mathcal{E}_9\ln\left(2r\sqrt{f(r)(\mathcal{E}^2 - f(r))} - \frac{2\left[M\left(\mathcal{E}^2-2\right)-r\mathcal{E}_0\right]}{\sqrt{\mathcal{E}_0}}\right)}{\mathcal{E}_0^{5/2}}, \tag{3.56g}$$

$$\mathcal{D}_t = \frac{16M\ln\left(r\left[2\mathcal{E}\sqrt{\mathcal{E}^2 - f(r)} + 2\mathcal{E}_0\right] + 2M\right)}{\mathcal{E}} + \frac{16M\ln rf(r)}{\mathcal{E}}, \tag{3.56h}$$

in which we have defined

$$\mathcal{E}_0 = \mathcal{E}^2 - 1, \tag{3.57a}$$

$$\mathcal{E}_1 = 2\mathcal{E}^6 - 6\mathcal{E}^4 - 1, \tag{3.57b}$$

$$\mathcal{E}_2 = 2\mathcal{E}^6 - 9\mathcal{E}^4 - 3, \tag{3.57c}$$

$$\mathcal{E}_3 = 4\mathcal{E}^2 + 2, \tag{3.57d}$$

$$\mathcal{E}_4 = 16\mathcal{E}^4 - 8\mathcal{E}^2 + 7, \tag{3.57e}$$

$$\mathcal{E}_5 = 13\mathcal{E}^4 - 10\mathcal{E}^2 + 7, \tag{3.57f}$$

$$\mathcal{E}_6 = 8\mathcal{E}^4 - 12\mathcal{E}^2 + 7, \tag{3.57g}$$

$$\mathcal{E}_7 = 2\mathcal{E}^2 - 3, \tag{3.57h}$$

$$\mathcal{E}_8 = 2\mathcal{E}^4 - 3r\mathcal{E}^2 + r, \tag{3.57i}$$

$$\mathcal{E}_9 = 2\mathcal{E}^4 - 7\mathcal{E}^2 + 2. \tag{3.57j}$$

# Main results and conclusions

Below we present the main results of the dissertation.

1. We found an novel analytical Schwarzschild-like BH in Dehnen-type DM halo. Additionally, we analyzed a newly derived BH solution by examining its spacetime curvature characteristics and energy conditions. This solution could represent an alternative perspective on the interaction of BH-DM systems, providing new insights into the fundamental properties of DM halos

2. We study the motion of magnetic dipoles and electrically charged particles in the vicinity of a self-dual BH in LQG immersed in an external asymptotically uniform magnetic field. We explore the effects of the quantum correction parameter and electromagnetic interactions on the particle geodesics. We derive the field equations and determine the electromagnetic four-vector potential for the case of a self-dual BH in LQG.

3. We investigate the ISCOs for both magnetic dipoles and electrically charged particles in detail, demonstrating that the quantum correction parameter significantly influences on the ISCO radius, causing it to shrink. Additionally, we show that the ISCO radius of magnetic dipoles is greater than that of electrically charged particles due to the magnetic field interaction. We investigate the ISCO parameters (i.e., $r_{ISCO}$, $l_{ISCO}$, $\mathcal{E}_{ISCO}$, $v_{ISCO}$, and $\Omega_{ISCO}$) for magnetic dipoles and electrically charged particles, providing detailed values. Furthermore, we examine the trajectories of charged particles under various

scenarios resulting from the quantum correction parameter $P$. Finally, analyzing the ISCO parameters that define the inner edge of the accretion disk, we explore the accretion disk around a self-dual BH in LQG.

4. We have investigated the bound and unbound motion of magnetized particles orbiting a Schwarzschild BH immersed in an external asymptotically uniform magnetic field, which includes all conceivable types of bounded and unbounded orbits. In particular, for planetary orbits, we perform a comparative analysis of our findings with the observed position of the $S2$ star carrying magnetic dipole moment around Sagittarius $A^*$ (Sgr $A^*$). We found maximum and minimum values for the parameter of magnetic interaction between the magnetic dipole of the star and the external magnetic field, as well as the energy and angular momentum of the $S2$ star. As a result, we obtain estimations of the magnetic dipole of the star in order of $10^6 G \times cm^3$. Additionally, we explore deflecting trajectories akin to gravitational Rutherford scattering. In obtaining the solutions for the orbital equations, we articulate the elliptic integrals and Jacobi elliptic functions, and illustrative figures and simulations augment our study.

# Bibliography


[1] U. Uktamov, M. Alloqulov, S. Shaymatov, T. Zhu, and B. Ahmedov, "Particle dynamics and the accretion disk around a Self-dual Black Hole immersed in a magnetic field in Loop Quantum Gravity," *Phys. Dark Univ.*, vol. 47, p. 101743, 2025.

[2] U. Uktamov, M. Fathi, J. Rayimbaev, and A. Abdujabbarov, "Orbits of particles with magnetic dipole moment around magnetized Schwarzschild black holes: Applications to the S2 star orbit," , vol. 110, no. 8, p. 084084, Oct. 2024.

[3] U. Uktamjon, B. Narzilloev, and B. Ahmedov, "Perturbation of spacetime and electromagnetic field due to massive charged particle around electrically charged stringy black hole," *Eur. Phys. J. Plus*, vol. 139, no. 10, p. 903, 2024.

[4] B. P. Abbott and et al. (Virgo and LIGO Scientific Collaborations), "Observation of Gravitational Waves from a Binary Black Hole Merger," *Phys. Rev. Lett.*, vol. 116, no. 6, p. 061102, Feb. 2016.

[5] ——, "Properties of the Binary Black Hole Merger GW150914," *Phys. Rev. Lett.*, vol. 116, no. 24, p. 241102, Jun. 2016.

[6] K. Akiyama and et al. (Event Horizon Telescope Collaboration), "First M87 Event Horizon Telescope Results. I. The Shadow of the Supermassive Black Hole," *Astrophys. J.*, vol. 875, no. 1, p. L1, Apr 2019.

[7] ——, "First Sagittarius A* Event Horizon Telescope Results. I. The Shadow of the Supermassive Black Hole in the Center of the Milky Way," *Astrophys. J. Lett.*, vol. 930, no. 2, p. L12, May 2022.

[8] M. J. Rees, "Black Hole Models for Active Galactic Nuclei," *Annu. Rev. Astron. Astrophys.*, vol. 22, pp. 471–506, Jan. 1984.

[9] J. Kormendy and D. Richstone, "Inward Bound—The Search For Supermassive Black Holes In Galactic Nuclei," *Annu. Rev. Astron. Astrophys.*, vol. 33, p. 581, Jan. 1995.

[10] F. Iocco, M. Pato, and G. Bertone, "Evidence for dark matter in the inner Milky Way," *Nature Phys.*, vol. 11, no. 3, pp. 245–248, Mar. 2015.

[11] G. Bertone and T. M. P. Tait, "A new era in the search for dark matter," *Nature*, vol. 562, no. 7725, pp. 51–56, Oct. 2018.

[12] V. C. Rubin and J. Ford, W. Kent, "Rotation of the Andromeda Nebula from a Spectroscopic Survey of Emission Regions," *Astrophys. J.*, vol. 159, p. 379, Feb. 1970.

[13] E. Corbelli and P. Salucci, "The extended rotation curve and the dark matter halo of M33," *Mon. Not. Roy. Astron. Soc.*, vol. 311, no. 2, pp. 441–447, Jan. 2000.

[14] M. Davis, G. Efstathiou, C. S. Frenk, and S. D. M. White, "The evolution of large-scale structure in a universe dominated by cold dark matter," *Astrophys. J.*, vol. 292, pp. 371–394, May 1985.

[15] M. Persic, P. Salucci, and F. Stel, "The universal rotation curve of spiral galaxies — I. The dark matter connection," *Mon. Not. R. Astron. Soc.*, vol. 281, no. 1, pp. 27–47, Jul. 1996.

[16] M. Valluri, D. Merritt, and E. Emsellem, "Difficulties with Recovering the Masses of Supermassive Black Holes from Stellar Kinematical Data," *Astrophys. J.*, vol. 602, no. 1, pp. 66–92, Feb. 2004.

[17] K. Akiyama and et al. (Event Horizon Telescope Collaboration), "First M87 Event Horizon Telescope Results. VI. The Shadow and Mass of the Central Black Hole," *Astrophys. J.*, vol. 875, no. 1, p. L6, Apr 2019.

[18] C. Bœhm and P. Fayet, "Scalar dark matter candidates," *Nucl. Phys. B*, vol. 683, no. 1, pp. 219–263, Apr. 2004.

[19] G. Bertone, D. Hooper, and J. Silk, "Particle dark matter: evidence, candidates and constraints," *Phys. Rep.*, vol. 405, no. 5-6, pp. 279–390, Jan. 2005.

[20] J. L. Feng, M. Kaplinghat, H. Tu, and H.-B. Yu, "Hidden charged dark matter," *J. Cosmol. Astropart. Phys.*, vol. 2009, no. 7, p. 004, Jul. 2009.

[21] M. Schumann, "Direct detection of WIMP dark matter: concepts and status," *J. Phys. G Nucl. Part. Phys.*, vol. 46, no. 10, p. 103003, Oct. 2019.

[22] S. Babak, J. Gair, A. Sesana, E. Barausse, C. F. Sopuerta, C. P. L. Berry, E. Berti, P. Amaro-Seoane, A. Petiteau, and A. Klein, "Science with the space-based interferometer LISA. V. Extreme mass-ratio inspirals," *Phys. Rev. D*, vol. 95, no. 10, p. 103012, May 2017.

[23] D. A. Brown, J. Brink, H. Fang, J. R. Gair, C. Li, G. Lovelace, I. Mandel, and K. S. Thorne, "Prospects for Detection of Gravitational Waves from Intermediate-Mass-Ratio Inspirals," *Phys. Rev. Lett.*, vol. 99, no. 20, p. 201102, Nov. 2007.

[24] P. Amaro-Seoane, "Detecting intermediate-mass ratio inspirals from the ground and space," *Phys. Rev. D*, vol. 98, no. 6, p. 063018, Sep. 2018.

[25] D. Clowe, M. Bradač, A. H. Gonzalez, M. Markevitch, S. W. Randall, C. Jones, and D. Zaritsky, "A Direct Empirical Proof of the Existence of Dark Matter," *Astrophys. J. Lett.*, vol. 648, no. 2, pp. L109–L113, Sep. 2006.

[26] G. Bertone, D. Hooper, and J. Silk, "Particle dark matter: evidence, candidates and constraints," *Phys. Rep.*, vol. 405, no. 5-6, pp. 279–390, Jan. 2005.

[27] J. G. de Swart, G. Bertone, and J. van Dongen, "How dark matter came to matter," *Nature Astron.*, vol. 1, p. 0059, Mar. 2017.

[28] R. H. Wechsler and J. L. Tinker, "The Connection Between Galaxies and Their Dark Matter Halos," *Annu. Rev. Astron. Astrophys.*, vol. 56, pp. 435–487, Sep. 2018.

[29] D. Merritt, A. W. Graham, B. Moore, J. Diemand, and B. Terzić, "Empirical Models for Dark Matter Halos. I. Nonparametric Construction of Density Profiles and Comparison with Parametric Models," *Astron. J.*, vol. 132, no. 6, pp. 2685–2700, Dec. 2006.

[30] A. A. Dutton and A. V. Macciò, "Cold dark matter haloes in the planck era: evolution of structural parameters for einasto and nfw profiles," *Mon. Not. Roy. Astron. Soc.*, vol. 441, no. 4, p. 3359–3374, May 2014. [Online]. Available: http://dx.doi.org/10.1093/mnras/stu742

[31] J. F. Navarro, C. S. Frenk, and S. D. M. White, "The structure of cold dark matter halos," *Astrophys. J.*, vol. 462, p. 563, May 1996. [Online]. Available: http://dx.doi.org/10.1086/177173

[32] A. Burkert, "The structure of dark matter halos in dwarf galaxies," *Astrophys. J.*, vol. 447, no. 1, Jul. 1995. [Online]. Available: http://dx.doi.org/10.1086/309560

[33] W. Dehnen, "A Family of Potential-Density Pairs for Spherical Galaxies and Bulges," *Mon. Not. R. Astron. Soc.*, vol. 265, p. 250, Nov. 1993.

[34] Shukirgaliyev, B., Otebay, A., Sobolenko, M., Ishchenko, M., Borodina, O., Panamarev, T., Myrzakul, S., Kalambay, M., Naurzbayeva, A., Abdikamalov, E., Polyachenko, E., Banerjee, S., Berczik, P., Spurzem, R., and Just, A., "Bound mass of dehnen models with a centrally peaked star formation efficiency," *Astron. Astrophys.*, vol. 654, p. A53, 2021. [Online]. Available: https://doi.org/10.1051/0004-6361/202141299

[35] M. M. Gohain, P. Phukon, and K. Bhuyan, "Thermodynamics and null geodesics of a Schwarzschild black hole surrounded by a Dehnen type dark matter halo," *Phys. Dark Univ.*, vol. 46, p. 101683, 2024.

[36] R. C. Pantig and A. Övgün, "Dehnen halo effect on a black hole in an ultra-faint dwarf galaxy," *J. Cosmol. Astropart. Phys.*, vol. 2022, no. 8, p. 056, Aug. 2022.

[37] A. Al-Badawi, S. Shaymatov, and Y. Sekhmani, "Schwarzschild black hole in galaxies surrounded by a dark matter halo," *J. Cosmol. Astropart. Phys.*, vol. 2025, no. 2, p. 014, Feb. 2025.

[38] M.-H. Li and K.-C. Yang, "Galactic dark matter in the phantom field," *Phys. Rev. D*, vol. 86, no. 12, p. 123015, Dec 2012.

[39] S. Shaymatov, B. Ahmedov, and M. Jamil, "Testing the weak cosmic censorship conjecture for a Reissner-Nordström-de Sitter black hole surrounded by perfect fluid dark matter," *Eur. Phys. J. C*, vol. 81, no. 7, p. 588, Jul. 2021.

[40] S. Shaymatov, D. Malafarina, and B. Ahmedov, "Effect of perfect fluid dark matter on particle motion around a static black hole immersed in an external magnetic field," *Phys. Dark Universe*, vol. 34, p. 100891, Oct. 2021.

[41] S. Shaymatov, P. Sheoran, and S. Siwach, "Motion of charged and spinning particles influenced by dark matter field surrounding a charged dyonic black hole," *Phys. Rev. D*, vol. 105, no. 10, p. 104059, May 2022.

[42] V. Cardoso, K. Destounis, F. Duque, R. P. Macedo, and A. Maselli, "Black holes in galaxies: Environmental impact on gravitational-wave generation and propagation," *Phys. Rev. D*, vol. 105, no. 6, p. L061501, Mar. 2022.

[43] X. Hou, Z. Xu, M. Zhou, and J. Wang, "Black hole shadow of Sgr A$^*$ in dark matter halo," *J. Cosmol. Astropart. Phys.*, vol. 2018, no. 7, p. 015, Jul. 2018.

[44] Z. Shen, A. Wang, Y. Gong, and S. Yin, "Analytical models of supermassive black holes in galaxies surrounded by dark matter halos," *Phys. Lett. B*, vol. 855, p. 138797, Aug. 2024.

[45] T. Xamidov, U. Uktamov, S. Shaymatov, and B. Ahmedov, "Quasiperiodic oscillations around a Schwarzschild black hole surrounded by a Dehnen type dark matter halo," *Phys. Dark Universe*, vol. 47, p. 101805, Feb. 2025.

[46] A. Al-Badawi and S. Shaymatov, "Astrophysical properties of static black holes embedded in a Dehnen type dark matter halo with the presence of quintessential field," *Chin. Phys. C*, vol. 49, no. 5, p. 055101, May 2025.

[47] ——, "Quasinormal modes and shadow of Schwarzschild black holes embedded in a Dehnen-type dark matter halo exhibiting a cloud of strings," *Commun. Theor. Phys.*, vol. 77, no. 3, p. 035402, Mar. 2025.

[48] M. Alloqulov, T. Xamidov, S. Shaymatov, and B. Ahmedov, "Gravitational waveforms from periodic orbits around a Schwarzschild black hole embedded in a Dehnen-type dark matter halo," *arXiv e-prints*, p. arXiv:2504.05236, Apr. 2025.

[49] T. Matos and D. Nunez, "The general relativistic geometry of the Navarro-Frenk-White model," *Rev. Mex. Fis.*, vol. 51, no. 1, pp. 71–75, Feb. 2005.

[50] Z. Xu, X. Hou, X. Gong, and J. Wang, "Black hole space-time in dark matter halo," *J. Cosmol. Astropart. Phys.*, vol. 2018, no. 9, p. 038, Sep. 2018.

[51] H. Mo, F. C. van den Bosch, and S. White, *Galaxy Formation and Evolution*. Cambridge: Cambridge University Press, 2010.

[52] B. Toshmatov, C. Bambi, B. Ahmedov, A. Abdujabbarov, and Z. Stuchlík, "Energy conditions of non-singular black hole spacetimes in conformal gravity," *European Physical Journal C*, vol. 77, no. 8, p. 542, Aug. 2017.

[53] C. W. Misner, K. S. Thorne, and J. A. Wheeler, *Gravitation*. San Francisco: W. H. Freeman, 1973.

[54] N. Dadhich and S. Shaymatov, "Circular orbits around higher dimensional Einstein and pure Gauss-Bonnet rotating black holes," *Phys. Dark Universe*, vol. 35, p. 100986, Mar. 2022.

[55] ——, "On black hole formation in higher dimensions," *Int. J. Mod. Phys. D*, vol. 31, no. 1, p. 2150120, Oct. 2022.

[56] J. Rayimbaev, S. Shaymatov, and M. Jamil, "Dynamics and epicyclic motions of particles around the Schwarzschild-de Sitter black hole in perfect fluid dark matter," *European Physical Journal C*, vol. 81, no. 8, p. 699, Aug. 2021.

[57] R. J. Adler, "Six easy roads to the Planck scale," *Am. J. Phys.*, vol. 78, no. 9, pp. 925–932, Sep. 2010.

[58] Y. J. Ng, "Selected Topics in Planck-Scale Physics," *Mod. Phys. Lett. A*, vol. 18, no. 16, pp. 1073–1097, Jan. 2003.

[59] A. Borde, A. H. Guth, and A. Vilenkin, "Inflationary Spacetimes Are Incomplete in Past Directions," *Phys. Rev. Lett.*, vol. 90, no. 15, p. 151301, Apr. 2003.

[60] A. Borde and A. Vilenkin, "Eternal inflation and the initial singularity," *Phys. Rev. Lett.*, vol. 72, no. 21, pp. 3305–3308, May 1994.

[61] S. W. Hawking, "The event horizon," in *Black Holes*, C. DeWitt and B. S. DeWitt, Eds. New York: Gordon and Breach, 1973, pp. 1–55.

[62] L. Modesto, "Semiclassical Loop Quantum Black Hole," *Int. J. Theor. Phys.*, vol. 49, no. 8, pp. 1649–1683, Aug. 2010.

[63] L. Modesto and I. Prémont-Schwarz, "Self-dual black holes in loop quantum gravity: Theory and phenomenology," *Phys. Rev. D*, vol. 80, no. 6, p. 064041, Sep. 2009.

[64] S. Sahu, K. Lochan, and D. Narasimha, "Gravitational lensing by self-dual black holes in loop quantum gravity," *Phys. Rev. D*, vol. 91, no. 6, p. 063001, Mar. 2015.

[65] A. Ashtekar, J. Olmedo, and P. Singh, "Quantum Transfiguration of Kruskal Black Holes," *Phys. Rev. Lett.*, vol. 121, no. 24, p. 241301, Dec. 2018.

[66] ——, "Quantum extension of the Kruskal spacetime," *Phys. Rev. D*, vol. 98, no. 12, p. 126003, Dec. 2018.

[67] M. Bojowald, S. Brahma, and D.-h. Yeom, "Effective line elements and black-hole models in canonical loop quantum gravity," *Phys. Rev. D*, vol. 98, no. 4, p. 046015, Aug. 2018.

[68] E. Alesci, S. Bahrami, and D. Pranzetti, "Quantum gravity predictions for black hole interior geometry," *Phys. Lett. B*, vol. 797, p. 134908, Oct. 2019.

[69] M. Assanioussi, A. Dapor, and K. Liegener, "Perspectives on the dynamics in a loop quantum gravity effective description of black hole interiors," *Phys. Rev. D*, vol. 101, no. 2, p. 026002, Jan. 2020.

[70] N. Bodendorfer, F. M. Mele, and J. Münch, "(b,v)-type variables for black to white hole transitions in effective loop quantum gravity," *Phys. Lett. B*, vol. 819, p. 136390, 2021.

[71] ——, "Mass and Horizon Dirac Observables in Effective Models of Quantum Black-to-White Hole Transition," *Class. Quant. Grav.*, vol. 38, no. 9, p. 095002, 2021.

[72] A. Perez, "Black holes in loop quantum gravity," *Rep. Prog. Phys.*, vol. 80, no. 12, p. 126901, Dec. 2017.

[73] A. Barrau, K. Martineau, and F. Moulin, "A Status Report on the Phenomenology of Black Holes in Loop Quantum Gravity: Evaporation, Tunneling to White Holes, Dark Matter and Gravitational Waves," *Universe*, vol. 4, no. 10, p. 102, Oct. 2018.

[74] C. Rovelli, "Black Hole Evolution Traced Out with Loop Quantum Gravity," *APS Physics*, vol. 11, p. 127, Dec. 2018.

[75] A. Ashtekar, "Black Hole Evaporation: A Perspective from Loop Quantum Gravity," *Universe*, vol. 6, no. 2, p. 21, Jan. 2020.

[76] W.-C. Gan, N. O. Santos, F.-W. Shu, and A. Wang, "Properties of the spherically symmetric polymer black holes," *Phys. Rev. D*, vol. 102, no. 12, p. 124030, Dec. 2020.

[77] E. Alesci and L. Modesto, "Particle creation by loop black holes," *Gen. Rel. Grav.*, vol. 46, p. 1656, Feb. 2014.

[78] J.-H. Chen and Y.-J. Wang, "Complex frequencies of a massless scalar field in loop quantum black hole spacetime," *Chin. Phys. B*, vol. 20, no. 3, p. 030401, Mar. 2011.

[79] A. Barrau, C. Rovelli, and F. Vidotto, "Fast radio bursts and white hole signals," *Phys. Rev. D*, vol. 90, no. 12, p. 127503, Dec. 2014.

[80] A. Dasgupta, "Semiclassical Loop Quantum Gravity and Black Hole Thermodynamics," *SIGMA*, vol. 9, p. 013, Feb. 2013.

[81] S. Hossenfelder, L. Modesto, and I. Prémont-Schwarz, "Emission spectra of self-dual black holes," *arXiv e-prints*, p. arXiv:1202.0412, Feb. 2012.

[82] M. B. Cruz, C. A. S. Silva, and F. A. Brito, "Gravitational axial perturbations and quasinormal modes of loop quantum black holes," *Eur. Phys. J. C*, vol. 79, no. 2, p. 157, Feb. 2019.

[83] F. Moulin, K. Martineau, J. Grain, and A. Barrau, "Quantum fields in the background spacetime of a polymeric loop black hole," *Class. Quant. Grav.*, vol. 36, no. 12, p. 125003, Jun. 2019.

[84] F. Moulin, A. Barrau, and K. Martineau, "An Overview of Quasinormal Modes in Modified and Extended Gravity," *Universe*, vol. 5, no. 9, p. 202, Sep. 2019.

[85] M. B. Cruz, F. A. Brito, and C. A. S. Silva, "Polar gravitational perturbations and quasinormal modes of a loop quantum gravity black hole," *Phys. Rev. D*, vol. 102, no. 4, p. 044063, Aug. 2020.

[86] J. S. Santos, M. B. Cruz, and F. A. Brito, "Quasinormal modes of a massive scalar field nonminimally coupled to gravity in the spacetime of self-dual black hole," *Eur. Phys. J. C*, vol. 81, no. 12, p. 1082, Dec. 2021.

[87] C. Liu, T. Zhu, Q. Wu, K. Jusufi, M. Jamil, M. Azreg-Aïnou, and A. Wang, "Shadow and quasinormal modes of a rotating loop quantum black hole," *Phys. Rev. D*, vol. 101, no. 8, p. 084001, Apr. 2020.

[88] T. Zhu and A. Wang, "Observational tests of the self-dual spacetime in loop quantum gravity," *Phys. Rev. D*, vol. 102, no. 12, p. 124042, Dec. 2020.

[89] Y.-C. Liu, J.-X. Feng, F.-W. Shu, and A. Wang, "Extended geometry of Gambini-Olmedo-Pullin polymer black hole and its quasinormal spectrum," *Phys. Rev. D*, vol. 104, no. 10, p. 106001, Nov. 2021.

[90] R. G. Daghigh, M. D. Green, and G. Kunstatter, "Scalar perturbations and stability of a loop quantum corrected Kruskal black hole," *Phys. Rev. D*, vol. 103, no. 8, p. 084031, Apr. 2021.

[91] M. Bouhmadi-López, S. Brahma, C.-Y. Chen, P. Chen, and D.-h. Yeom, "A consistent model of non-singular Schwarzschild black hole in loop quantum gravity and its quasinormal modes," *JCAP*, vol. 2020, no. 7, p. 066, Jul. 2020.

[92] Q.-M. Fu and X. Zhang, "Gravitational lensing by a black hole in effective loop quantum gravity," *Phys. Rev. D*, vol. 105, no. 6, p. 064020, Mar. 2022.

[93] S. Brahma, C.-Y. Chen, and D.-h. Yeom, "Testing Loop Quantum Gravity from Observational Consequences of Nonsingular Rotating Black Holes," *Phys. Rev. Lett.*, vol. 126, no. 18, p. 181301, May 2021.

[94] C. Liu, H. Siew, T. Zhu, Q. Wu, Y. Sun, Y. Zhao, and H. Xu, "Constraints on the rotating self-dual black hole with quasi-periodic oscillations," *JCAP*, vol. 11, p. 096, 2023.

[95] Z.-Y. Tu, T. Zhu, and A. Wang, "Periodic orbits and their gravitational wave radiations in a polymer black hole in loop quantum gravity," *Phys. Rev. D*, vol. 108, no. 2, p. 024035, 2023.

[96] S. Yang, W.-D. Guo, Q. Tan, and Y.-X. Liu, "Axial gravitational quasinormal modes of a self-dual black hole in loop quantum gravity," *Phys. Rev. D*, vol. 108, no. 2, p. 024055, 2023.

[97] J.-M. Yan, C. Liu, T. Zhu, Q. Wu, and A. Wang, "Observational tests of a quantum extension of Schwarzschild spacetime in loop quantum gravity with stars in the Galactic Center," *Phys. Rev. D*, vol. 107, no. 8, p. 084043, 2023.

[98] S. Albuquerque, I. P. Lobo, and V. B. Bezerra, "Massless Dirac perturbations in a consistent model of loop quantum gravity black hole: quasinormal modes and particle emission rates," *Class. Quant. Grav.*, vol. 40, no. 17, p. 174001, 2023.

[99] K. Chen and S.-W. Wei, "Motion of spinning particles around a polymer black hole in loop quantum gravity," 3 2024.

[100] H.-X. Jiang, C. Liu, I. K. Dihingia, Y. Mizuno, H. Xu, T. Zhu, and Q. Wu, "Shadows of loop quantum black holes: semi-analytical simulations of loop

quantum gravity effects on Sagittarius A* and M87*," *JCAP*, vol. 01, p. 059, 2024.

[101] H.-X. Jiang, I. K. Dihingia, C. Liu, Y. Mizuno, and T. Zhu, "Enhanced Blandford Znajek jet in loop quantum black hole," *JCAP*, vol. 05, p. 101, 2024.

[102] R.-T. Chen, S. Li, L.-G. Zhu, and J.-P. Wu, "Constraints from Solar System tests on a covariant loop quantum black hole," *Phys. Rev. D*, vol. 109, no. 2, p. 024010, 2024.

[103] J.-M. Yan, Q. Wu, C. Liu, T. Zhu, and A. Wang, "Constraints on self-dual black hole in loop quantum gravity with S0-2 star in the galactic center," *JCAP*, vol. 09, p. 008, 2022.

[104] D. M. Gingrich, "Quasinormal modes of loop quantum black holes near the Planck scale," *Phys. Rev. D*, vol. 109, no. 4, p. 044044, 2024.

[105] Y. Liu and X. Zhang, "Gravitational waves for eccentric extreme mass ratio inspirals of self-dual spacetime," 4 2024.

[106] Y.-L. Liu, Z.-Q. Feng, and X.-D. Zhang, "Solar system constraints of a polymer black hole in loop quantum gravity," *Phys. Rev. D*, vol. 105, p. 084068, 2022.

[107] C. Bambi, "Testing the kerr nature of stellar-mass black hole candidates by combining the continuum-fitting method and the power estimate of transient ballistic jets," *Phys. Rev. D*, vol. 85, no. 4, p. 043002, Feb 2012.

[108] C. Bambi, J. Jiang, and J. F. Steiner, "Testing the no-hair theorem with the continuum-fitting and the iron line methods: a short review," *Classical and Quantum Gravity*, vol. 33, no. 6, p. 064001, Mar. 2016.

[109] M. A. Abramowicz and P. C. Fragile, "Foundations of Black Hole Accretion Disk Theory," *Living Rev. Relativ.*, vol. 16, no. 1, p. 1, Jan. 2013.

[110] R. P. Fender, T. M. Belloni, and E. Gallo, "Towards a unified model for black hole X-ray binary jets," *Mon. Not. R. Astron. Soc.*, vol. 355, no. 4, pp. 1105–1118, Dec. 2004.

[111] K. Auchettl, J. Guillochon, and E. Ramirez-Ruiz, "New Physical Insights about Tidal Disruption Events from a Comprehensive Observational Inventory at X-Ray Wavelengths," *Astrophys. J.*, vol. 838, no. 2, p. 149, Apr. 2017.

[112] The IceCube Collaboration and et al., "Multimessenger observations of a flaring blazar coincident with high-energy neutrino IceCube-170922A," *Science*, vol. 361, no. 6398, p. eaat1378, Jul. 2018.

[113] C. Bambi, *Black Holes: A Laboratory for Testing Strong Gravity.* Springer, Singapore, 2017.

[114] S. Chandrasekhar, *The mathematical theory of black holes.* New York: Oxford University Press., 1998.

[115] F. de Felice and F. Sorge, "Magnetized orbits around a Schwarzschild black hole," *Class. Quantum Grav.*, vol. 20, pp. 469–481, Feb. 2003.

[116] F. de Felice, F. Sorge, and S. Zilio, "Magnetized orbits around a Kerr black hole," *Class. Quantum Grav.*, vol. 21, pp. 961–973, Feb. 2004.

[117] J. Vrba, A. Abdujabbarov, M. Kološ, B. Ahmedov, Z. Stuchlík, and J. Rayimbaev, "Charged and magnetized particles motion in the field of generic singular black holes governed by general relativity coupled to nonlinear electrodynamics," *Phys.Rev.D*, vol. 101, no. 12, p. 124039, Jun. 2020.

[118] V. P. Frolov and P. Krtouš, "Charged particle in higher dimensional weakly charged rotating black hole spacetime," *Phys. Rev. D*, vol. 83, no. 2, p. 024016, Jan 2011.

[119] V. P. Frolov, "Weakly magnetized black holes as particle accelerators," *Phys. Rev. D*, vol. 85, no. 2, p. 024020, Jan. 2012.

[120] Hussain, S, Hussain, I, and Jamil, M., "Dynamics of a charged particle around a slowly rotating kerr black hole immersed in magnetic field," *Eur. Phys. J. C*, vol. 74, no. 3, p. 210, 2014. [Online]. Available: https://doi.org/10.1140/epjc/s10052-014-3210-y

[121] M. Kološ, A. Tursunov, and Z. Stuchlík, "Possible signature of magnetic fields related to quasi-periodic oscillation observed in microquasars," *Eur. Phys. J. C.*, vol. 77, p. 860, Jul. 2017.

[122] B. Narzilloev, J. Rayimbaev, S. Shaymatov, A. Abdujabbarov, B. Ahmedov, and C. Bambi, "Can the dynamics of test particles around charged stringy black holes mimic the spin of Kerr black holes?" *Phys. Rev. D*, vol. 102, no. 4, p. 044013, Aug. 2020.

[123] ——, "Dynamics of test particles around a Bardeen black hole surrounded by perfect fluid dark matter," *Phys. Rev. D*, vol. 102, no. 10, p. 104062, Nov. 2020.

[124] J. Kovář, P. Slaný, C. Cremaschini, Z. Stuchlík, V. Karas, and A. Trova, "Electrically charged matter in rigid rotation around magnetized black hole," *Phys. Rev. D*, vol. 90, no. 4, p. 044029, Aug. 2014.

[125] S. Shaymatov, M. Patil, B. Ahmedov, and P. S. Joshi, "Destroying a near-extremal Kerr black hole with a charged particle: Can a test magnetic field

serve as a cosmic censor?" *Phys. Rev. D*, vol. 91, no. 6, p. 064025, Mar. 2015.

[126] K. Düztaş, M. Jamil, S. Shaymatov, and B. Ahmedov, "Testing Cosmic Censorship Conjecture for Extremal and Near-extremal (2+1)-dimensional MTZ Black Holes," *Class. Quantum Grav.*, vol. 37, no. 17, p. 175005, aug 2020.

[127] S. Shaymatov, J. Vrba, D. Malafarina, B. Ahmedov, and Z. Stuchlík, "Charged particle and epicyclic motions around 4 D Einstein-Gauss-Bonnet black hole immersed in an external magnetic field," *Phys. Dark Universe*, vol. 30, p. 100648, Dec. 2020.

[128] S. Shaymatov and B. Ahmedov, "Overcharging process around a magnetized black hole: can the backreaction effect of magnetic field restore cosmic censorship conjecture?" *Gen. Relativ. Gravit.*, vol. 55, no. 2, p. 36, Feb. 2023.

[129] S. Shaymatov, B. Narzilloev, A. Abdujabbarov, and C. Bambi, "Charged particle motion around a magnetized Reissner-Nordström black hole," *Phys. Rev. D*, vol. 103, no. 12, p. 124066, Jun. 2021.

[130] S. Shaymatov, M. Alloqulov, B. Ahmedov, and A. Wang, "Kerr-Newman-modified-gravity black hole's impact on the magnetic reconnection," *Phys. Rev. D*, vol. 110, no. 4, p. 044005, Aug. 2024.

[131] S. U. Khan, U. Uktamov, J. Rayimbaev, A. Abdujabbarov, I. Ibragimov, and Z.-M. Chen, "Circular orbits and collisions of particles with magnetic dipole moment near magnetized Kerr black holes in modified gravity," *Eur. Phys. J. C*, vol. 84, no. 2, p. 203, 2024.

[132] S. Shaymatov, "Efficiency of magnetic Penrose process in higher dimensional Myers-Perry black hole spacetimes," *Phys. Rev. D*, vol. 110, no. 4, p. 044042, Aug. 2024.

[133] O. L. M. Ginzburg V. L., *Zh. Eksp. Teor. Fiz.*, vol. 47, p. 1030, 1964.

[134] J. L. Anderson and J. M. Cohen, "Gravitational Collapse of Magnetic Neutron Stars," *Astrophys. Space Sci.*, vol. 9, pp. 146–152, Oct. 1970.

[135] R. M. Wald, "Black hole in a uniform magnetic field," *Phys. Rev. D*, vol. 10, pp. 1680–1685, Sep. 1974.

[136] L. Rezzolla, B. J. Ahmedov, and J. C. Miller, "General relativistic electromagnetic fields of a slowly rotating magnetized neutron star - I. Formulation of the equations," *Mon. Not. R. Astron. Soc.*, vol. 322, no. 4, pp. 723–740, Apr. 2001.

[137] V. S. Morozova, B. J. Ahmedov, and O. Zanotti, "Explaining radio emission of magnetars via rotating and oscillating magnetospheres of neutron stars," *Mon. Not. R. Astron. Soc.*, vol. 419, pp. 2147–2155, Jan. 2012.

[138] J. Kovář, P. Slaný, C. Cremaschini, Z. Stuchlík, V. Karas, and A. Trova, "Electrically charged matter in rigid rotation around magnetized black hole," *Phys. Rev. D*, vol. 90, no. 4, p. 044029, Aug. 2014.

[139] M. Y. Piotrovich, N. A. Silant'ev, Y. N. Gnedin, and T. M. Natsvlishvili, "Magnetic Fields of Black Holes and the Variability Plane," *ArXiv e-prints*, Feb. 2010.

[140] A.-K. Baczko, R. Schulz, and et al., "A highly magnetized twin-jet base pinpoints a supermassive black hole," *Astron. Astrophys.*, vol. 593, p. A47, Sep. 2016.

[141] R. A. Daly, "Black Hole Spin and Accretion Disk Magnetic Field Strength Estimates for More Than 750 Active Galactic Nuclei and Multiple Galactic Black Holes," *Astrophys. J.*, vol. 886, no. 1, p. 37, Nov. 2019.

[142] Y. Dallilar and et al., "A precise measurement of the magnetic field in the corona of the black hole binary v404 cygni," *Science*, vol. 358, no. 6368, pp. 1299–1302, 2017. [Online]. Available: http://science.sciencemag.org/content/358/6368/1299

[143] Event Horizon Telescope Collaboration, "First M87 Event Horizon Telescope Results. VIII. Magnetic Field Structure near The Event Horizon," *Astrophys. J. Lett.*, vol. 910, no. 1, p. L13, Mar. 2021.

[144] R. Narayan, D. C. M. Palumbo, M. D. Johnson, and et al., "The Polarized Image of a Synchrotron-emitting Ring of Gas Orbiting a Black Hole," *Astrophys. J.*, vol. 912, no. 1, p. 35, May 2021.

[145] J. A. Petterson, "Magnetic field of a current loop around a schwarzschild black hole," *Phys. Rev. D*, vol. 10, pp. 3166–3170, Nov 1974. [Online]. Available: https://link.aps.org/doi/10.1103/PhysRevD.10.3166

[146] V. P. Frolov and A. A. Shoom, "Motion of charged particles near a weakly magnetized Schwarzschild black hole," *Phys. Rev. D*, vol. 82, no. 8, p. 084034, Oct. 2010.

[147] Z. Stuchlík and M. Kološ, "Acceleration of the charged particles due to chaotic scattering in the combined black hole gravitational field and asymptotically uniform magnetic field," *Eur. Phys. J. C*, vol. 76, p. 32, Jan. 2016.

[148] M. Azreg-Aïnou, "Vacuum and nonvacuum black holes in a uniform magnetic field," *European Physical Journal C*, vol. 76, no. 7, p. 414, Jul. 2016.

[149] U. Uktamov, M. Fathi, J. Rayimbaev, and A. Abdujabbarov, "Orbits of particles with magnetic dipole moment around magnetized schwarzschild black holes: Applications to the s2 star orbit," *Phys. Rev. D*, vol. 110, p. 084084, Oct 2024. [Online]. Available: https://link.aps.org/doi/10.1103/PhysRevD.110.084084

[150] G. Preti, "General relativistic dynamics of polarized particles in electromagnetic fields," *Phys. Rev. D*, vol. 70, no. 2, p. 024012, Jul. 2004.

[151] S. Shaymatov, K. Jusufi, M. Alloqulov, and B. Ahmedov, "Epicyclic motions and constraints on the charged stringy black hole spacetime," *Eur. Phys. J. Plus*, vol. 138, no. 11, p. 997, Nov 2023. [Online]. Available: https://doi.org/10.1140/epjp/s13360-023-04604-y

[152] S. Shaymatov, M. Jamil, K. Jusufi, and K. Bamba, "Constraints on the magnetized Ernst black hole spacetime through quasiperiodic oscillations," *Eur. Phys. J. C*, vol. 82, no. 7, p. 636, Jul. 2022.

[153] K. Schwarzschild, "Über das Gravitationsfeld eines Massenpunktes nach der Einsteinschen Theorie," *Sitzungsberichte der Königlich Preussischen Akademie der Wissenschaften*, pp. 189–196, Jan. 1916.

[154] F. W. Dyson, A. S. Eddington, and C. Davidson, "A Determination of the Deflection of Light by the Sun's Gravitational Field, from Observations Made at the Total Eclipse of May 29, 1919," *Philosophical Transactions of the Royal Society of London Series A*, vol. 220, pp. 291–333, Jan. 1920.

[155] G. M. Clemence, "The relativity effect in planetary motions," *Rev. Mod. Phys.*, vol. 19, pp. 361–364, Oct 1947. [Online]. Available: https://link.aps.org/doi/10.1103/RevModPhys.19.361

[156] Y. Hagihara, "Theory of the Relativistic Trajeetories in a Gravitational Field of Schwarzschild," *Japanese Journal of Astronomy and Geophysics*, vol. 8, p. 67, Jan. 1930.

[157] C. G. Darwin, "The gravity field of a particle," *Proceedings of the Royal Society of London. Series A. Mathematical and Physical Sciences*, vol. 249, no. 1257, pp. 180–194, Jan. 1959. [Online]. Available: https://royalsocietypublishing.org/doi/10.1098/rspa.1959.0015

[158] ——, "The gravity field of a particle. II," *Proceedings of the Royal Society of London. Series A. Mathematical and Physical Sciences*, vol. 263, no. 1312, pp. 39–50, Aug. 1961. [Online]. Available: https://royalsocietypublishing.org/doi/10.1098/rspa.1961.0142

[159] B. Mielnik and J. Plebański, "A study of geodesic motion in the field of schwarzschild's solution," *Acta Phys. Pol.*, vol. 21, pp. 239–268, 1962.

[160] C. G. J. Jacobi, *C. G. J. Jacobi's Gesammelte Werke: Herausgegeben auf Veranlassung der königlich preussischen Akademie der Wissenschaften*, ser. Cambridge Library Collection - Mathematics, K. Weierstrass, Ed. Cambridge University Press, 2013.

[161] N. H. Abel, *Oeuvres complètes de Niels Henrik Abel: Nouvelle édition*, ser. Cambridge Library Collection - Mathematics, L. Sylow and S. Lie, Eds. Cambridge University Press, vol. 2.

[162] B. Riemann, "Theorie der Abel'schen Functionen." *Journal für die reine und angewandte Mathematik (Crelles Journal)*, vol. 1857, no. 54, pp. 115–155, Jul. 1857. [Online]. Available: https://www.degruyter.com/document/doi/10.1515/crll.1857.54.115/html

[163] ——, "Ueber das verschwinden der $\vartheta$-functionen." *Journal für die reine und angewandte Mathematik (Crelles Journal)*, vol. 1866, no. 65, pp. 161–172, 1866. [Online]. Available: https://doi.org/10.1515/crll.1866.65.161

[164] C. Weierstrass, "Zur theorie der abelschen functionen." *Journal für die reine und angewandte Mathematik (Crelles Journal)*, vol. 1854, no. 47, pp. 289–306, 1854. [Online]. Available: https://doi.org/10.1515/crll.1854.47.289

[165] H. F. Baker, *Abelian functions: Abel's theorem and the allied theory of theta functions*, ser. Cambridge mathematical library. Cambridge, [Eng.] ; New York: Cambridge University Press, 1995.

[166] G. V. Kraniotis and S. B. Whitehouse, "General relativity, the cosmological constant and modular forms," *Classical and Quantum Gravity*, vol. 19, no. 20, pp. 5073–5100, Oct. 2002. [Online]. Available: https://iopscience.iop.org/article/10.1088/0264-9381/19/20/304

[167] ——, "Compact calculation of the perihelion precession of Mercury in general relativity, the cosmological constant and Jacobi's inversion problem," *Classical and Quantum Gravity*, vol. 20, no. 22, pp. 4817–4835, Nov. 2003. [Online]. Available: https://iopscience.iop.org/article/10.1088/0264-9381/20/22/007

[168] G. V. Kraniotis, "Precise relativistic orbits in Kerr and Kerr–(anti) de Sitter spacetimes," *Classical and Quantum Gravity*, vol. 21, no. 19, pp. 4743–4769, Oct. 2004. [Online]. Available: https://iopscience.iop.org/article/10.1088/0264-9381/21/19/016

[169] ——, "Frame dragging and bending of light in Kerr and Kerr–(anti) de Sitter spacetimes," *Classical and Quantum Gravity*, vol. 22, no. 21,

pp. 4391–4424, Nov. 2005. [Online]. Available: https://iopscience.iop.org/article/10.1088/0264-9381/22/21/001

[170] N. Cruz, M. Olivares, and J. R. Villanueva, "The geodesic structure of the Schwarzschild anti-de Sitter black hole," *Classical and Quantum Gravity*, vol. 22, no. 6, pp. 1167–1190, Mar. 2005. [Online]. Available: https://iopscience.iop.org/article/10.1088/0264-9381/22/6/016

[171] G. V. Kraniotis, "Periapsis and gravitomagnetic precessions of stellar orbits in Kerr and Kerr–de Sitter black hole spacetimes," *Classical and Quantum Gravity*, vol. 24, no. 7, pp. 1775–1808, Apr. 2007. [Online]. Available: https://iopscience.iop.org/article/10.1088/0264-9381/24/7/007

[172] E. Hackmann and C. Lämmerzahl, "Complete Analytic Solution of the Geodesic Equation in Schwarzschild–(Anti-)de Sitter Spacetimes," *Physical Review Letters*, vol. 100, no. 17, p. 171101, May 2008. [Online]. Available: https://link.aps.org/doi/10.1103/PhysRevLett.100.171101

[173] ——, "Geodesic equation in Schwarzschild-(anti-)de Sitter space-times: Analytical solutions and applications," *Physical Review D*, vol. 78, no. 2, p. 024035, Jul. 2008. [Online]. Available: https://link.aps.org/doi/10.1103/PhysRevD.78.024035

[174] E. Hackmann, V. Kagramanova, J. Kunz, and C. Lämmerzahl, "Analytic solutions of the geodesic equation in axially symmetric space-times," *EPL (Europhysics Letters)*, vol. 88, no. 3, p. 30008, Nov. 2009. [Online]. Available: https://iopscience.iop.org/article/10.1209/0295-5075/88/30008

[175] E. Hackmann, B. Hartmann, C. Lämmerzahl, and P. Sirimachan, "Complete set of solutions of the geodesic equation in the space-time of a Schwarzschild black hole pierced by a cosmic string," *Physical*

*Review D*, vol. 81, no. 6, p. 064016, Mar. 2010. [Online]. Available: https://link.aps.org/doi/10.1103/PhysRevD.81.064016

[176] M. Olivares, J. Saavedra, C. Leiva, and J. R. Villanueva, "MOTION OF CHARGED PARTICLES ON THE REISSNER–NORDSTRÖM (ANTI)-DE SITTER BLACK HOLE SPACETIME," *Modern Physics Letters A*, vol. 26, no. 39, pp. 2923–2950, Dec. 2011. [Online]. Available: https://www.worldscientific.com/doi/abs/10.1142/S0217732311037261

[177] G. V. Kraniotis, "Precise analytic treatment of Kerr and Kerr-(anti) de Sitter black holes as gravitational lenses," *Classical and Quantum Gravity*, vol. 28, no. 8, p. 085021, Apr. 2011. [Online]. Available: https://iopscience.iop.org/article/10.1088/0264-9381/28/8/085021

[178] N. Cruz, M. Olivares, and J. R. Villanueva, "Geodesic structure of Lifshitz black holes in 2+1 dimensions," *The European Physical Journal C*, vol. 73, no. 7, p. 2485, Jul. 2013. [Online]. Available: http://link.springer.com/10.1140/epjc/s10052-013-2485-8

[179] J. R. Villanueva, J. Saavedra, M. Olivares, and N. Cruz, "Photons motion in charged Anti-de Sitter black holes," *Astrophysics and Space Science*, vol. 344, no. 2, pp. 437–446, Apr. 2013. [Online]. Available: http://link.springer.com/10.1007/s10509-012-1333-x

[180] G. V. Kraniotis, "Gravitational lensing and frame dragging of light in the Kerr–Newman and the Kerr–Newman (anti) de Sitter black hole spacetimes," *General Relativity and Gravitation*, vol. 46, no. 11, p. 1818, Nov. 2014. [Online]. Available: http://link.springer.com/10.1007/s10714-014-1818-8

[181] S. Soroushfar, R. Saffari, J. Kunz, and C. Lämmerzahl, "Analytical solutions of the geodesic equation in the spacetime of a black hole in f ( R ) gravity," *Physical Review D*, vol. 92, no. 4, p. 044010, Aug. 2015. [Online]. Available: https://link.aps.org/doi/10.1103/PhysRevD.92.044010

[182] J. R. Villanueva and M. Olivares, "Gravitational Rutherford scattering and Keplerian orbits for electrically charged bodies in heterotic string theory," *The European Physical Journal C*, vol. 75, no. 11, p. 562, Nov. 2015. [Online]. Available: http://link.springer.com/10.1140/epjc/s10052-015-3794-x

[183] S. Soroushfar, R. Saffari, S. Kazempour, S. Grunau, and J. Kunz, "Detailed study of geodesics in the Kerr-Newman-(A)dS spacetime and the rotating charged black hole spacetime in f ( R ) gravity," *Physical Review D*, vol. 94, no. 2, p. 024052, Jul. 2016. [Online]. Available: https://link.aps.org/doi/10.1103/PhysRevD.94.024052

[184] B. Hoseini, R. Saffari, S. Soroushfar, S. Grunau, and J. Kunz, "Analytic treatment of complete geodesics in a static cylindrically symmetric conformal spacetime," *Physical Review D*, vol. 94, no. 4, p. 044021, Aug. 2016. [Online]. Available: https://link.aps.org/doi/10.1103/PhysRevD.94.044021

[185] B. Hoseini, R. Saffari, and S. Soroushfar, "Study of the geodesic equations of a spherical symmetric spacetime in conformal Weyl gravity," *Classical and Quantum Gravity*, vol. 34, no. 5, p. 055004, Mar. 2017. [Online]. Available: https://iopscience.iop.org/article/10.1088/1361-6382/aa5a63

[186] M. Fathi, M. Kariminezhaddahka, M. Olivares, and J. R. Villanueva, "Motion of massive particles around a charged Weyl black hole and the geodetic precession of orbiting gyroscopes," *The European Physical*

*Journal C*, vol. 80, no. 5, p. 377, May 2020. [Online]. Available: https://link.springer.com/10.1140/epjc/s10052-020-7945-3

[187] M. Fathi, M. Olivares, and J. R. Villanueva, "Classical tests on a charged Weyl black hole: bending of light, Shapiro delay and Sagnac effect," *The European Physical Journal C*, vol. 80, no. 1, p. 51, Jan. 2020. [Online]. Available: http://link.springer.com/10.1140/epjc/s10052-020-7623-5

[188] ——, "Gravitational Rutherford scattering of electrically charged particles from a charged Weyl black hole," *The European Physical Journal Plus*, vol. 136, no. 4, p. 420, Apr. 2021. [Online]. Available: https://link.springer.com/10.1140/epjp/s13360-021-01441-9

[189] P. A. González, M. Olivares, Y. Vásquez, and J. R. Villanueva, "Null geodesics in five-dimensional Reissner–Nordström anti-de Sitter black holes," *The European Physical Journal C*, vol. 81, no. 3, p. 236, Mar. 2021. [Online]. Available: https://link.springer.com/10.1140/epjc/s10052-021-09024-9

[190] M. Fathi, M. Olivares, and J. R. Villanueva, "Analytical study of light ray trajectories in Kerr spacetime in the presence of an inhomogeneous anisotropic plasma," *The European Physical Journal C*, vol. 81, no. 11, p. 987, Nov. 2021. [Online]. Available: https://link.springer.com/10.1140/epjc/s10052-021-09787-1

[191] G. V. Kraniotis, "Gravitational redshift/blueshift of light emitted by geodesic test particles, frame-dragging and pericentre-shift effects, in the Kerr–Newman–de Sitter and Kerr–Newman black hole geometries," *The European Physical Journal C*, vol. 81, no. 2, p. 147, Feb. 2021. [Online]. Available: https://link.springer.com/10.1140/epjc/s10052-021-08911-5

[192] M. Fathi, M. Olivares, and J. R. Villanueva, "Study of null and time-like geodesics in the exterior of a Schwarzschild black hole with quintessence and cloud of strings," *The European Physical Journal C*, vol. 82, no. 7, p. 629, Jul. 2022. [Online]. Available: https://link.springer.com/10.1140/epjc/s10052-022-10600-w

[193] S. Soroushfar and M. Afrooz, "Analytical solutions of the geodesic equation in the space-time of a black hole surrounded by perfect fluid in Rastall theory," *Indian Journal of Physics*, vol. 96, no. 2, pp. 593–607, Feb. 2022. [Online]. Available: https://link.springer.com/10.1007/s12648-020-01971-5

[194] E. Battista and G. Esposito, "Geodesic motion in Euclidean Schwarzschild geometry," *The European Physical Journal C*, vol. 82, no. 12, p. 1088, Dec. 2022. [Online]. Available: https://link.springer.com/10.1140/epjc/s10052-022-11070-w

[195] M. Fathi, M. Olivares, and J. R. Villanueva, "Spherical photon orbits around a rotating black hole with quintessence and cloud of strings," *The European Physical Journal Plus*, vol. 138, no. 1, p. 7, Jan. 2023. [Online]. Available: https://link.springer.com/10.1140/epjp/s13360-022-03538-1

[196] M. Fathi, "Analytical study of particle geodesics around a scale-dependent de sitter black hole," *Annals of Physics*, vol. 457, p. 169401, 2023. [Online]. Available: https://www.sciencedirect.com/science/article/pii/S0003491623001872

[197] L. Perek, "Galactic orbits of stars," *Vistas in Astronomy*, vol. 5, pp. 28–39, Jan. 1962. [Online]. Available: https://linkinghub.elsevier.com/retrieve/pii/008366566290003X

[198] M. Barbieri and R. G. Gratton, "Galactic orbits of stars with planets," *Astronomy & Astrophysics*, vol. 384, no. 3, pp. 879–883, Mar. 2002. [Online]. Available: http://www.aanda.org/10.1051/0004-6361:20020011

[199] S. Zhong, K. Hayasaki, S. Li, P. Berczik, and R. Spurzem, "Exploring the Origin of Stars on Bound and Unbound Orbits Causing Tidal Disruption Events," *The Astrophysical Journal*, vol. 959, no. 1, p. 19, Dec. 2023. [Online]. Available: https://iopscience.iop.org/article/10.3847/1538-4357/ad0122

[200] J. Binney and S. Tremaine, *Galactic Dynamics: Second Edition*. Princeton University Press, Oct. 2011. [Online]. Available: http://www.jstor.org/stable/10.2307/j.ctvc778ff

[201] P. S. Behroozi, A. Loeb, and R. H. Wechsler, "Unbound particles in dark matter halos," *Journal of Cosmology and Astroparticle Physics*, vol. 2013, no. 06, pp. 019–019, Jun. 2013. [Online]. Available: https://iopscience.iop.org/article/10.1088/1475-7516/2013/06/019

[202] A. N. Aliev and D. V. Gal'tsov, ""Magnetized" black holes," *Soviet Physics Uspekhi*, vol. 32, no. 1, pp. 75–92, Jan. 1989. [Online]. Available: https://iopscience.iop.org/article/10.1070/PU1989v032n01ABEH002677

[203] L.-X. Li, "Observational signatures of the magnetic connection between a black hole and a disk," *Astronomy & Astrophysics*, vol. 392, no. 2, pp. 469–472, Sep. 2002. [Online]. Available: http://www.aanda.org/10.1051/0004-6361:20020958

[204] D. L. Meier, *Black Hole Astrophysics: The Engine Paradigm*. Berlin, Heidelberg: Springer Berlin Heidelberg, 2012. [Online]. Available: https://link.springer.com/10.1007/978-3-642-01936-4

[205] S. I. Kruglov, "Magnetized black holes and nonlinear electrodynamics," *International Journal of Modern Physics A*, vol. 32, no. 23n24, p. 1750147, Aug. 2017. [Online]. Available: https://www.worldscientific.com/doi/abs/10.1142/S0217751X17501470

[206] D. Ghosh, A. Thalapillil, and F. Ullah, "Astrophysical hints for magnetic black holes," *Physical Review D*, vol. 103, no. 2, p. 023006, Jan. 2021. [Online]. Available: https://link.aps.org/doi/10.1103/PhysRevD.103.023006

[207] O. Kopáček and V. Karas, "Magnetized black holes: The role of rotation, boost, and accretion in twisting the field lines and accelerating particles," in *The Sixteenth Marcel Grossmann Meeting*. Online: WORLD SCIENTIFIC, Feb. 2023, pp. 3999–4009. [Online]. Available: https://www.worldscientific.com/doi/10.1142/9789811269776_0333

[208] V. Karas and Z. Stuchlík, "Magnetized Black Holes: Interplay between Charge and Rotation," *Universe*, vol. 9, no. 6, p. 267, Jun. 2023. [Online]. Available: https://www.mdpi.com/2218-1997/9/6/267

[209] S. Chang, L. Zhang, Z. Jiang, and X. Li, "Trajectories and radiation of charged particles in the pulsar magnetosphere," *Monthly Notices of the Royal Astronomical Society*, vol. 513, no. 1, pp. 925–933, 04 2022. [Online]. Available: https://doi.org/10.1093/mnras/stac931

[210] P. Mészáros, "Gamma-ray bursts: theoretical issues and developments," in *INTEGRAL CONFERENCE AND AHEAD GAMMA-RAY WORKSHOP INTEGRAL LOOKS AHEAD TO MULTI-MESSENGER ASTRONOMY*. Mem. Soc. Ast. It. 90, 1-2, 2019, pp. 57–66. [Online]. Available: https://www.memsait.it/volumi/Vol.%2090%20n.%201-2,%202019/2019MmSAI..90...57M.pdf

[211] I. D. Novikov and B. E. Stern, *The Possible Mechanism of the Formation of the Hard Spectrum of Active Galactic Nuclei.* Dordrecht: Springer Netherlands, 1986, pp. 149–171. [Online]. Available: https://doi.org/10.1007/978-94-009-4562-3_10

[212] K. Nishikawa, G. Richardson, S. Koide, K. Shibata, T. Kudoh, P. Hardee, and G. J. Fishman, "A General Relativistic Magnetohydrodynamic Simulation of Jet Formation," *The Astrophysical Journal*, vol. 625, no. 1, pp. 60–71, May 2005. [Online]. Available: https://iopscience.iop.org/article/10.1086/429360

[213] M. Mościbrodzka, H. Falcke, and H. Shiokawa, "General relativistic magnetohydrodynamical simulations of the jet in M 87," *Astronomy & Astrophysics*, vol. 586, p. A38, Feb. 2016. [Online]. Available: http://www.aanda.org/10.1051/0004-6361/201526630

[214] Y. Mizuno, "GRMHD Simulations and Modeling for Jet Formation and Acceleration Region in AGNs," *Universe*, vol. 8, no. 2, p. 85, Jan. 2022. [Online]. Available: https://www.mdpi.com/2218-1997/8/2/85

[215] R. M. Wald, *General relativity.* Chicago: University of Chicago Press, 1984.

[216] L. Rezzolla, B. J. Ahmedov, and J. C. Miller, "General relativistic electromagnetic fields of a slowly rotating magnetized neutron star - I. Formulation of the equations," *Mon. Not. R. Astron. Soc*, vol. 322, pp. 723–740, Apr. 2001.

[217] G. Preti, "General relativistic dynamics of polarized particles in electromagnetic fields," , vol. 70, no. 2, p. 024012, Jul. 2004.

[218] F. de Felice and F. Sorge, "Magnetized orbits around a Schwarzschild black hole," *Classical and Quantum Gravity*, vol. 20, no. 3, pp. 469–481, Feb. 2003.

[219] Y.-K. Lim and Z. C. Yeo, "Energies and angular momenta of periodic Schwarzschild geodesics," , vol. 109, no. 2, p. 024037, Jan. 2024.

[220] J. Levin and G. Perez-Giz, "A periodic table for black hole orbits," , vol. 77, no. 10, p. 103005, May 2008.

[221] S. Chandrasekhar, *The Mathematical Theory of Black Holes*, 1998.

[222] P. F. Byrd and M. D. Friedman, *Handbook of Elliptic Integrals for Engineers and Scientists*. Berlin, Heidelberg: Springer Berlin Heidelberg, 1971. [Online]. Available: http://link.springer.com/10.1007/978-3-642-65138-0

[223] T. Lacroix, "Dynamical constraints on a dark matter spike at the Galactic centre from stellar orbits," *A& A*, vol. 619, p. A46, Nov. 2018.

[224] T. Do, A. Hees, A. Ghez, G. D. Martinez, D. S. Chu, S. Jia, S. Sakai, J. R. Lu, A. K. Gautam, K. K. O'Neil, E. E. Becklin, M. R. Morris, K. Matthews, S. Nishiyama, R. Campbell, S. Chappell, Z. Chen, A. Ciurlo, A. Dehghanfar, E. Gallego-Cano, W. E. Kerzendorf, J. E. Lyke, S. Naoz, H. Saida, R. Schödel, M. Takahashi, Y. Takamori, G. Witzel, and P. Wizinowich, "Relativistic redshift of the star S0-2 orbiting the Galactic Center supermassive black hole," *Science*, vol. 365, no. 6454, pp. 664–668, Aug. 2019.

[225] M. Habibi, S. Gillessen, F. Martins, F. Eisenhauer, P. M. Plewa, O. Pfuhl, E. George, J. Dexter, I. Waisberg, T. Ott, S. von Fellenberg, M. Bauböck, A. Jimenez-Rosales, and R. Genzel, "Twelve Years of Spectroscopic Monitoring in the Galactic Center: The Closest Look at S-stars near the Black Hole," , vol. 847, no. 2, p. 120, Oct. 2017.

[226] D. Kunneriath, G. Witzel, A. Eckart, M. Zamaninasab, R. Gießübel, R. Schödel, F. K. Baganoff, M. R. Morris, M. Dovčiak, W. J. Duschl, M. García-Marín, V. Karas, S. König, T. P. Krichbaum, M. Krips, R. S. Lu, J. Mauerhan, J. Moultaka, K. Mužić, N. Sabha, F. Najarro, J. U. Pott, K. F. Schuster, L. O. Sjouwerman, C. Straubmeier, C. Thum, S. N. Vogel, P. Teuben, A. Weiss, H. Wiesemeyer, and J. A. Zensus, "Coordinated NIR/mm observations of flare emission from Sagittarius A*," *Atsron. Astrophys*, vol. 517, p. A46, Jul. 2010.

[227] A. Eckart, M. García-Marín, S. N. Vogel, P. Teuben, M. R. Morris, F. Baganoff, J. Dexter, R. Schödel, G. Witzel, M. Valencia-S., V. Karas, D. Kunneriath, C. Straubmeier, L. Moser, N. Sabha, R. Buchholz, M. Zamaninasab, K. Mužić, J. Moultaka, and J. A. Zensus, "Millimeter to X-ray flares from Sagittarius A*," *Astron.Astrphys*, vol. 537, p. A52, Jan. 2012.

[228] R. P. Eatough, H. Falcke, R. Karuppusamy, K. J. Lee, D. J. Champion, E. F. Keane, G. Desvignes, D. H. F. M. Schnitzeler, L. G. Spitler, M. Kramer, B. Klein, C. Bassa, G. C. Bower, A. Brunthaler, I. Cognard, A. T. Deller, P. B. Demorest, P. C. C. Freire, A. Kraus, A. G. Lyne, A. Noutsos, B. Stappers, and N. Wex, "A strong magnetic field around the supermassive black hole at the centre of the Galaxy," *Nature*, vol. 501, no. 7467, pp. 391–394, Sep. 2013.

[229] Y. B. Zel'dovich, I. D. Novikov, and J. Silk, "Relativistic Astrophysics, Vol. 1: Stars and Relativity," *Physics Today*, vol. 25, no. 3, p. 63, Jan. 1972.

[230] L. Ryder, *Introduction to General Relativity*. Cambridge University Press, 2009.

[231] Y. B. Zel'dovich and I. D. Novikov, *Stars and relativity*. Mineola, N.Y: Dover Publications, 2014.